

**RETRIEVAL OF LAND
SURFACE PARAMETERS USING
PASSIVE MICROWAVE
REMOTE SENSING**

Richard A.M. de Jeu

Cover: Earth rising above the Moon's horizon. Photo was taken during the famous Apollo-11 mission where astronaut Neal Armstrong stepped onto the lunar surface for the first time.
Photo Credit: NASA

© Richard A.M. de Jeu, 2003

This study was partly funded by the NASA Seasonal-to-Interannual Prediction Project (NSIPP) and was carried out at the Hydrological Sciences Branch (MC 974) at NASA Goddard Space Flight Center, Greenbelt, MD, USA, and the Department of Geo-Environmental Sciences, Faculty of Earth and Life Sciences, Vrije Universiteit Amsterdam, the Netherlands.

The full text of this thesis and additional background information are available on the internet at <http://www.geo.vu.nl/~geomil>

Retrieval of land surface parameters using passive microwave remote sensing.
Richard de Jeu, Ph.D. Thesis Vrije Universiteit Amsterdam.

ISBN 09-9016430-8

NUR-code: 934

Subject headings:

Passive Microwave Remote Sensing / SMMR / Soil Moisture / Soil Temperature / Vegetation Indices

This thesis was printed by: PrintPartners Ipskamp, Enschede, the Netherlands

VRIJE UNIVERSITEIT

**Retrieval of Land Surface Parameters using Passive
Microwave Remote Sensing**

ACADEMISCH PROEFSCHRIFT

ter verkrijging van de graad van doctor aan
de Vrije Universiteit Amsterdam,
op gezag van de rector magnificus
prof.dr. T. Sminia,
in het openbaar te verdedigen
ten overstaan van de promotiecommissie
van de faculteit der Aard- en Levenswetenschappen
op dinsdag 4 februari 2003 om 15.45 uur
in het auditorium van de universiteit,
De Boelelaan 1105

door

Richard Adrianus Maria de Jeu

geboren te Alkemade

promotor: prof.dr. H.F. Vugts
copromotor: dr. M. Owe

Contents

1	General Introduction	1
1.1	Background	1
1.2	Thesis Objective and Approach	2
1.3	Thesis Outline	2
2	Microwave Theory	3
2.1	Introduction	3
2.2	Dielectric Constant	4
2.3	Soil Physical Properties	5
2.4	Thermal Sampling Depth	6
2.5	Surface Roughness	7
2.6	Vegetation Effects	8
2.7	Dependence of Polarization on Vegetation	12
2.8	Atmosphere	13
3	Description of Data Sets	15
3.1	Satellite Data	15
3.1.1	Nimbus-SMMR	15
3.1.2	TRMM	16
3.1.3	NOAA-AVHRR	17
3.2	Land Surface Data	17
3.2.1	Vegetation	17
3.2.2	Soil Properties	18
3.2.3	Soil Temperature	19
3.2.4	Soil Moisture	20
3.3	Atmospheric Data	22
3.3.1	Precipitation	22
3.3.2	Clouds	22
4	Derivation of Surface Soil Temperatures	25
4.1	Introduction	25
4.2	Atmospheric Effects	26
4.3	Surface Soil Temperature Model	30

4.4	Validation of the Model	33
4.5	Results	34
4.6	Conclusions and Discussion	36
5	Retrieval of Soil Moisture and Vegetation Optical Depth	37
5.1	Introduction	37
5.2	Modelling Approach	38
5.3	Results	42
5.4	Summary and Conclusions	44
6	Limitations of the Land Surface Parameter Retrievals	49
6.1	Introduction	49
6.2	Error Propagation Analysis	50
6.2.1	Theory	50
6.2.2	Application to the Test Sites	51
6.3	Masking Routine	56
6.3.1	General	56
6.3.2	Snow and Frozen Soil	56
6.3.3	Vegetation	56
6.4	Conclusions	58
7	Land Surface Parameters derived from 18 GHz	59
7.1	Introduction	59
7.2	Model Modification	60
7.3	Results	61
7.3.1	Vegetation	61
7.3.2	Soil Moisture	61
7.3.3	Interrelationships and Errors	61
7.4	Conclusions and Recommendations	62
8	Applications	67
8.1	Introduction	67
8.2	Global Vegetation Monitoring	67
8.2.1	Introduction	67
8.2.2	Global Vegetation Mapping	68
8.2.3	Conclusions	74
8.3	Soil Moisture Dynamics	75
8.3.1	Introduction	75
8.3.2	The Indian Monsoon	75
8.3.3	Annual Soil Moisture Changes versus Monsoon Circulation	78
8.3.4	Conclusions	78
8.4	Time Series Analysis on the Surface Soil Temperatures	79
8.4.1	Introduction	79
8.4.2	Time Series Analysis	79
8.4.3	Application to the Continental United States	82

9 Summary and Conclusions	87
9.1 General	87
9.2 Soil Temperature	88
9.3 Soil Moisture and Vegetation Optical Depth	88
9.4 Model Sensitivity	89
9.5 Wavelength Effects	90
9.6 Applications	90
9.7 Follow-up Studies	91
10 Samenvatting en Conclusies	93
10.1 Algemeen	93
10.2 Bodemtemperatuur	94
10.3 Bodemvocht en Vegetatie	94
10.4 Gevoeligheid van het Model	95
10.5 Golflengte Effecten	96
10.6 Toepassingen	96
10.7 Vervolgstudies	97
Bibliography	99
Appendix A: Wang-Schmugge Model	109
Appendix B: Acronyms and Symbols	111
Acknowledgements	115
Publications and Reports	117

List of Figures

2.1	Comparison of horizontal and vertical polarized emissivity calculated for an average soil at the SMMR wavelength and incidence angle with no canopy cover.	4
2.2	Comparison of the soil dielectric constants for typical sand, loam, and clay soils. The real part is designated by ϵ' and the imaginary part by ϵ''	6
2.3	Horizontal polarized brightness temperature calculated for a range of roughness values using Equation 2.4.	7
2.4	Schematic representation of the partitioning of microwave radiation from a vegetation covered surface in terms of the brightness temperature (From Van de Griend and Owe (1993)).	9
2.5	The effect of the vegetation optical depth on the emissivity. At H-polarization, the sensitivity of the above canopy emissivity is severely reduced at an optical depth of about 0.75 ($\Gamma = 0.3$).	10
2.6	The effect of the single scattering albedo on the soil moisture brightness temperature relationship.	11
2.7	Locations of SMMR footprints used to calculate the vertical and horizontal optical depth at saturated conditions.	12
2.8	Relationship between vertical and horizontal optical depth.	13
3.1	Location maps of the field stations. Figure (A) is a global overview, (B) shows the U.S. sites, (C) the African site and (D) the Eurasian sites.	23
4.1	Time series of the brightness temperature ratio (-o-) at different wavelengths and the precipitable water (-) for the Mongolia test site	27
4.2	Time series of the brightness temperature ratio (-o-) at different wavelengths and the precipitable water (-) for the Libya test site	28
4.3	Time series of the vertical (top) and horizontal (bottom) emissivity at 37 GHz (-o-) and the precipitable water (-) for the Mongolia test site	29
4.4	Time series of the vertical (top) and horizontal (bottom) emissivity at 37 GHz (-o-) and the precipitable water (-) for the Libya test site	30
4.5	Relation between the vertical polarized brightness temperature at 37 GHz and the soil temperature at 5 cm depth for different soil moisture conditions. Note that the influence of soil moisture on the linear relationship does have a random character.	31

4.6	The relationship between soil temperature at 5 cm depth and 1.25 cm depth according to field observations in Botswana and the U.S. (BARC) and model simulations (between the two dotted lines).	32
4.7	Average monthly composites of 1983 of day-time (A, C, E, and G) and night-time (B, D, F, and H) soil temperature at 5 cm depth of North America. A and B represent January, C and D April, E and F July and G and H October. The snow cover is also included and is indicated with black dots.	35
5.1	The theoretical relationship between MPDI and the vegetation optical depth for a range of soil dielectric constants ($h = 0$, $\omega = 0.06$, and $u = 50.3^\circ$). Typical soil moisture values of $0 \text{ m}^3 \text{ m}^{-3}$, $0.18 \text{ m}^3 \text{ m}^{-3}$, $0.26 \text{ m}^3 \text{ m}^{-3}$, $0.34 \text{ m}^3 \text{ m}^{-3}$, and $0.41 \text{ m}^3 \text{ m}^{-3}$ would correspond to dielectric constants of $k = 3, 8, 13, 18,$ and 23	39
5.2	A graphical presentation of the relationship between the absolute value of the dielectric constant of the soil (k) and the fitting parameters C_1 , C_2 , C_3 and C_4	40
5.3	Verification comparing the MPDI-optical depth relationship derived from the radiative transfer equation to calculation from simulated data ($h = 0$, $\omega = 0.06$, and $u = 50.3^\circ$).	41
5.4	A simplified diagram of the soil moisture retrieval methodology	42
5.5	Time series of satellite derived day-time (\circ) and night-time ($+$) soil moisture and ground observations ($*$) for the test sites. For comparison the precipitation is included for the American sites.	46
5.6	Time series of satellite derived day-time (\circ) and night-time ($+$) vegetation optical depth and NDVI ($-$) for the test sites. For comparison the precipitation is included for the American sites.	47
6.1	The standard deviation of the soil moisture as related the vegetation optical depth. Note the different relations for different moisture regimes	52
6.2	The Coefficient of Variation (CV) of the soil moisture as related to the vegetation optical depth. The relationship is separated in two different soil moisture classes, where (A) represents the dry soils with soil moisture values below $0.2 \text{ m}^3 \text{ m}^{-3}$ and (B) represents the wet soils with soil moisture values between 0.2 and $0.5 \text{ m}^3 \text{ m}^{-3}$. In Figure A the thick dots represent dry soils with soil moisture values below $0.1 \text{ m}^3 \text{ m}^{-3}$ and the thin dots soil moisture values between 0.1 and $0.2 \text{ m}^3 \text{ m}^{-3}$	53
6.3	The standard deviation of the vegetation optical depth as related to the soil moisture. Note the different relations for different vegetation types.	54
6.4	The coefficient of variation of the vegetation optical depth as related to the soil moisture. The relationship is separated in two different vegetation classes, where (A) represents sparse vegetation with optical depth values below 0.4 , and (B) represents dense vegetation with optical depth values between 0.4 and 0.8	55

7.1	Time series of the soil moisture from 6.6 GHz and 18 GHz for the 5 test sites.	63
7.2	Time series of the vegetation optical depth derived from 6.6 GHz and 18 GHz for the 5 test site.	64
7.3	The soil moisture derived from the 6.6 GHz signals versus the soil moisture from 18 GHz. $R^2 = 0.60$, S.E.E. = $0.06 \text{ m}^3 \text{ m}^{-3}$ for 1614 (n) points.	65
7.4	The vegetation optical depth derived from the 6.6 GHz signals versus the vegetation optical depth from 18 GHz. The dotted line indicates the 1:1 relation and the solid line the regression line. $R^2 = 0.81$, S.E.E. = 0.06 for 1614 (n) points.	65
7.5	The standard deviation of the vegetation optical depth as related to the soil moisture. These values are derived from the 5 test sites with the 18 GHz brightness temperatures.	66
7.6	The standard deviation of the soil moisture as related to the vegetation optical depth. These values are derived from the 5 test sites with the 18 GHz brightness temperatures.	66
8.1	A monthly composite of the vegetation optical depth for Australia during July 1983. This image clearly illustrates the boundary effect with the masked pixels (gray) along the coastlines and surrounding Lake Eyre in the south central site of Australia.	69
8.2	Global monthly composites of vegetation optical depth (A and B), NDVI (C and D), and LAI (E and F) representing January, and April respectively for 1983. Missing data are represented by the color gray	70
8.3	Global monthly composites of vegetation optical depth (A and B), NDVI (C and D), and LAI (E and F) representing July, and October respectively for 1983. Missing data are represented by the color gray	71
8.4	The land cover classification map developed by Defries and Townshend (1994)	72
8.5	Mean monthly precipitation (A, B, C, G, H and I) and soil moisture (D, E, F, J, K and L) composites from the Indian peninsula of 1983. This Figure represents the first six months.	76
8.6	Mean monthly precipitation (A, B, C, G, H and I) and soil moisture (D, E, F, J, K and L) composites from the Indian peninsula of 1983. This Figure represents the last six months.	77
8.7	Results of a statistical time series analysis of surface soil temperature (5 cm) retrievals from satellite microwave observations for the continental U.S. during the period 1978 to 1987. The left and right panels correspond with day-time and night-time observations respectively. Maps A and B illustrate the 9-year average temperature in Kelvin; C and D the seasonal amplitude of the mean monthly annual course in Kelvin; E and F the phase-shift (time of peak) with the unit being the date; G and H the long term trend (slope) in Kelvin per year. Five pixels (numbered) were selected for more detailed analysis.	80

List of Figures

8.8	Three thematic maps of the U.S. obtained from the LDAS web site (http://ldas.gsfc.nasa.gov/). These maps are a (A) vegetation classification map, (B) classification map of the soil texture type, and (C) elevation map. The description of the soil and vegetation classes can be found in Table 8.2.	81
8.9	Difference (in days) between the night-time (Figure 8.7 F) and daytime (Figure 8.7 E) phase-shift of the soil temperature at 5 cm depth.	82
8.10	The time series of the soil surface temperature for the 5 selected pixels (as marked in Figure 8.7). The circles in combination with the dashed line represent the satellite derived monthly average T_s values at 5 cm depth, and the solid line is the time series analysis model.	83

List of Tables

3.1	Characteristics of the SMMR instrument.	16
3.2	Characteristics of the extracted Oklahoma Mesonet field stations.	19
5.1	Polynomial parameters that describe the relation between the absolute value of the dielectric constant of the soil (k) and the fitting parameters C_1, C_2, C_3 and C_4 (See Equation 5.3).	40
6.1	Contribution of the input parameters in the total standard deviations of the soil moisture and vegetation optical depth. Note, the soil moisture values (θ) are in $\text{m}^3 \text{m}^{-3}$	57
8.1	Median vegetation optical depth (τ), NDVI, and LAI values for different land covers derived from the Mean, Maximum and Minimum monthly images of 1983	73
8.2	Description of the soil and vegetation classes, as given in Figure 8.8.	81

Chapter 1

GENERAL INTRODUCTION

1.1 Background

Interest in the link between human activity and climate change is currently high, however researchers today are only rediscovering an old concept. George Perkins Marsh (1874) voiced his concern over the ability of man to alter the Earth's climate, *i.e.* soil moisture, precipitation, temperature, and atmosphere by modifying the surface vegetation and hydrologic regime through clearing, planting, irrigation, and draining wetlands, but was unable to provide much data in support of his theory. Thornthwaite (1956) recognized the importance of this hypothesis, and indicated the causal conditions for climatological change, such as changes in the general circulation of the atmosphere, variation in incoming radiation and changes in the Earth's features.

Nowadays there is strong evidence that human activity has disturbed the natural climate, providing a remarkable acceleration in global warming, sea level rise, deforestation, and desertification. In order to monitor these environmental changes, there is a distinct need for long term spatially distributed land surface data sets, like soil moisture, soil temperature and vegetation.

Satellite remote sensing can be a powerful tool in fulfilling those needs, because it can monitor and compute environmental processes in both spatial and temporal terms. Since the early sixties, satellites have provided useful data for water resources management. During this period, visible and infrared were used to observe snow cover, surface water areas, land use and surface temperature (Schmugge, 1985). However, a major drawback of these instruments was their sensitivity to atmospheric contaminants. The occurrence of clouds and water vapor could easily disturb the signals, resulting in limited land surface information.

In the seventies, some scientists started to discover the promising possibilities of microwave instruments onboard of satellites. They observed that low frequency microwave signals penetrate clouds and are able to provide physical information of the land surface.

In 1975 Wilheit developed one of the first radiative transfer models that described the physics of microwave radiation in the soil. This important step in microwave research started a series of papers on the possibilities of retrieving soil moisture through

microwave radiometry.

In 1977 Njoku and Kong described one of the first soil moisture models. These models started to become more complex with a surface roughness model (Choudhury et al., 1979), more sophisticated canopy layers (Kirdiashev et al., 1979; Mo et al., 1982), and better dielectric mixing models (Wang and Schmugge, 1980; Dobson et al., 1985). However, limitations in computing and lack of validation data frequently delayed research progress. Now, 20 years later research in this field has evolved, resulting in more physically based models (Njoku and Li, 1999; Owe et al., 2001). A couple of years ago we were only able to estimate satellite derived soil moisture for a few selected sites. However as demonstrated in this dissertation, we are now capable to generate reliable global soil moisture data bases.

1.2 Thesis Objective and Approach

The primary objective of the present study is to develop a methodology to estimate the land surface parameters soil moisture, soil temperature and vegetation optical depth on a global basis by using passive microwave remote sensing. The methodology should be general, in a way that it does not require any field observations of soil moisture or canopy biophysical properties for calibration purposes, and that it can be used with microwave observations at different wavelengths.

The study starts by first analyzing microwave theory. This analysis results in the development of a simple physically based land surface retrieval model. The model is tested on 5 test sites in the US and Eurasia and the resulting land surface parameters are compared to field measurements and evaluated with an error propagation analysis. The functionality of the model is tested by applying it to different wavelengths. Finally the model is used on the global Nimbus/SMMR passive microwave data set and various applications of the retrieved land surface parameters are discussed.

1.3 Thesis Outline

The thesis consists of a series of papers. However, in order to minimize redundancy, and to give the thesis a more logical structure, some papers are revised and combined to form a single chapter.

Chapter 1 provides a descriptive outline, general introduction to microwave remote sensing, and thesis objective and approach. Chapter 2 provides a background in passive microwave theory, and Chapter 3 gives a description of the data sets used in the present study. The method used to derive soil temperatures is described in Chapter 4, while the soil moisture and vegetation optical depth retrieval technique is described and applied to 6.6 GHz observations in Chapter 5. Chapter 6 discusses the limitations of the land surface parameter retrievals through error propagation analysis and the implementation of a masking routine. Chapter 7 describes the application of the methodology to higher frequency (18 GHz) data. Chapter 8 discusses the potential applications of the land surface data sets, while Chapter 9 provides research conclusions and offers suggestions for follow-on research.

Chapter 2

MICROWAVE THEORY

2.1 Introduction

Passive microwave theory has been described in considerable detail by a number of authors (*e.g.* Njoku and Kong, 1977; Ulaby et al., 1982, 1986). This section gives a brief overview of the theory relevant to the present study.

Passive microwave remote sensing is based on the measurement of thermal radiation from the land surface in the centimeter wave band, and is largely determined by the physical temperature and the emissivity of the radiating body. The emitted radiation in the microwave region ($\lambda = 1\text{-}1000$ mm) is extremely low as compared with longwave infrared radiation ($\lambda = 1\text{-}100$ μm).

An approximation for the Planck equation, at low frequencies ($f < 117$ GHz), is the Rayleigh-Jeans approximation, and can be shown to lead to

$$T_{b(l)} \approx e_{s(l)}T \quad (2.1)$$

Where l refers to either horizontal or vertical polarization, T_b is the observed microwave brightness temperature, T is the physical (thermodynamic) temperature of the emitting layer, and e_s is the smooth-surface emissivity. If the assumption is made that the dielectric constant in the soil has a smooth boundary and that the temperature and surface moisture distributions are uniform, the reflectivity, R (where $R = 1 - e_s$), may be calculated from the Fresnel equation

$$R_H = \left| \frac{\cos u - \sqrt{\varepsilon - \sin^2 u}}{\cos u + \sqrt{\varepsilon - \sin^2 u}} \right|^2 \quad (2.2)$$

and

$$R_V = \left| \frac{\varepsilon \cos u - \sqrt{\varepsilon - \sin^2 u}}{\varepsilon \cos u + \sqrt{\varepsilon - \sin^2 u}} \right|^2 \quad (2.3)$$

where ε is the complex dielectric constant of a soil-water mixture ($\varepsilon = \varepsilon' + \varepsilon''i$), u is the incidence angle of the sensor and V and H refer to the polarization of the emitted radiation. To simplify the mathematics in this thesis, the complex dielectric constant of the soil-water mixture will often be expressed as k , which is the absolute value of

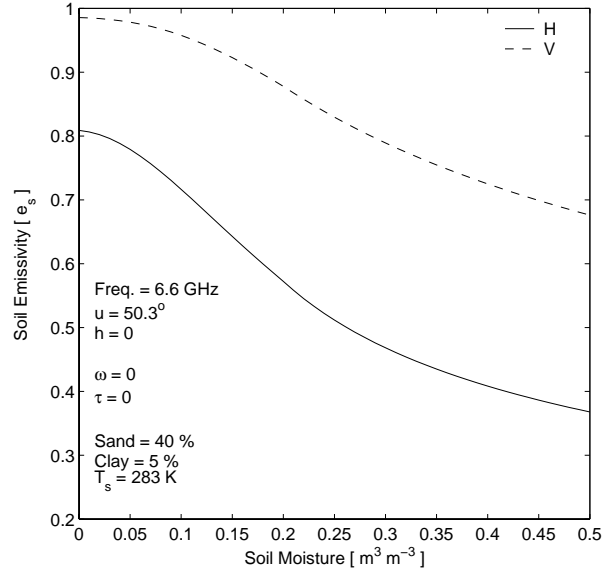


Figure 2.1: Comparison of horizontal and vertical polarized emissivity calculated for an average soil at the SMMR wavelength and incidence angle with no canopy cover.

the dielectric constant ($|\varepsilon| = k$).

While the absolute magnitude of the soil emissivity is somewhat lower at horizontal polarization, the sensitivity to changes in surface moisture is significantly greater than at vertical polarization (See Figure 2.1). Conversely, at vertical polarization, the sensitivity to surface temperature is greater. This subsequently forms the basis for a surface temperature estimation procedure (Owe and Van de Griend, 2001), which is later discussed in Chapter 4.

2.2 Dielectric Constant

The microwave region is the only part of the electromagnetic spectrum that permits truly quantitative estimates of soil moisture using physically based expressions such as radiative transfer models. Microwave technology is also the only remote sensing method that measures a direct response to the absolute amount of water in the surface soil.

The basis for microwave remote sensing of soil moisture follows from the large contrast in dielectric constant of dry soil ($k \approx 4$) and water ($k \approx 80$) and the resulting dielectric properties of soil-water mixtures ($k = 4-40$) and their effect on the natural microwave emission from the soil (Schmugge et al., 1986). The dielectric constant is an electrical property of matter and is a measure of the response of a medium to an applied electric field. The dielectric constant is a complex number, containing a real (ε') and an imaginary (ε'') part. The real part determines the propagation charac-

teristics of the energy as it passes upward through the soil, while the imaginary part determines the energy losses (Schmugge et al., 1986).

The dielectric constant is a difficult quantity to measure in the field. Moreover, reproducing precise field conditions in laboratory soil samples makes laboratory analysis of the dielectric constant not entirely straightforward. Consequently, the validation of theoretical calculations is often somewhat difficult.

Dielectric models which are commonly used in theoretical calculations are the Dobson Model (Dobson et al., 1985), a modified version of this model developed by Peplenski et al. (1995) and the Wang-Schmugge Model (Wang and Schmugge, 1980).

In 1998 Owe and Van de Griend compared the Dobson and the W-S model and they concluded that W-S model had better agreement with the laboratory dielectric constant measurements. Consequently, for this study the W-S model was chosen and a description of this model can be found in Appendix A.

2.3 Soil Physical Properties

In a non-homogeneous medium such as soil, the complex dielectric constant is a combination of the individual dielectric constants of its components (*i.e.* air, water, rock, etc.). In a soil medium, the dielectric constant is determined largely by the moisture content, temperature, salinity, textural composition, and frequency.

The relationship between the soil dielectric constant and the moisture content is almost linear, except at low moisture contents (See Figure 2.2). This non-linearity at low moisture contents is due to the strong bonds which develop between the surfaces of the soil particles and the thin films of water which surround them. These bonds are so strong at low moisture levels, that the free rotation of the water molecules is impeded. This water is often referred to as bound water. Therefore, in a relatively dry soil, the water is tightly bound and contributes little to the dielectric constant of the soil water mixture.

As more water is added, the molecules are further from the particle surface and are able to rotate more freely. This is referred to as the free water phase. The subsequent influence of the free water on the soil dielectric constant therefore also increases.

Smaller particles such as irregular fine sands, silts, and clays have a higher surface area-to-volume ratio and therefore are able to hold more water molecules at higher potentials.

The unique plate-like structure of clays provides an additional source of high energy bonds and increases the soil's affinity for water.

Two soils with different textural composition may exhibit markedly different relationships between moisture content and their respective soil dielectric constants. Soils with a high clay content will generally have a lower dielectric constant than coarse sandy soils at the same moisture content, since more water is being held in the bound water phase (See Figure 2.2).

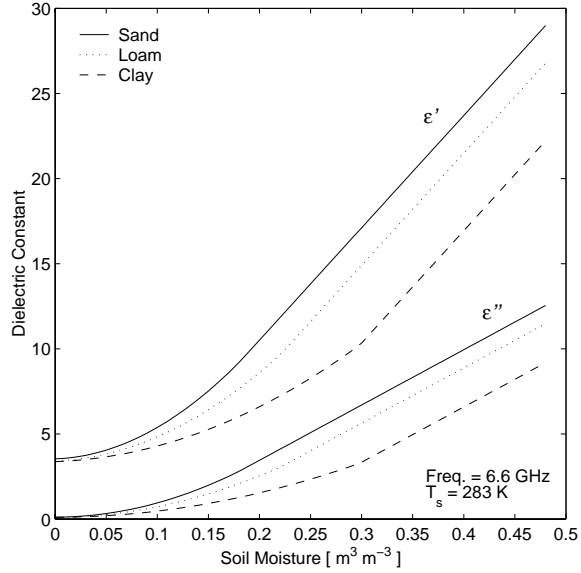


Figure 2.2: Comparison of the soil dielectric constants for typical sand, loam, and clay soils. The real part is designated by ϵ' and the imaginary part by ϵ'' .

2.4 Thermal Sampling Depth

Microwave energy originates from within the soil, and the magnitude of any one soil layer's contribution decreases with depth. For practical purposes, the total thickness of the surface layer which provides most of the measurable energy contribution is defined as the thermal sampling depth (Schmugge and Choudhury, 1981). This term is often confused with the skin depth or penetration depth.

Skin depth is defined as the depth over which the wave amplitude has attenuated by a factor $\frac{1}{e}$ and penetration depth is the depth over which the power or intensity is attenuated by a factor $\frac{1}{e}$. The skin depth is half of the penetration depth (Ulaby et al., 1982; Van Oevelen, 2000).

The sampling depth is influenced mainly by the total complex dielectric constant discontinuity at the surface and the near surface dielectric constant gradient. For a uniform dielectric profile with depth this is what determines the Fresnel reflection coefficients. The penetration depth on the other hand has more to do with the imaginary part of the dielectric constant which leads to loss and attenuation in the medium, thus determining the depth in the medium from which most of the radiation originates that reaches the surface (E. Njoku, Pers. Comm.).

It is thought that the sampling depth is only several tenths of a wavelength (Schmugge, 1983).

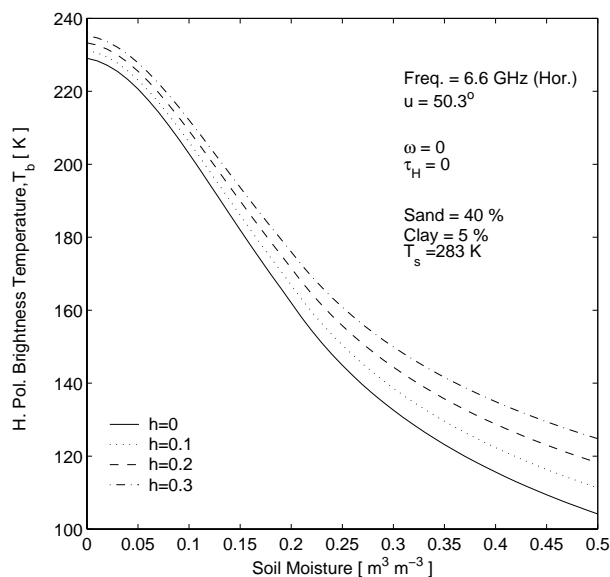


Figure 2.3: Horizontal polarized brightness temperature calculated for a range of roughness values using Equation 2.4.

2.5 Surface Roughness

Surface roughness increases the apparent emissivity of natural surfaces, which is caused by increased scattering due to the increase in surface area of the emitting surfaces (Schmugge, 1985). Roughness also reduces the sensitivity of emissivity to soil moisture variations, and thus reduces the range in measurable emissivity from dry to wet soil conditions (Wang, 1983).

Furthermore, the path through the atmosphere between the surface and the sensor depends on the elevation and also slope of the emitting surface. However this effect is only significant at frequencies which are affected by atmospheric attenuation (> 10 GHz, Mätzler and Standley, 2000).

In 1959 Peake developed a theoretical approach to modify the reflectivity ($e_s = 1 - R$) for rough surfaces. This approach provided insight into scattering mechanism and required deriving expressions for the scattering coefficients. The scattering coefficients could be estimated with two surface parameters, the height standard deviation and the horizontal correlation length and many approaches to derive the theoretical expressions for emissivity have been developed using these two parameters (*e.g.* Fung and Eom, 1981; Tsang and Newton, 1982; Tsang et al., 1985). Although they provided insight into the scattering mechanisms these expressions were not easy to use, as they require detailed knowledge of the soil surface height and slope statistics, and their computational accuracy is often limited in practical situations (Njoku and Entekhabi, 1996).

A simpler, empirical roughness model was developed by Choudhury et al. (1979), and

is described as

$$e_{r(l)} = 1 - R_{(l)} \exp(-h \cos^2 u) \quad (2.4)$$

where e_r is the rough surface emissivity, h is an empirical roughness parameter, related to the root mean square (rms) height variation of the surface and the correlation length, and u is the incidence angle of the observation.

Typical values for h have been suggested, ranging from 0 for a smooth surface, 0.3 for a disked field, to 0.4 for a rough ploughed field. A more elaborate formulation, which also included a polarization mixing parameter, has subsequently been proposed by Wang and Choudhury (1981). However, little work has since been conducted to quantify the relative magnitudes of either the roughness parameter or the polarization mixing parameter. The effects of frequency and incidence angle on the roughness parameter have also not been studied thoroughly.

The effect of roughness on the observed microwave brightness at 6.6 GHz for a range of surface moistures is illustrated in Figure 2.3. A change in the roughness parameter from 0 to 0.3 corresponds to a difference in the surface emissivity, of about 0.005 at dry conditions, to about 0.014 at saturation.

There is some speculation that the effect of surface roughness is minimal in most locations at satellite scales, except in areas of mountainous terrain or extreme relief. Van de Griend and Owe (1994a) found that a surface roughness of 0 gave the lowest rms errors in satellite-derived soil moisture over a southern African test site.

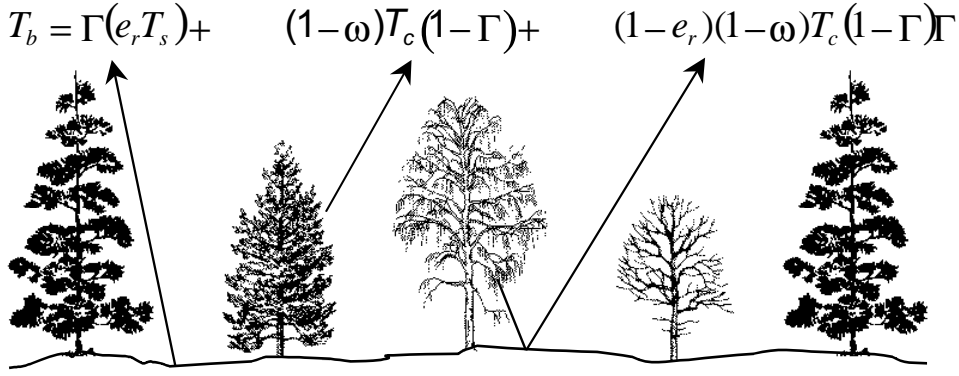
2.6 Vegetation Effects

The effects of vegetation on the microwave emission as measured from above the canopy are two-fold. The vegetation may absorb or scatter the radiation emanating from the soil, but it will also emit its own radiation. In areas of sufficiently dense canopy, the emitted soil radiation will become masked, and the observed emissivity will be due largely to the vegetation. The magnitude of the absorption by the canopy depends upon the wavelength and the vegetation water content.

The most frequently used wavelengths for soil moisture sensing are in the L- and C-bandwidths ($\lambda \approx 21$ cm and 5 cm, respectively), although only L-band sensors are able to penetrate vegetation of any significant density. While observations at all frequencies are subject to scattering and absorption and require some correction if the data are to be used for soil moisture retrieval, shorter wave bands are especially susceptible to vegetation influences.

Numerous canopy models have been developed to account for the effects of vegetation (Kirdiashev et al., 1979; Mo et al., 1982; Ulaby et al., 1986; Theis and Blanchard, 1988). For this study the model of Mo et al. (1982) is used because this model has proven to be a simple but physically based model that can effectively estimate the radiation by the soil surface even under vegetation (Van Oevelen, 2000). The upwelling radiation from the land surface as observed from above the canopy may be expressed in terms of the brightness temperature, T_b , and is given as a simple radiative transfer equation (Mo et al., 1982),

$$T_{b(l)} = T_s e_{r(l)} \Gamma_{(l)} + (1 - \omega_{(l)}) T_c (1 - \Gamma_{(l)}) + (1 - e_{r(l)}) (1 - \omega_{(l)}) T_c (1 - \Gamma_{(l)}) \Gamma_{(l)} \quad (2.5)$$



Γ = Transmissivity of the vegetation, e_r = Rough surface emissivity, T_s = Surface temperature, ω = Single scattering albedo, and T_c = Canopy temperature.

Figure 2.4: Schematic representation of the partitioning of microwave radiation from a vegetation covered surface in terms of the brightness temperature (From Van de Griend and Owe (1993)).

Where T_s and T_c are the thermometric temperatures of the soil and the canopy respectively, ω is the single scattering albedo, and Γ the transmissivity of the canopy. The first term of the above equation defines the radiation from the soil as attenuated by the overlying vegetation.

The second term accounts for the upward radiation directly from the vegetation, while the third term defines the downward radiation from the vegetation, reflected upward by the soil and again attenuated by the canopy. These three terms are summarized in Figure 2.4. The transmissivity (Γ) is defined in terms of the optical depth τ , such that

$$\Gamma(l) = \exp \frac{-\tau(l)}{\cos u} \quad (2.6)$$

The canopy optical depth is related to the vegetation density and the frequency. For frequencies less than 10 GHz, it has been shown to be a linear function of vegetation water content. Typical values of τ for agricultural crops have generally been given as less than one (Mo et al., 1982; Jackson and O'Neill, 1990a).

Theoretical calculations show that the sensitivity of above-canopy brightness temperature measurements to variations in soil emissivity decreases with increasing optical depth or canopy thickness (Ulaby et al., 1986). This is because the soil emission is attenuated by the canopy and emission from the vegetation canopy tends to saturate the signal with increasing optical depth. This subsequently results in decreased sensor sensitivity to soil moisture variations.

A transmissivity of 1 corresponds to an optical depth of 0, indicating bare soil, or at least no attenuation of the soil-emitted radiation due to an overlying canopy. Conversely, a transmissivity of 0 indicates an infinitely thick canopy, with no penetration of the soil emission through the canopy.

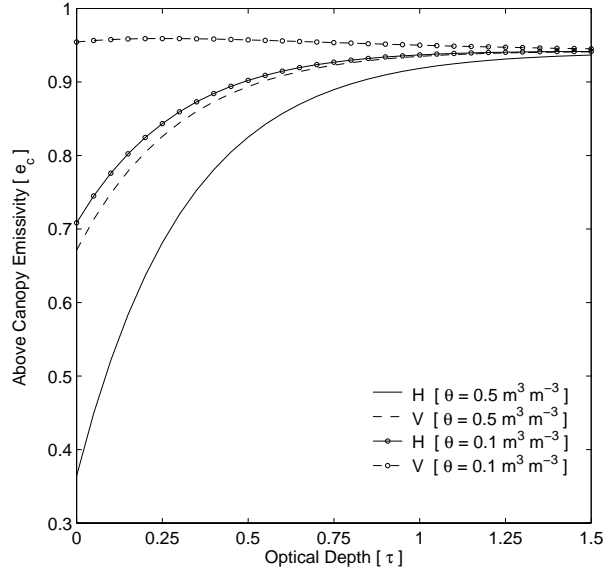


Figure 2.5: The effect of the vegetation optical depth on the emissivity. At H-polarization, the sensitivity of the above canopy emissivity is severely reduced at an optical depth of about 0.75 ($\Gamma = 0.3$).

It is also shown in Figure 2.5, that at C-band, the above-canopy signal becomes totally saturated at an optical depth of about 1.5 in the horizontal channel, although for practical purposes, the sensitivity of C-band measurements to optical depth variations significantly decreases when the optical depth is higher than 0.75. Under dry conditions, this threshold occurs even sooner. The relationships between other indicators of vegetation biomass or canopy density, such as leaf area index (LAI), vegetation water content (VWC), Microwave Polarization Difference Index (MPDI) and Normalized Difference Vegetation Index (NDVI) have been reported in a variety of studies (Becker and Choudhury, 1988; Holben et al., 1980; Tucker et al., 1980), but are largely empirical in nature. Theoretical calculations indicate that at C-band, sensitivity to changes in surface moisture conditions ceases at a maximum VWC of approximately 1.5 kg m^{-2} (Njoku and Li, 1999).

The single scattering albedo describes the scattering of the emitted radiation by the vegetation. The scattering albedo is a function of plant geometry, and consequently varies according to plant species and associations. Experimental data for this parameter are limited, and values for selected crops have been found to vary from 0.04 to about 0.12 (Brunfeldt and Ulaby, 1984; Jackson and O'Neill, 1990b; Mo et al., 1982). Values for natural vegetation are even more scarce, although Becker and Choudhury (1988) estimated a value of 0.05 for a semi-arid region in Africa. Van de Griend and Owe (1994b) calculated a 3-year time series of both scattering albedo and vegetation optical depth at both 6.6 GHz and 37 GHz for savanna surfaces in Botswana.

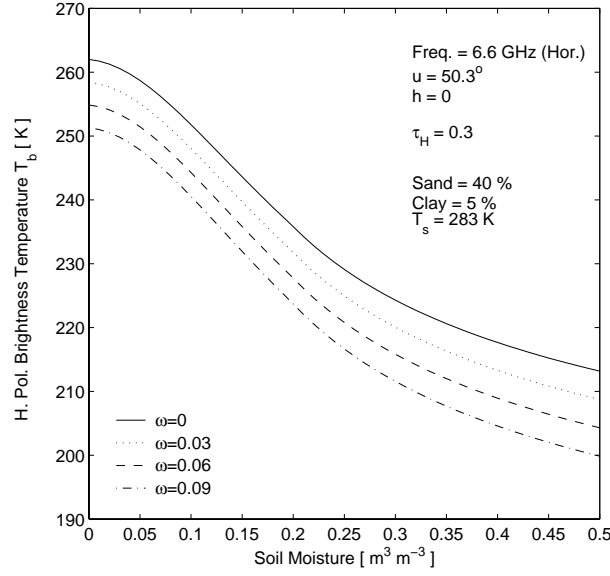


Figure 2.6: The effect of the single scattering albedo on the soil moisture brightness temperature relationship.

The optical depth displayed a distinct seasonal course at both frequencies, although the values for 37 GHz were significantly higher. While the scattering albedo demonstrated considerable variability during the 3-year period, a relationship with vegetation biomass or other seasonal indicators was not observed. An average value for the scattering albedo of 0.076 was found for both frequencies. The effect of the scattering albedo on the observed brightness temperature-surface moisture relationship is illustrated in Figure 2.6, over a range of values reported in the literature.

The influence of polarization on the optical depth and the scattering albedo has also received relatively little attention. There is, however, some experimental evidence that differences in the transmissivity at horizontal and vertical polarization are dependent on incidence angle. These differences are observed mainly over vegetation elements that exhibit some systematic orientation such as vertical stalks in tall grasses, grains, and maize (Ulaby et al., 1986; Van de Griend and Owe, 1994a; Van de Griend et al., 1996). At a nadir (0°) incidence angle, the stalks are not visible, and appear only as small randomly oriented disks. However, as the incidence angle increases, the stalks become more prominent, resulting in an increased effect on vertically polarized emissions.

In general, the canopy and stem structure for most crops and naturally occurring vegetation are assumed to be randomly oriented. While it may be reasonable to assume that the optical depth is for the most part polarization independent, especially at satellite scales, additional validation is provided. The validation analysis is an important step in the current thesis and will be described in a separate section below.

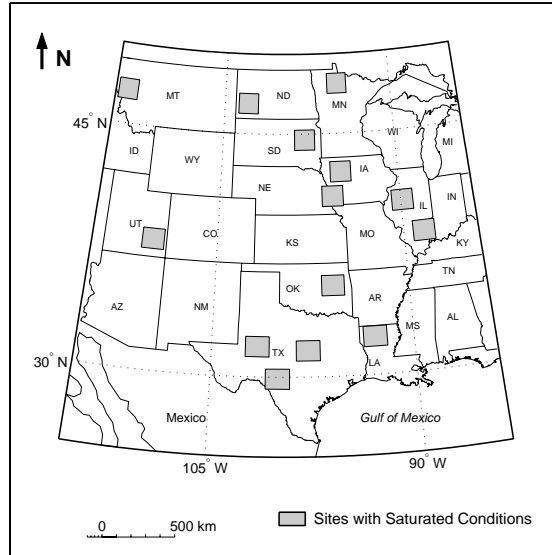


Figure 2.7: Locations of SMMR footprints used to calculate the vertical and horizontal optical depth at saturated conditions.

2.7 Dependence of Polarization on Vegetation

Validation was performed by analyzing areas where the surface soil moisture was known, namely areas of saturation. Daily and hourly precipitation records throughout the midwestern United States were analyzed for the entire SMMR period (1978-1987) for exceptionally large storms.

The criteria was that these storms not only had to deposit large amounts of water to ensure saturation of the surface, but they also had to cover an extensive geographic area, to ensure near complete coverage of the SMMR footprint (≈ 150 km). Storm events with greater than 30 mm average precipitation for an entire footprint in a 24-hour period were selected. All gauging stations within the footprint must have recorded rain during the period. An additional stipulation was that a satellite overpass had to occur between 4 and 8 hours after the end of the precipitation event.

The footprint locations used in this analysis are given in Figure 2.7 and cover a range of canopy types and densities. Assuming complete saturation of the surface, and knowledge of the soil porosity and texture, the soil emissivity can be assessed using a dielectric model (Wang and Schmugge, 1980), as described in Appendix A, and the Fresnel equations (Equation 2.2 and 2.3). The radiative transfer equation (Equation 2.5) is then inverted and solved for the optical depth, for both vertical and horizontal polarization.

It is shown that when τ_H and τ_V are plotted together (See figure 2.8), they fall very close to the 1:1 line, supporting the assumption that the optical depth is independent of polarization for a random canopy.

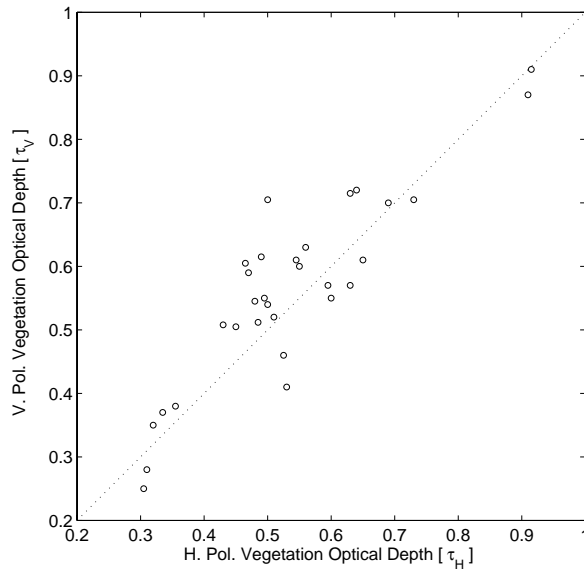


Figure 2.8: Relationship between vertical and horizontal optical depth.

2.8 Atmosphere

Electromagnetic radiation emitted from the ground surface may interact with the atmosphere in two ways as it propagates to a satellite radiometer. These are interactions between the electromagnetic radiation and 1) atmospheric gases (primarily oxygen and water vapor) and 2) water droplets existing in clouds and rain.

The primary interaction mechanism is that of absorption of energy by the atmosphere. However, for frequencies below 15 GHz the effects are quite small, and for frequencies below 10 GHz the effects are negligible. The effect of water droplets in clouds and rain may be somewhat more significant, and depends largely on two factors; 1) the phase state of the particles (*i.e.* ice or liquid) and 2) the size of the particle relative to the wavelength (Chahine, 1983; Ulaby et al., 1982).

In addition to the atmospheric effects on the emitted surface radiation, there is also a sky background radiation component, which is reflected back to the observing instrument, and also a direct atmospheric component. Each of these components is further affected (attenuated) by the atmospheric transmissivity.

As stated before, these effects are relatively small at longer wavelengths and in Chapter 4 the influence of the atmosphere in the microwave region will be discussed in greater detail.

Chapter 3

DESCRIPTION OF DATA SETS

3.1 Satellite Data

3.1.1 Nimbus-SMMR

The microwave data used to retrieve the land surface parameters is from the Scanning Multichannel Microwave Radiometer (SMMR) on board the Nimbus-7 satellite (Gloersen and Barath, 1977).

The instrument began transmitting data in October of 1978, and was eventually deactivated in August of 1987. Due to power constraints on board the satellite, the SMMR instrument could only be activated on alternate days. The polar orbiting satellite circled the Earth approximately 14 times in one day, with a local noon (ascending orbit) and midnight (descending orbit) equator crossing, and a swath width of about 780 km. The incidence angle was 50.3° .

Brightness temperatures were measured at five frequencies, from 6.6 GHz to 37 GHz (See Table 3.1 for more details) at both horizontal and vertical polarization, resulting in ten different channels.

Although complete coverage of the Earth required about 6 days, sufficient overlapping occurred at the mid-latitudes, to result in repeat coverage over small sites about 2 to 3 times per week. The 24 hour on-off cycle of the instrument permitted both day and night observations.

The spatial resolution of SMMR was rather coarse, ranging from approximately 25 km at 37 GHz, to 150 km at 6.6 GHz.

The original SMMR data were obtained from the Marshall Space Flight Center Distributed Active Archive Center (DAAC). Orbit brightness temperatures were extracted and stored into daily $\frac{1}{4}$ degree global maps. If a pixel center fell within a grid, then the grid is assigned the brightness value. If multiple pixel centers fell within a $\frac{1}{4}$ degree grid, then all the brightness values within the grid were averaged. Separate day-time and night-time data sets were created.

For this study, only the brightness temperatures for land surface were used. Brightness temperatures of water bodies were masked out. Water bodies have significantly lower brightness temperatures and are easy to detect and eliminate prior to the analysis.

Frequency GHz	Wavelength (λ) cm	Spatial Resolution km	Accuracy K
6.6	4.5	150	0.7
10.7	2.8	90	0.8
18.0	1.7	55	0.9
21.0	1.4	45	1.0
37.0	0.8	25	1.4

Table 3.1: Characteristics of the SMMR instrument.

The low resolution of Nimbus/SMMR microwave signatures (See Table 3.1) together with the sampling grid of $\frac{1}{4}$ degree ($\approx 25 \times 25 \text{ km}^2$) results in a relatively broad band along the coast of the water bodies. This band is easily 100 km (east-west direction) and 75 km (north-south) for 6.6 GHz although it is much narrower at higher frequencies. At 37 GHz, for instance, this band is approximately 25 km (east-west) and 17 km (north-south). This is called the boundary effect and is the primary cause of mixed pixels. Because of the mathematical complexity due to the inherent irregularity of coastlines in combination with the elliptical shape of the measuring footprint, these pixels were also eliminated.

In Central Europe the 6.6 GHz signals are extremely high and are probably disturbed by external radio signals. Therefore the 6.6 GHz data in this area is useless for soil moisture and vegetation retrieval and is masked out for this study.

3.1.2 TRMM

The Tropical Rainfall Measuring Mission (TRMM) is a joint research program between the National Aeronautics and Space Administration (NASA) of the United States and the National Space Development Agency (NASDA) of Japan.

In November 1997, the satellite was launched and placed in a low earth orbit of 350 km. The primary sensor onboard this spacecraft is the TRMM Microwave Imager (TMI), a passive microwave instrument. The vertical polarized 37 GHz signals measured with this instrument were used in this study.

The swath width for this instrument is 760 km with an incidence angle of 52.8° . The spatial resolution at this channel is $16 \times 9 \text{ km}$.

For this study, two years of data (*i.e.*, 1998, 1999) near the 8 Oklahoma Mesonet Stations (See section 3.2.3), were selected. In order to select the TRMM data, the assumption was made that the brightness temperature could be compared with the soil temperature if the scanning center of the instrument was between ± 0.02 degrees longitude and latitude boundary of the location of the Oklahoma Mesonet station.

The temporal resolution of the radiometer was 2 times per day on average.

3.1.3 NOAA-AVHRR

Estimation of land surface vegetation properties from satellite observations is mostly based on the spectral properties of the vegetation. Spectral measurements in the visible region ($\lambda = 0.4\text{-}0.70 \mu\text{m}$) are sensitive to the chlorophyll content of vegetation, while measurements in the near infrared ($\lambda = 0.73\text{-}1.1 \mu\text{m}$) are sensitive to the mesophyll structure of leaves (Townshend et al., 1993).

Vegetation strongly absorbs the visible part and strongly reflects near infrared radiation. Therefore a normalized ratio has a good response to vegetation activity and the Normalized Difference Vegetation Index (NDVI) has become the most commonly used index today. It is defined as:

$$NDVI = \frac{\rho_{nir} - \rho_{red}}{\rho_{nir} + \rho_{red}} \quad (3.1)$$

Where ρ_{red} is the land surface reflectance in the red band ($\lambda = 0.58\text{-}0.68 \mu\text{m}$) in the visible domain and ρ_{nir} is the land surface reflectance in the near infrared.

The NDVI data is derived from the Advanced Very High Resolution Radiometer (AVHRR) on board the NOAA-7, -9, -11, and -14 satellites.

The AVHRR data was adjusted for sensor degradation, volcanic aerosol effects, cloud contamination, short-term atmospheric effects, solar zenith angle variations, and missing data (Los et al., 2000).

The data set begins in 1981 and continues through the present. Over North America, the data consists of 8 km spatial resolution and 15 day temporal resolution, while the remainder of the globe has a spatial resolution of 1 degree with a monthly temporal resolution.

3.2 Land Surface Data

3.2.1 Vegetation

3.2.1.1 Leaf Area Index

Global, monthly, 1 by 1 degree Leaf Area Index (LAI) is obtained from the Goddard Space Flight Center (<http://islscp2.gsfc.nasa.gov/>) International Satellite Land Surface Climatology Project (ISLSCP) Initiative II. The data set covers a time period from 1982 to 1990.

The LAI is generally defined as one-sided green leaf area per unit ground area in the plant canopy (Chen and Black, 1992). It plays an important role in studies of global climate and biochemical cycles. The LAI is especially important with respect to the global carbon cycle, with about a quarter of atmospheric carbon dioxide potentially fixed as gross primary production by terrestrial vegetation annually (Myneni et al., 1995).

The LAI data set was derived from data collected by the AVHRR on board the NOAA-7, -9, -11, and -14 satellites. The data was processed on a similar way as the NDVI data set and the methodology to derive the LAI from NOAA AVHRR data is described in detail by Los et al. (2000).

3.2.1.2 Land Cover Classification Map

The global land cover classification map used in this study was developed by Defries and Townshend (1994). They used monthly NDVI images in a supervised maximum likelihood technique to obtain 11 land covers. The spatial resolution of this map is 1 by 1 degree and may be found on the ISLSCP CD-ROM (Meeson et al., 1995; Sellers et al., 1995).

For the United States, the $\frac{1}{8}$ degree vegetation classification map from the Land Data Assimilation System website (LDAS, <http://ldas.gsfc.nasa.gov/>) is used. This classification map is based on the 1 km land classification map of the University of Maryland (Hansen et al., 2000) and the 1 km classification map of the International Geosphere Biosphere Programme (Eidenshink and Faundeen, 1994).

They developed a first predominant vegetation type map with 13 classes by counting up the number of occurrences of a particular type of vegetation (1 km scale) within an $\frac{1}{8}$ degree grid box, and then dividing this number by the total number of 1 km pixels in an $\frac{1}{8}$ degree box.

3.2.2 Soil Properties

Soil physical property data such as texture and hydraulic properties were obtained from the Land Data Assimilation System (LDAS) website at $\frac{1}{8}$ degree resolution for the U.S. (Houser et al., 2000; Mitchell et al., 2000), and from the ISLSCP one degree global soil property maps for the remainder of the world (Meeson et al., 1995; Sellers et al., 1995; Zobler, 1986).

The LDAS soil data set was derived from the 1 km Penn State State Soil Geographic (STATSGO; USDA, 1994) data base and the 5 minute data of the United States Department of Agriculture (USDA) Agriculture Research Service (ARS) and the Food and Agriculture Organization (FAO). These soil maps were compiled by generalizing more detailed soil survey maps. Where more detailed soil survey maps were not available, data on geology, topography, vegetation, and climate were assembled, together with Land Remote Sensing Satellite (LANDSAT) images.

The LDAS soil type maps were converted to soil characteristic maps (*i.e.* porosity, wilting point, sand content, and clay content) with Rawls conversion table (Rawls et al., 1998). For this study the soil properties of the first 5 cm layer are used.

The ISLSCP global map was derived from the FAO soil map of the world (1974-1981), scale 1:5,000,000. This global soil type map was converted to soil characteristics by Zobler (1986).

The $\frac{1}{8}$ degree elevation map of the US was also obtained from LDAS. The topographic data set is based on the GTOPO30 Global 30 Arc Second (≈ 1 km) Elevation Data Set. This set was distributed by the EROS (Earth Resources Observation System) Data Center Distributed Active Archive Center (EDC DAAC), located at the U.S. Geological Survey's EROS Data Center in Sioux Falls, South Dakota.

In particular, average elevation values over the United States were derived by isolating the relevant subset of data from the 1 km global data set, and then averaging up to the $\frac{1}{8}$ degree resolution values.

St. Name	Longitude	Latitude	Alt.(m)	Soil Type
Stilwater	97° 09' 50" W	36° 12' 11" N	272	Silty Clay Loam
Marena	97° 21' 28" W	36° 06' 44" N	331	Sandy Clay Loam
Perkins	97° 04' 81" W	35° 99' 83" N	292	Loam
Acme	98° 00' 56" W	34° 80' 56" N	397	Sandy Loam
Goodwell	101° 60' 14" W	36° 60' 17" N	996	Loam
Seiling	99° 04' 06" W	36° 19' 03" N	540	Loam
Nowata	95° 60' 78" W	36° 74' 36" N	206	Silt Loam
Wister	94° 68' 81" W	34° 98' 47" N	143	Silt Loam

Table 3.2: Characteristics of the extracted Oklahoma Mesonet field stations.

3.2.3 Soil Temperature

3.2.3.1 Oklahoma Mesonet

The Oklahoma Mesonet is a network of environmental monitoring stations and consists of 114 automated stations covering the state of Oklahoma. Every station has a 10-m high meteorological tower on a protected 100 square meter area (10 by 10 meter).

For this study we extracted two years (*i.e.* 1998, 1999) of soil temperature and soil moisture information at 5 cm depth at 8 stations with different soil characteristics at 30 minute temporal resolution.

A summary description of the stations can be found in Table 3.2 and the geographical location of these sites is shown in Figure 3.1 B. All 8 stations have a grassland cover. More information of this set can be found at <http://okmesonet.ocs.ou.edu/>.

3.2.3.2 BARC

Numerous field experiments have been conducted at the USDA Beltsville Agricultural Research Center (BARC) in Maryland located at 39° 03' N and 76° 85' W (See Figure 3.1 B). One of the first experiments was carried out during October 1979 over bare and vegetated fields. In this period, soil temperature measurements were made at several depths, 0-2.5 cm and 10-12.5 cm. Several different types of fields were included in the measurements (*e.g.* bare, grass, soybean and corn). This experiment is described in detail by Wang et al. (1980).

Another experiment was conducted during July-September of 1980. During this period soil temperatures were measured at depths of approximately 0.25 cm, 1.25 cm, 2.5 cm, 7.5 cm and 15 cm under several types of cover types. These types were bare, grass, soybean, and corn. The data set and a detailed description of the set can be found in Wang et al. (1982).

The third experiment was conducted during June-September 1982. Observations of soil temperature were made at 1 cm, 3 cm and 7.5 cm depth under a bare soil, grass, soybean, sorghum, alfalfa, wheat, and corn (O'Neill et al., 1983).

The temporal resolution of these three sets was irregular, but on average, measure-

ments were made weekly, with several observations made on a given measurement day.

In order to compare these three experiments with the Oklahoma Mesonet 5-cm temperature set, they were adjusted with linear interpolation to temperature measurements at 0.2 cm, 0.5 cm, 1.25 cm and 5 cm depth.

3.2.3.3 Botswana

Soil temperature data was collected at the Agricultural Research Station at Sebele (24° 34' S, 25° 57' E, altitude 994 m, see Figure 3.1 C) since September, 1975 under the direction of the Dryland Farming Research Scheme in collaboration with the Agricultural Research Station and Botswana Meteorological Services (Dryland, 1984).

Until June 1983 the soil temperature was measured daily at three stations at 8:00 hr and 14:00 hr under a bare soil and a short-grass cover at 1.75 cm, 10 cm and 60 cm depth.

In order to compare soil temperature values with the other data sets the temperatures at 0.2 cm, 0.5 cm, 1.25 cm and 5 cm depths were estimated using a linear interpolation technique.

3.2.4 Soil Moisture

Soil moisture data for the five test sites were obtained from the Global Soil Moisture Data Bank (<http://www.envsci.rutgers.edu/~robock>). Two locations from Eurasia (Turkmenistan and Mongolia) and three from the U.S. (one in Iowa and two in Illinois) were used (See Figure 3.1 B and D for the locations).

Observations were made mostly in grassland and agricultural areas. For each of the test sites, the 6.6, 18 and 37 GHz observations covering the field stations were extracted from the SMMR data set and the 18 and 37 GHz signals (*i.e.* these signals had a resolution of approximately 55 and 25 km, respectively) were converted to the 6.6 GHz footprint (≈ 150 km) with a nearest neighbor interpolation technique.

Descriptions of the field data sets can be found below, and in Robock et al. (2000).

3.2.4.1 Illinois

The Illinois data set was compiled by the Illinois State Water Survey (Hollinger and Isard, 1994). The data consisted of 0-10 cm total surface moisture measurements at 19 stations from 1981 to 1996. Six of these stations were used for this study, three in a northern test site and three in a southern test site. The geographical location of these stations are for the northern site: 40° 92' N, 90° 73' W; 40° 70' N, 89° 52' W; 40° 97' N, 90° 15' W, and for the southern site: 38° 95' N, 88° 95' W; 38° 73' N, 88° 10' W; 38° 13' N, 88° 92' W.

The soil moisture was measured by neutron probe and calibrated with gravimetric observations. The measurements were biweekly from March through September and monthly during the winter. The vegetation cover at all stations was grass.

The northern 150 km footprint test site consists almost entirely of farms, with about

60 % cropland, 10 % grasses, and about 30 % woodlands. Urban or built-up areas and surface water account for less than 1 % each. Soils are generally poorly drained fine to medium textured silt loams to silty clay loams. The topography is nearly flat to gentle undulating.

The southern site is also largely farm land, with about 40 % crops, 25 % woodlands, and the remainder in pasture and grasses. Urban area and surface water again account for less than 1 % each. Soils are for the most part well drained moderately fine to medium textured silt loams.

The annual precipitation for the northern site is approximately 900 mm per year and for the southern site 1100 mm per year.

3.2.4.2 Iowa

The Iowa data set is developed by the state University of New Jersey, University of Maryland and the USDA-ARS-National Soil Tilth Laboratory. The data consisted of a range of 0-7.5 cm total surface moisture measurements at 6 stations. The stations were located close to each other (*i.e.* ≈ 200 m) in two different catchments, located at 41° 20' N, 95° 60' W in the southwestern part of the state. Each catchment has three sites where soil moisture observation were taken. The soil moisture was measured using a gravimetric technique, and recorded in percent wetness by weight. The record of observations begins in 1972 and continues until 1994. The observations were made between April and October, on average twice a month.

Within the Iowa footprint 10 % is woodland and forest and 90 % is arable land in a flat area. The main soil type (90 %) is silty clay loam with silt loam soils (10 %) along the Missouri River. The annual precipitation is about 850 mm per year.

3.2.4.3 Russia

This set consists of gravimetric measurements of soil moisture from 130 meteorological stations located in the former Soviet Union, during the period 1978-1985. The measurements were taken in the upper 10 cm soil layer with a natural grass type vegetation. The observational plots were about 0.1 ha. in size, and contained four sampling locations in each plot. The four samples were averaged to yield a mean value for the plots. Observations were made three times per month during the warm season, and once a month during the winter. For this study, a station in the dry Kara Kum desert of Turkmenistan (coordinates 37° 30' N, 62° 42' E) was selected. Approximately 15 % of the footprint is covered with woodland and forests. The other 85 % is mainly grassland and shrub with cotton farms (< 5 %) along the Murgab river. The soils are mainly well drained loamy sands. The annual precipitation of the test site is roughly 200 mm per year.

3.2.4.4 Mongolia

The Mongolian data set consists of 42 stations for the period 1970-93. Twenty-five sites have pasture vegetation and 17 have wheat. All the observations were made using the gravimetric technique for the upper 10-cm layer. The station used in the

validation is located at 44° 05' N, 103° 33' E. Soil moisture was observed three times a month, on the 7th, 17th and 27th of each month from April until the end of October. The vegetation within the footprint is sparse and consists mainly of desert grass and shrub with a silt loam soil. Satellite derived vegetation indices show that there is no seasonal variation in the vegetation. This site is the driest of all the location studies with an annual precipitation of less than 200 mm a year. The topography of this test site is flat.

3.3 Atmospheric Data

3.3.1 Precipitation

Precipitation data for the U.S. originates from the National Climate Data Center (NCDC), however, a commercial version available on CD ROM (EarthInfo, 1993; EarthInfo, 1994) was used for this study. The data set can be divided into daily and hourly observations of precipitation. Both daily (18,770 stations) and hourly (6,801 stations) precipitation totals are compiled by cooperative stations throughout all fifty states and U.S. territories. Daily precipitation data for the period 1978 to 1987 was used.

Mean monthly global precipitation of 1983 was developed by the Climate Research Unit (CRU) of the University of East Anglia. The set has a 0.5 degree spatial resolution and is based on 19,800 precipitation stations. The station data were interpolated as a function of latitude, longitude and elevation using thinplate splines. The dataset is described in detail by New et al. (1999) and can be obtained at the Intergovernmental Panel on Climate Change (IPCC) Data Distribution Centre (DDC) (<http://ipcc-ddc.cru.uea.ac.uk>).

3.3.2 Clouds

The International Satellite Cloud Climate Project (ISCCP) began as part of the World Climate Research Program (WCRP) in 1982. Data have been collected since 1 July, 1983. More than 150 cloud related variables are retrieved from visible and infrared satellite data and stored in a 280 km equal area grid in the ISCCP-D1 data set every three hours.

Only the precipitable water for the entire atmosphere was used to investigate the influence of the atmosphere on the passive microwave signals for this study. More information on the cloud data set can be obtained from Rossow and Schiffer (1991) and documentation is available at the following URL:

<http://isccp.giss.nasa.gov/documents.html>.

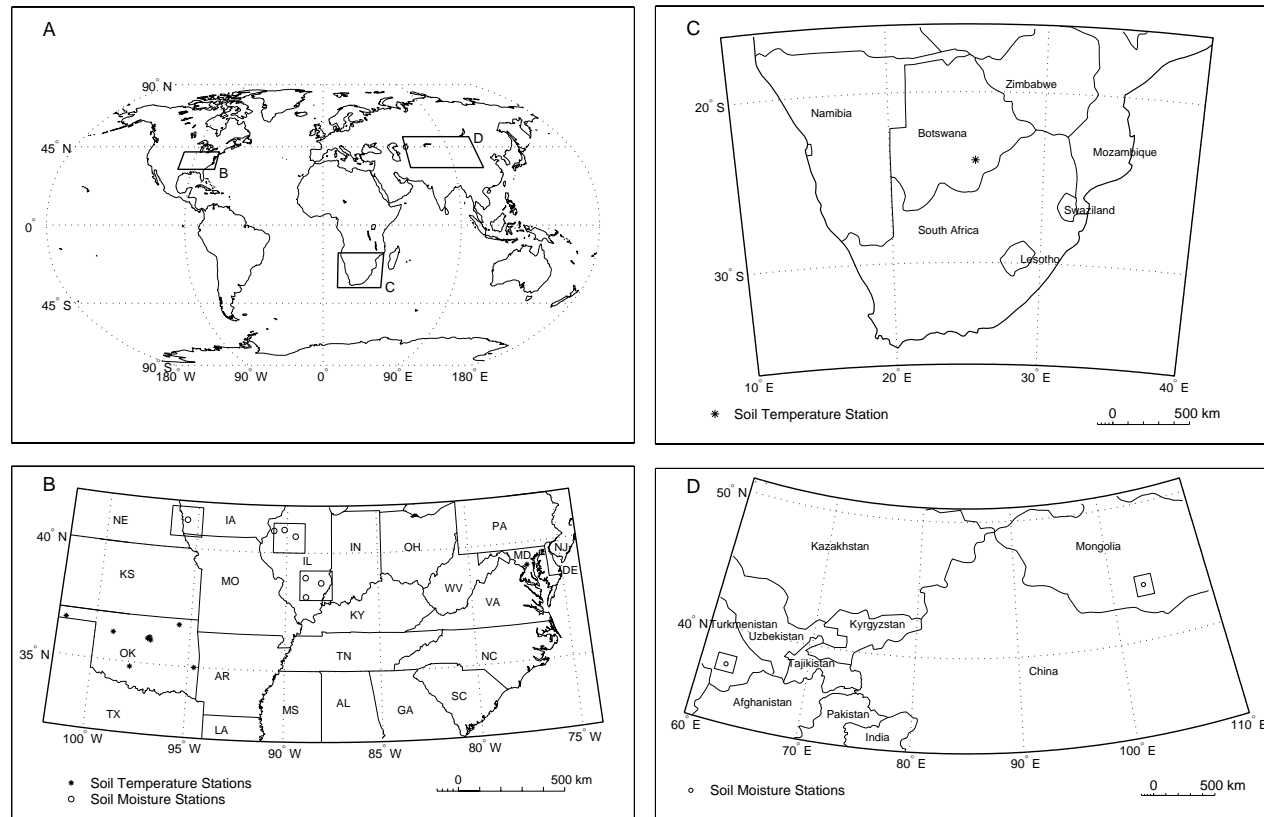


Figure 3.1: Location maps of the field stations. Figure (A) is a global overview, (B) shows the U.S. sites, (C) the African site and (D) the Eurasian sites.

Chapter 4

DERIVATION OF SURFACE SOIL TEMPERATURES

This chapter is based on:

De Jeu, R.A.M., and M. Owe (2002). Estimating Spatially Averaged Surface Soil Temperature for Microwave Surface Moisture Derivation. *Remote Sensing of Environment*. Submitted.

4.1 Introduction

Surface soil temperature describes the energetic state of the soil. It is an important prognostic (or state) variable in land surface processes models and an input parameter in radiative transfer models. In this study surface temperature is especially important for normalizing microwave radiobrightness temperatures in inverse radiative transfer modelling methods for soil moisture and vegetation optical depth retrieval (Owe et al., 2001 and Chapter 5). Therefore, there is a distinct need for accurate estimates of surface soil temperature in environmental modelling.

In order to use these models on a regional or a global scale spatially averaged data is necessary. The variability of surface temperature in space and time is extremely high and is a function of incoming solar radiation, air temperature, vegetation, soil physical properties, and topography.

Traditional techniques have used point measurements of air temperatures and soil temperatures to derive spatially averaged surface soil temperature, but they introduce large errors because of variability in space.

Thermal infrared (TIR) remote sensing provides spatially averaged values of physical skin temperature. However, TIR measurements always need atmospheric correction and the accuracy of the sensors decreases significantly when there is cloud cover.

Microwave remote sensing also has the potential for providing reliable estimates of spatially averaged surface soil temperature (Calvet et al.,1996; Njoku and Li, 1999; Van de Griend et al., 1998; Owe and Van de Griend, 2001;Van de Griend, 2001). The great advantage of microwave instruments compared to TIR sensors is that they are much less affected by atmospheric conditions and thus require little or no correction (See Section 2.8). However, the main drawback is the need to estimate surface

emissivity that depends on soil moisture through the dielectric constant (See Equation 2.1).

This study presents a technique to estimate the effective temperature by using vertical polarized 37 GHz radiobrightness temperatures.

First the contribution of the atmosphere on this signal is tested. Then a procedure is presented, which demonstrates the relationship between the 37 GHz signal and soil temperature at 5 cm depth and the influence of soil moisture on this relationship. A relationship was developed between soil temperature at 5 cm depth with soil temperature at 1.25 cm depth. With the temperature at 1.25 cm depth it was possible to generate a temperature algorithm that estimates the temperature of the emitting layer at 6.6 GHz, which is an important input parameter in the soil moisture and optical depth retrieval models. The satellite derived soil temperatures at 5 cm depth were validated with North American snow cover maps.

In addition, the modelled soil temperatures of the 6.6 GHz emitting layer are used in the passive microwave based soil moisture and vegetation optical depth model which is described in Chapter 5.

4.2 Atmospheric Effects

The influence of the atmosphere increases with increasing frequency. In this chapter the 37 GHz vertical polarized brightness temperatures will be used to derive surface soil temperatures. To understand the magnitude of the atmospheric influence on this signal, two areas were selected where the vegetation and soil moisture did not change significantly during the year (*e.g.*, deserts). This means that for these areas, changes in the apparent emissivity were mainly caused by changes in the atmosphere.

The arid Mongolian test site and a footprint in the Libyan part of the Sahara Desert (footprint center was 25° 12' 50" N, 13° 62' 50" E) were used. SMMR brightness temperatures at different frequencies were extracted for these two sites. Because of differences in footprint size, the higher resolution data was first registered to the 6.6 GHz pixel size by using a nearest neighbor interpolation technique.

Choudhury et al. (1992) indicated that microwave data is sensitive to the precipitable water, so for the same test sites the precipitable water was extracted from the D1 ISCCP data set.

The ratio between horizontal and vertical brightness temperature was used to eliminate the influence of the surface temperature. Figures 4.1 and 4.2 show that water in the atmosphere significantly influences the brightness temperature ratio at frequencies above 10 GHz.

However it is still not clear if the atmosphere causes anomalies in the horizontal or vertical signals. To find out which one is affected most, the assumption is made that the emissivity at long wavelengths (*i.e.* 6.6 GHz) does not change for these test sites, because the atmosphere does not affect these signals.

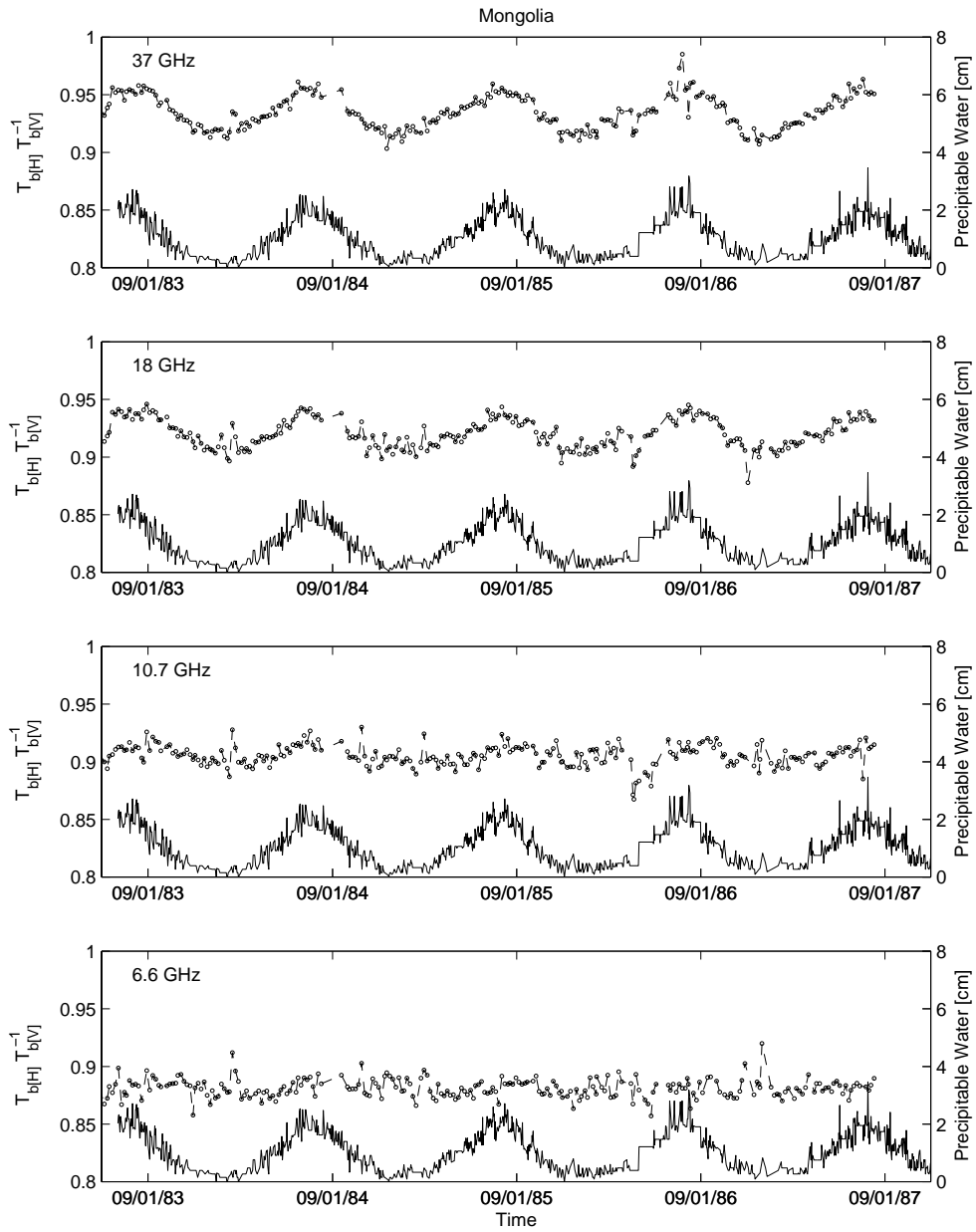


Figure 4.1: Time series of the brightness temperature ratio (-o-) at different wavelengths and the precipitable water (-) for the Mongolia test site

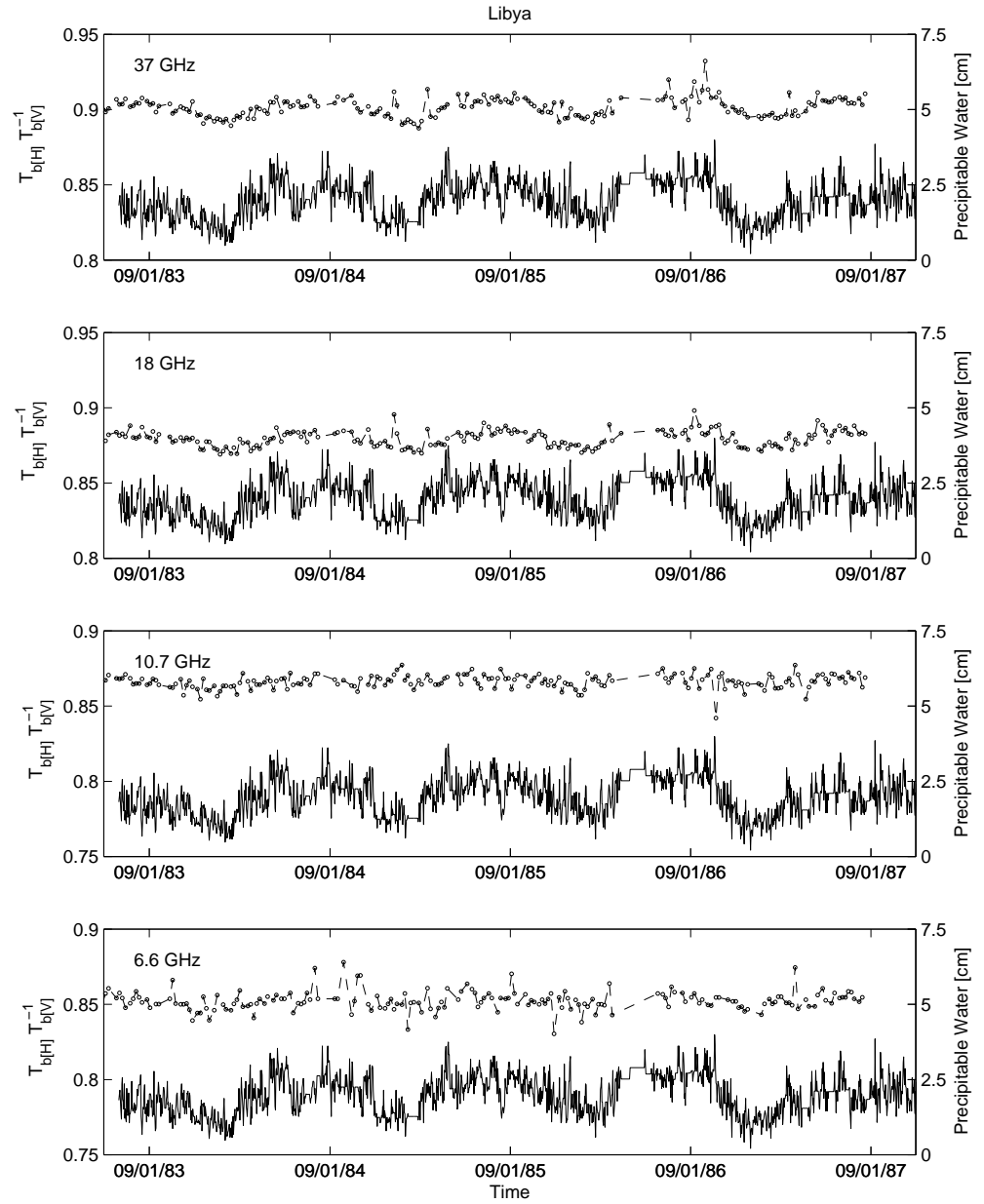


Figure 4.2: Time series of the brightness temperature ratio (-o-) at different wavelengths and the precipitable water (-) for the Libya test site

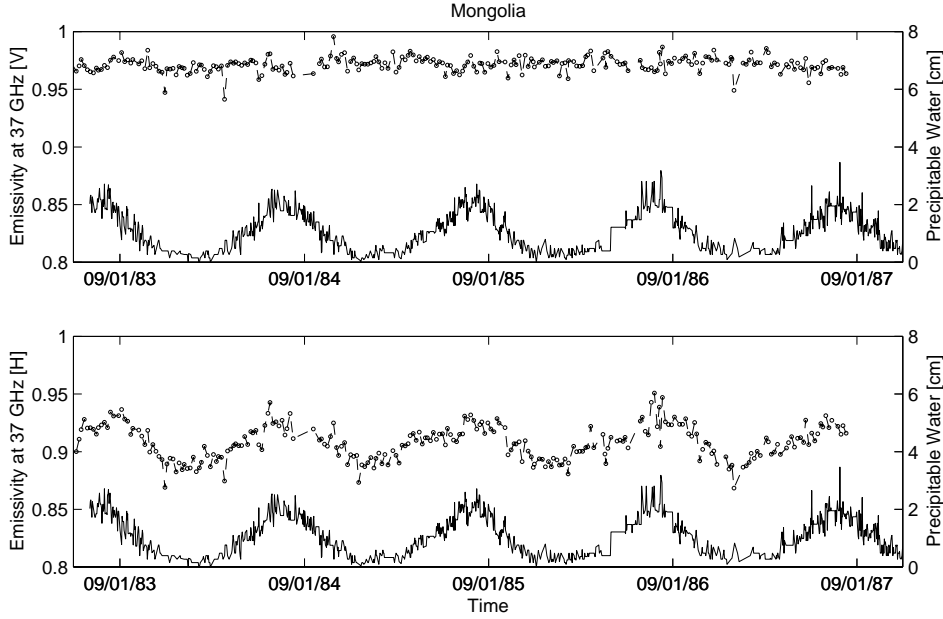


Figure 4.3: Time series of the vertical (top) and horizontal (bottom) emissivity at 37 GHz (-o-) and the precipitable water (-) for the Mongolia test site

For the vertical polarization, the emissivity is set to 0.98. This value is estimated with the W-S model (See Appendix A) using the soil characteristics derived from the ISLSCP data set and a fixed soil moisture value of $0.03 \text{ m}^3 \text{ m}^{-3}$.

The soil temperature also changes the soil emissivity, but for these test sites the changes are negligible.

The temperature of the emitting layer at 6.6 GHz can now be estimated with Equation 2.1. The temperature of the emitting layer, T_s , is equal to the soil temperature at a depth of approximately 28 % of the wavelength (Schmugge, 1983), which is 0.2 cm for 37 GHz and 1.25 cm for 6.6 GHz. By using linear interpolation with the Botswana and BARC data sets, the following conversion was made and the temperature of the emitting layer at 37 GHz was estimated as

$$T_{s[0.2cm]} = T_s = 1.039T_{s[1.25cm]} - 11.380 \quad (4.1)$$

where $T_{s[0.2cm]}$ is the temperature of 0.2 cm depth and indicates the temperature of the emitting layer at 37 GHz. The verification to use this kind of linear models to obtain soil temperatures from different depths can be found in the next section. Now the emissivity at 37 GHz can be calculated for both the horizontal and vertical polarization.

Both Figure 4.3 and 4.4 show that mainly the horizontal polarized brightness temperature is influenced by the atmosphere. The vertical brightness temperature, which is the one used in the surface temperature algorithm is not significantly influenced by

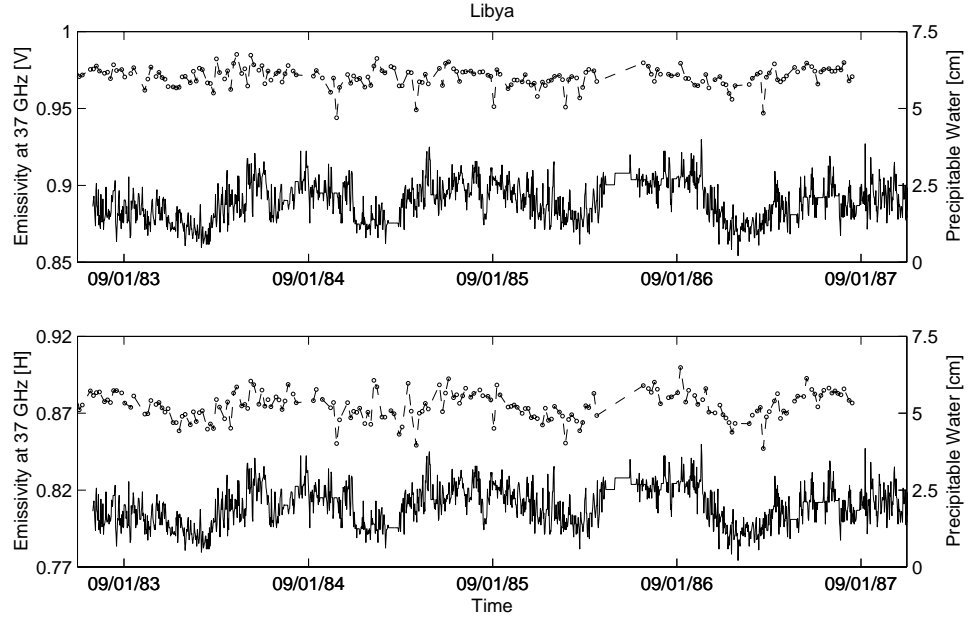


Figure 4.4: Time series of the vertical (top) and horizontal (bottom) emissivity at 37 GHz (-o-) and the precipitable water (-) for the Libya test site

the atmosphere.

4.3 Surface Soil Temperature Model

As already indicated in the previous sections, it is assumed that the temperature of the emitting layer, T_s , is equal to the soil temperature at a depth of approximately 28 % of the wavelength. The temperature of these depths are rarely measured in the field and an algorithm had to be developed to estimate these temperatures in order to estimate T_s .

Previous papers (Owe et. al., 1999; Owe and Van de Griend, 2001; Owe et al., 2001) indicated that the vertical polarized 37 GHz can be used to estimate the temperature of the emitting layer at 6.6 GHz. In these papers it has been shown that the emissivity of the vertical polarized 37 GHz signal approaches it's maximum value of about 0.96 at the incidence angles of TRMM and SMMR, which are 52.8° , and 50.3° , respectively.

Although the emissivity decreases with soil moisture, it is still above 0.9, even at saturation. Consequently, the effect of moisture at this frequency and polarization is small and the emissivity is predominantly a function of the physical surface temperature.

To compare the 37 GHz brightness temperature to soil temperature measurements, it is necessary to have field observations at the same time and location of the satellite

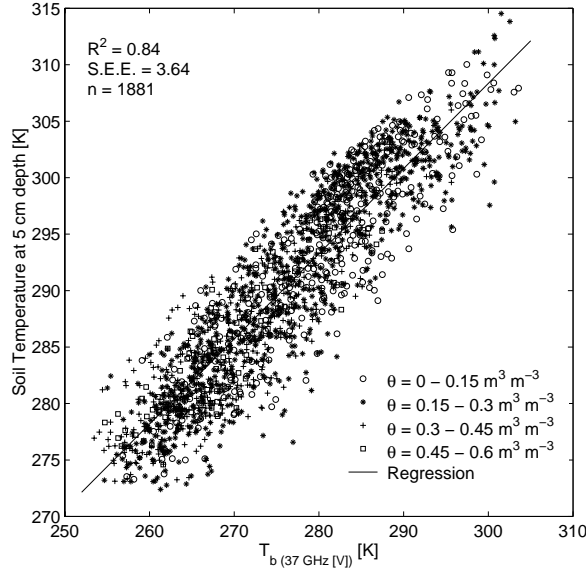


Figure 4.5: Relation between the vertical polarized brightness temperature at 37 GHz and the soil temperature at 5 cm depth for different soil moisture conditions. Note that the influence of soil moisture on the linear relationship does have a random character.

overpass.

Soil temperatures at 5 cm depth were selected from 8 stations in Oklahoma. These stations were compared to the vertical polarized 37 GHz brightness temperatures from the TRMM satellite. TRMM footprints close to the Oklahoma field stations were selected. This procedure was described in Section 3.1.2. Soil temperature values at the moment of the overpass were calculated by using a simple linear interpolation between the 30-minute interval.

When using all of the 8 Oklahoma field stations the general linear relationship between soil temperature at 5 cm depth and vertical polarized brightness temperature at 37 GHz can be described as:

$$T_{s[5cm]} = 0.754T_{b(37GHz[V])} + 82.043 \quad (4.2)$$

Where $T_{s[5cm]}$ is the soil temperature at 5 cm depth and $T_{b(37GHz[V])}$ is the vertical polarized brightness temperature at 37 GHz, both in degrees Kelvin.

This relationship had a R^2 of 0.84, and a Standard Error of Y Estimated (S.E.E.) of 3.64 K for 1881 measuring points (n). Figure 4.5 gives a graphical presentation of this relationship.

Differences in soil wetness and soil type did not appear to have a recognizable influence on this relationship and the observed scatter of the graph is mainly caused by upscaling problems. The Oklahoma soil temperature measurements are point measurements whereas the brightness temperature measurements are spatially averaged values.

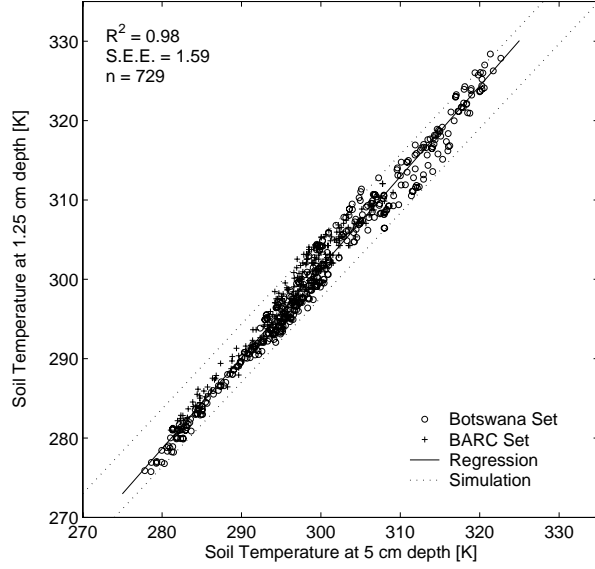


Figure 4.6: The relationship between soil temperature at 5 cm depth and 1.25 cm depth according to field observations in Botswana and the U.S. (BARC) and model simulations (between the two dotted lines).

A relationship between 1.25 and 5 cm is necessary to get reliable estimates of the temperature of the emitting layer at 6.6 GHz.

To obtain such a relationship one can use a soil temperature model such as the one described by McCulloch and Penman (1956). Such a soil temperature model can be used to model the diurnal and annual variation of soil temperature in depth. This study was focussed on the annual variation because the satellite overpass was always at the same hour of day (*i.e.* noon and midnight). The soil temperature can be modelled as

$$T_{(z,t_d)} = T_{ave} + A_0 \exp\left(-\frac{z}{D}\right) \sin\left(w_d t_d - \frac{z}{D}\right) \quad (4.3)$$

Where $T_{(z,t_d)}$ is the soil temperature in Kelvin at z cm depth as a function of time t_d in days, T_{ave} is the average annual temperature at the surface, A_0 is the amplitude of the annual surface temperature fluctuation in Kelvin, and w_d the frequency in days⁻¹ ($w_d = \frac{2\pi}{365}$).

D is the damping depth, at which the temperature amplitude decreases to the fraction of $\frac{1}{\exp(1)}$ (≈ 0.37) of the amplitude at the soil surface A_0 . The damping depth is related to the thermal properties of the soil and the frequency of the temperature fluctuation. The damping depth for annual variation varies between 50 cm for a peat soil to 300 cm for a sandy soil (Van Wijk, 1963).

Equation 4.3 can be used for two different depths (*i.e.* z_1 and z_2) and by combining these two soil temperature equations for those two depths with the assumption that $z \ll D$, the soil temperature at z_1 can be approached as a function of

the soil temperature at z_2 as

$$T_{(z_1, t_d)} = T_{(z_2, t_d)} + A_0 \frac{z_2 - z_1}{D} (\sqrt{2} \cos(w_d t_d - \frac{\pi}{4})) \quad (4.4)$$

The absolute error of this equation will be in the order of $\frac{z^2}{D^2}$.

Numerous simulations can be made with Equation 4.4 for several soils to estimate soil temperature at 1.25 cm for given soil temperatures at 5 cm depth. With these simulations it has been shown that by looking at the annual temperature variation, the relationship between soil temperature at 1.25 cm and 5 cm will always be between two boundaries and has a relationship which is almost linear for a large variety of soils. The boundaries are indicated with dotted lines in Figure 4.6.

With field data from the BARC and Botswana data set, as described in Section 3.2.3.2 and 3.2.3.3, it can be seen in the same Figure that the field observations fell within these two boundaries. According to the field data the linear relationship between the soil temperatures at two different depths was

$$T_{s[1.25cm]} = 1.142T_{s[5cm]} - 41.143 \quad (4.5)$$

For this study this equation was used for the estimation of the temperature of the emitting layer at 6.6 GHz instead to the soil temperature model (Equation 4.4) because of lack of information on the damping depth.

Combining Equations 4.2 and 4.5, the relationship between the vertical polarized 37 GHz observations and 1.25 cm soil temperature is calculated and given below

$$T_{s[1.25cm]} = T_s = 0.861T_{b(37GHz[V])} + 52.550 \quad (4.6)$$

This Equation was used globally for this study to calculate the temperature of the emitting layer at 6.6 GHz.

However, one should keep in mind that this relationship is only based on measurements in Oklahoma, Maryland and Botswana.

The incorporation of additional data sets of coupled soil temperature and brightness temperature at 37 GHz at different locations in combination with the soil temperature model (Equation 4.4) will most likely improve this empirical linear relationship and efforts to locate such data sets are currently in progress.

4.4 Validation of the Model

Validation of the retrieved surface soil temperatures is performed by separate approaches.

First, the soil temperature retrievals are compared to snow cover maps of North America. The position of the snow cover boundary will be compared to the satellite derived freezing temperature (273 K) boundary.

The second approach uses the soil moisture retrieval model described in Chapter 5 to validate the temperature algorithm. The satellite derived temperatures of the emitting layer at 6.6 GHz are put in the soil moisture and optical depth retrieval models, and the resulting time series of day-time and night-time soil moisture and

optical depth values are compared.

The surface temperature is a very sensitive parameter in the soil moisture and optical depth retrieval model and miscalculation of the surface temperature will result in wrong estimates of soil moisture and vegetation optical depth.

Consequently, if the day-time and night-time soil moisture and optical depth retrievals coincide well with each other, one could say that the temperature algorithm is reliable and will enhance the soil moisture and vegetation data set by using both day-time and night-time data. In Chapter 5 the results of the latter validation technique will be described.

4.5 Results

The temperature model was verified by comparing the temperature fields with snow cover maps. Equation 4.2 was used on monthly averaged day-time and night-time composites of SMMR vertical polarized 37 GHz brightness temperatures to model the soil temperature at 5 cm depth.

Monthly maps of North America were made for the months January, April, July and October for 1983. These composites were compared with snow cover maps from the same period. The difference in horizontal polarized brightness temperatures between the SMMR 37 GHz and 18 GHz is used to derive these maps. According to the difference algorithm of Chang et al. (1987) there is snow cover if

$$(T_{b(18GHz[H])} - T_{b(37GHz[H])}) > 0 \quad (4.7)$$

The Figures 4.7 A through H present the combination of the temperature maps with snow cover maps.

In January, the snow cover boundary is roughly at the US/Canadian border with exception of the Rocky Mountains and some northern states of the US, like North Dakota, South Dakota, and Iowa. Temperatures below 273 K can also be found in similar places and along the Mississippi river in the southern part of the US.

In April the snow cover retreats in northern direction. Most of the snow disappeared in the Rocky Mountains and along the eastern shore of Quebec (Canada). The soil temperature starts to increase, especially in Mexico, where the day time soil temperature easily exceeds 293 K.

In July, there is almost no snow on the North American continent, with exception of a few spots in Alaska. The soil temperature reaches its maximum in the central part of the U.S. In Mexico the temperature starts to decrease again.

In October the snow cover appears first in Alaska. The soil temperature decreases along the entire continent, with exception of some areas along the eastern and western shore of Mexico.

In general the day-time and the night-time composite temperature values below 273 K coincide well with the snow cover maps, so it seems that the soil surface temperature algorithm gives reliable estimates.

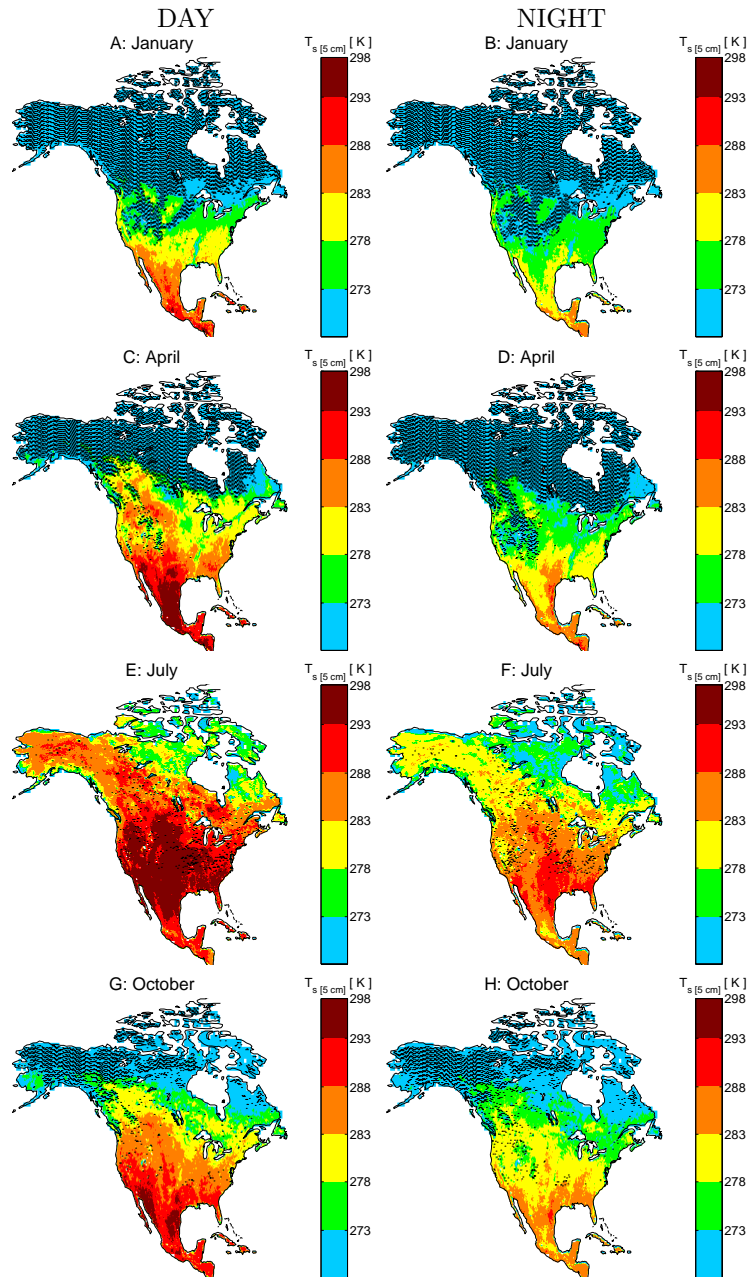


Figure 4.7: Average monthly composites of 1983 of day-time (A, C, E, and G) and night-time (B, D, F, and H) soil temperature at 5 cm depth of North America. A and B represent January, C and D April, E and F July and G and H October. The snow cover is also included and is indicated with black dots.

4.6 Conclusions and Discussion

Surface temperature is an important parameter in a variety of environmental studies especially in climate modelling. However, this parameter is seldom measured at climate stations, and soil temperatures derived from numerical models possess a low level of accuracy and are frequently prone to large errors. Even if there are field measurements, they still are point measurements and they don't provide the spatially distributed mean that are usually required.

Remote sensing seems to be a promising tool for obtaining spatially representative surface temperatures. The traditional technique for measuring surface temperature is thermal infrared. However, a huge disadvantage of this technique is that clouds and other atmospheric phenomena disturb and quite often completely mask the signal.

Passive microwave remote sensing seems to be a more promising tool, because the atmosphere affects the microwave signals much less.

According to some previous studies the vertical polarized 37 GHz brightness temperature possesses potential to estimate this parameter. These observations are preserved in a 23-plus year historical global database, that begins with Nimbus SMMR in 1978 and extending to the present with SSM/I and TRMM.

These data are ideal for long-term climate studies and other physically based land processes applications.

A method for using the vertical polarized 37 GHz brightness temperatures to estimate land surface temperature has been presented. It has been shown that the precipitable water in atmosphere does not markedly influences the vertical polarized brightness temperature at 37 GHz and therefore doesn't need an additional correction.

Brightness temperatures were compared to field soil temperatures at 5 cm depth from test sites located in Oklahoma, and a linear relationship was developed for those two parameters. Representative temperatures for the 6.6 GHz emitting layer (≈ 1.25 cm) were then derived by applying corrections that were based on data from the BARC and Botswana test sites.

The newly derived surface soil temperature algorithm was used on SMMR 37 GHz brightness temperature composites of North America and verified with snow cover maps. Both of these maps showed good comparison, and indicated that the new temperature algorithm can be used in radiative transfer-based retrieval models for soil moisture and vegetation optical depth.

However, due to a lack of soil temperature data bases, the surface soil temperature model is only based on measurements in Oklahoma, Maryland and Botswana. To ensure more accurate global application of the retrieval algorithm and especially in light of prospective new instruments such as SMOS and AMSR satellites one should keep in mind that measurements of soil temperature in the first one or two centimeters at different locations can significantly improve the estimation of the temperature of the emitting layer (T_s). This will subsequently improve the soil moisture and vegetation retrievals from passive microwave signals.

Chapter 5

RETRIEVAL OF SOIL MOISTURE AND VEGETATION OPTICAL DEPTH

This chapter is based on:

De Jeu, R.A.M., and M. Owe (2002). Further Validation of a new Methodology for Surface Moisture and Vegetation Optical Depth Retrieval. *International Journal of Remote Sensing*. In Press.

Owe, M., R.A.M. De Jeu, and J.P. Walker (2001). A Methodology for Surface Soil Moisture and Vegetation Optical Depth Retrieval Using the Microwave Polarization Difference Index. *IEEE Transactions on Geoscience and Remote Sensing*, 39:1643-1654.

5.1 Introduction

Research emphasis in soil moisture retrieval from microwave signals has changed from active to passive as a result of up-scaling problems in the active microwave region. The techniques developed for active microwave retrievals are well suited for small scale (≈ 10 ha), but interpretations face problems at larger scales because of the lack of information about the influence of the topography and vegetation on the return signal (Walker et al., 2000).

Soil moisture information at larger scales has been identified as a parameter of significant potential for improving the accuracy of large-scale land surface atmosphere interaction models (Shukla and Mintz, 1982; Dirmeyer et al., 2000; Owe et al., 1999). Soil moisture is an important link between the exchange of water and energy at the soil-atmosphere interface (Gouweleeuw, 2000). For example, it has been shown that numerical forecasting of precipitation extremes of the United States are strongly affected by soil moisture fields (Entekhabi et al., 1999).

Numerous studies have successfully demonstrated that passive microwave remote sensing has great potential for monitoring soil moisture at larger scales (Schmugge et al., 1986; Jackson and O'Neill, 1990a; Owe et al., 1992; Van de Griend and Owe, 1994a). The techniques developed in these studies provide spatially averaged hydro-

logical data, which is ideal for environmental modelling and monitoring. Such spatially averaged area sets are logistically and economically difficult to obtain through traditional in situ measurement techniques.

Microwave remote sensing techniques are based on radiative transfer theory that require the surface description and especially vegetation optical depth to account for vegetated areas.

Traditional methodologies have attempted to relate remotely sensed estimates of soil moisture to observed ground data, and then solve for the optical depth as a residual. These approaches are not ideal because of poor ground-based data sets, and the inability to quantify spatially representative estimates of surface soil moisture and vegetation biophysical properties at satellite scales.

The methodology described in this chapter is somewhat unique, in that it solves simultaneously for surface moisture and vegetation optical depth, without the use of observations of surface moisture or biophysical parameters. The technique only uses the horizontal and vertical polarization brightness temperatures of one frequency and a surface temperature algorithm based on the vertical polarized 37 GHz signal.

The approach is based on a radiative transfer model, including a newly developed surface temperature algorithm and a vegetation optical depth retrieval technique. It is tested with 6.6 GHz Scanning Multichannel Microwave Radiometer (SMMR) data over footprint-sized test sites in Illinois (USA), Iowa (USA), Turkmenistan, and Mongolia.

Results are compared with soil moisture field observations, precipitation data, and satellite-derived vegetation index data.

5.2 Modelling Approach

The methodology presented here solves for the soil moisture and vegetation optical depth simultaneously, using the simple radiative transfer equation, Equation 2.5, and the horizontal and vertical brightness temperature at 6.6 GHz.

A nominal satellite footprint size of 150 km is assumed. Even though pixels are registered to a $\frac{1}{4}$ degree grid, all retrieval calculations, including ancillary data, are based on the assumed footprint size. A uniform footprint, with respect to average soil and canopy temperatures and vegetation biophysical characteristics is assumed. Surface moisture and vegetation optical depth are subsequently extracted as average footprint values.

Since there are still many more variables than can be solved for effectively by the radiative transfer relationships, some parameters will have to be estimated and/or solved for independently.

As stated earlier (See Section 2.6), information on the scattering albedo is somewhat scarce. While most reported values have been estimated primarily as residual calculations using theoretical approaches with radiative transfer models, limited information exists on validation efforts from actual field measurements. Based on reported scattering albedo values and the effect of the scattering albedo on the observed brightness temperature that was illustrated in Figure 2.6, an average value of 0.06 is used.

It was also assumed that surface roughness would have a minimum effect on the

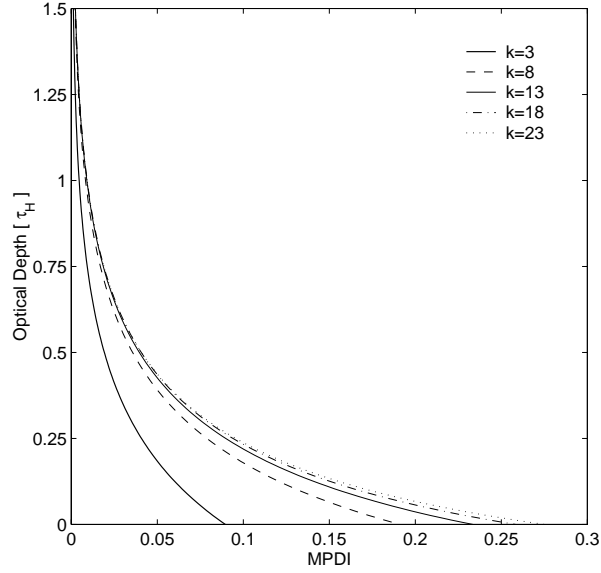


Figure 5.1: The theoretical relationship between MPDI and the vegetation optical depth for a range of soil dielectric constants ($h = 0$, $\omega = 0.06$, and $u = 50.3^\circ$). Typical soil moisture values of $0 \text{ m}^3 \text{ m}^{-3}$, $0.18 \text{ m}^3 \text{ m}^{-3}$, $0.26 \text{ m}^3 \text{ m}^{-3}$, $0.34 \text{ m}^3 \text{ m}^{-3}$, and $0.41 \text{ m}^3 \text{ m}^{-3}$ would correspond to dielectric constants of $k = 3, 8, 13, 18,$ and 23 .

surface moisture calculations over the test areas, and was subsequently set to 0. Furthermore, we didn't account for spatial distribution of temperature within the canopy and assume that the soil and vegetation have the same temperature, $T_s = T_c$ (See equation 2.5), and the mean surface temperature (T_s) of the SMMR footprint was estimated with Equation 4.6. However, T_s may be provided from other sources as well.

The model now has two remaining parameters; the optical depth that represents the vegetation density and directly affects the canopy transmissivity and the soil moisture that affects the the soil emissivity. Solving for these two variables, requires a more unique approach, and is described below. Brightness temperature measured from space contains information on both the canopy and soil surface emissions and their respective physical temperatures (Equation 2.1). Polarization ratios, such as the Microwave Polarization Difference Index (MPDI), are frequently used to remove the dependence of the temperature of the emitting layer on T_b , resulting in a parameter that is quantitatively related to the dielectric properties of all the emitting surface(s). At the 37 GHz frequency, the MPDI is mainly a function of the overlying vegetation, and consequently is a good indicator of the canopy density (Becker and Choudhury, 1988). At a frequency of 6.6 GHz, the MPDI will not only contain information on the canopy, namely the optical depth, but will also contain significantly more information on the soil emission and consequently the soil dielectric properties.

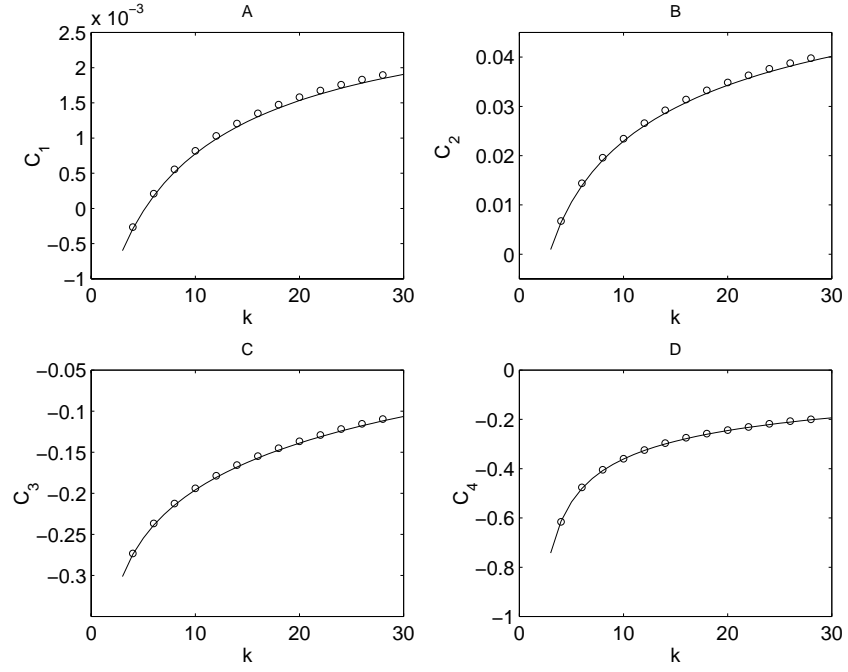


Figure 5.2: A graphical presentation of the relationship between the absolute value of the dielectric constant of the soil (k) and the fitting parameters C_1 , C_2 , C_3 and C_4 .

j	1	2	3	4
$M_{j,1}$	$1.3232 \cdot 10^{-12}$	$5.0225 \cdot 10^{-11}$	$3.0617 \cdot 10^{-10}$	$2.5074 \cdot 10^{-9}$
$M_{j,2}$	$-1.7719 \cdot 10^{-10}$	$-6.5270 \cdot 10^{-9}$	$-3.9492 \cdot 10^{-8}$	$-3.2123 \cdot 10^{-7}$
$M_{j,3}$	$1.0020 \cdot 10^{-8}$	$3.5430 \cdot 10^{-7}$	$2.1215 \cdot 10^{-6}$	$1.7088 \cdot 10^{-5}$
$M_{j,4}$	$-3.1332 \cdot 10^{-7}$	$-1.0452 \cdot 10^{-5}$	$-6.1648 \cdot 10^{-5}$	$-4.8891 \cdot 10^{-4}$
$M_{j,5}$	$5.9980 \cdot 10^{-6}$	$1.8329 \cdot 10^{-4}$	$1.0560 \cdot 10^{-3}$	$8.1506 \cdot 10^{-3}$
$M_{j,6}$	$-7.4764 \cdot 10^{-5}$	$-1.9876 \cdot 10^{-3}$	$-1.1011 \cdot 10^{-2}$	$-8.0281 \cdot 10^{-2}$
$M_{j,7}$	$6.6256 \cdot 10^{-4}$	$1.4150 \cdot 10^{-2}$	$7.3781 \cdot 10^{-2}$	$4.5635 \cdot 10^{-1}$
$M_{j,8}$	$-2.0330 \cdot 10^{-3}$	$-2.7467 \cdot 10^{-2}$	$-4.4594 \cdot 10^{-1}$	-1.5691

Table 5.1: Polynomial parameters that describe the relation between the absolute value of the dielectric constant of the soil (k) and the fitting parameters C_1, C_2, C_3 and C_4 (See Equation 5.3).

The MPDI is defined as

$$MPDI = \frac{T_{b(V)} - T_{b(H)}}{T_{b(V)} + T_{b(H)}} \quad (5.1)$$

The theoretical relationship between the MPDI and the vegetation optical depth as

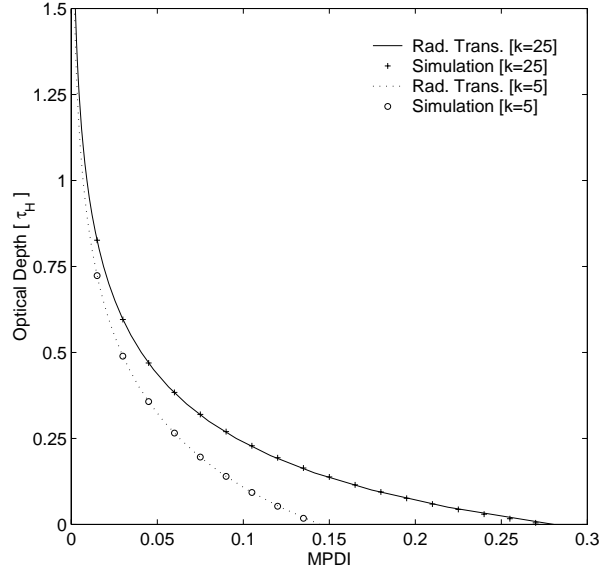


Figure 5.3: Verification comparing the MPDI-optical depth relationship derived from the radiative transfer equation to calculation from simulated data ($h = 0$, $\omega = 0.06$, and $u = 50.3^\circ$).

derived from the radiative transfer equation (Equation 2.5), is illustrated in Figure 5.1.

This relationship was derived by running numerous simulations of $T_{b(V)}$ and $T_{b(H)}$ for different dielectric constants and optical depth. As one notices, however, the relationship between the optical depth and MPDI exhibits a strong dependence on the surface moisture, and is defined by a family of curves according to the surface moisture content. Instead of using soil moisture, however, the absolute value of the soil dielectric constant is used in order to eliminate the influence of soil physical properties. These curves may be defined by fitting a polynomial to the simulations, according to

$$\tau = C_1 \ln(MPDI)^3 + C_2 \ln(MPDI)^2 + C_3 \ln(MPDI) + C_4 \quad (5.2)$$

where the parameters C_1 , C_2 , C_3 and C_4 are a function of k , and can be defined by the relationship

$$C_j = M_{j,1}k^N + M_{j,2}k^{(N-1)} + \dots M_{j,N}k + M_{j,(N+1)} \quad (5.3)$$

Where N is the degree of the polynomial, M refers to the polynomial coefficients (See Table 5.1 and Figure 5.2) and the subscript j refers to the term number. Verification of the above relationships is illustrated in Figure 5.3. The theoretical optical depth, as derived by solving the radiative transfer equation, is plotted together with the model simulation results for wet and dry soil moisture conditions. Agreements

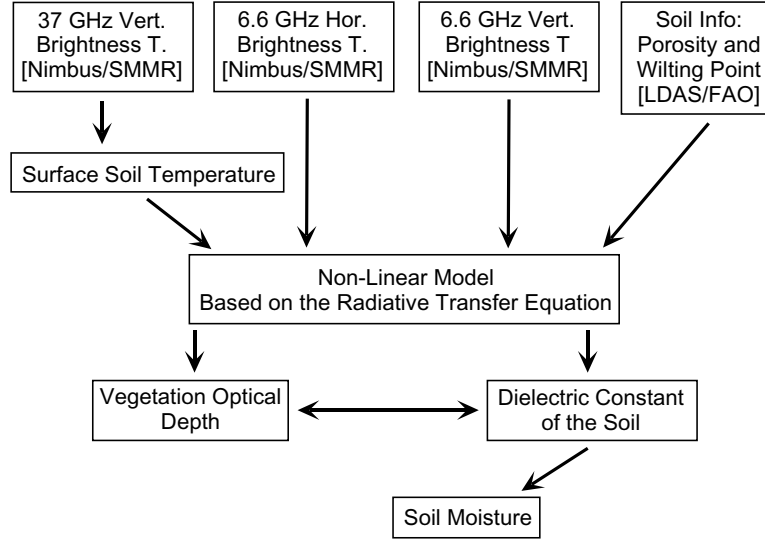


Figure 5.4: A simplified diagram of the soil moisture retrieval methodology

between the two solutions is good.

By substituting Equation 5.2 into Equation 2.6 and 2.5, the optical depth is eliminated and the vegetation parameter in the radiative transfer model is now expressed as a function of MPDI and the soil dielectric constant. The remaining term in the radiative transfer equation (Equation 2.5) is the soil emissivity, $e_{r(l)}$. As H polarization has the greatest sensitivity to soil moisture we solve for $e_{r(l)}$ using $T_{b(H)}$. The emissivity of the soil is calculated from the Fresnel equations (Equation 2.2 and 2.3), where the only unknown is the dielectric constant of the soil. We now have both the vegetation optical depth and the soil emissivity defined in terms of soil dielectric constant. Next, the model uses a non-linear iterative procedure to solve the radiative transfer equation (Equation 2.5) in a forward approach, by optimizing on the dielectric constant.

Once convergence of the calculated and observed brightness temperatures is achieved, the model uses information on soil physical properties, such as particle size distribution, porosity, and wilting point (See section 3.2.2), together with the Wang-Schmugge dielectric model (Wang and Schmugge, 1980) to solve for the surface soil moisture.

In Figure 5.4 the soil moisture retrieval technique is presented in a simplified diagram.

5.3 Results

The methodology outlined above for retrieving of both surface soil moisture and vegetation optical depth has been applied to the entire historical data set of SMMR

brightness temperatures for the previously described locations; Turkmenistan, Mongolia, Iowa and Illinois. These areas were selected because of the availability of long term soil moisture data that can be used for validation purposes.

While not necessarily the most optimum data set for microwave validation, these sets are one of the few data sets in the world, that cover such a large area for such a lengthy period.

Topographic and land use maps were used to select pixel-sized test sites that were relatively flat and homogeneous with respect to land cover. Time series of satellite derived soil moisture are compared to observational soil moisture values from sampling stations within the footprints.

Before looking at these graphs, one must keep in mind several important differences when comparing the satellite-derived surface moisture with the ground observations.

- **Differences in spatial resolution**

The SMMR-derived surface moisture is an average value integrated over the entire footprint, whereas the observational data are point measurements.

- **Differences in vertical resolution**

the observational data are an average soil moisture within the top 10 cm profile, while the SMMR retrievals reflect only the moisture content of the microwave thermal sampling depth, which is at most only about 1 to 2 cm.

- **Differences in acquisition times**

Ground and satellite observations rarely occur on the same day.

- **Inter-observation periods**

While the SMMR observations are displayed with connecting lines, it is done so only to help in observing general trends in the time series. It is important to realize that significant changes in surface moisture may have occurred during the periods between observations, however, these changes may have gone totally undetected by both the satellite and the ground observations.

In Illinois two 150 km test sites were selected for validation (See Figure 3.1 B), with each site containing 3 observation stations. The soil moisture field data is reported as average volumetric moisture content in the top 10 cm profile.

The Iowa location (See Figure 3.1 B) contained two research catchments with three soil moisture measuring stations in each. Measurements for this location represented the average moisture for the top 7.5 cm soil layer. The six bi-monthly point measurements were averaged, providing perhaps the most spatially representative soil moisture values of all the test sites.

A one year time series of SMMR-derived surface moisture along with the observed soil moisture from these three U.S. test sites are given in Figure 5.5. Daily precipitation is also included in the time series to assist in understanding the observed changes in soil moisture.

The Mongolia and Turkmenistan locations could be characterized by only one soil moisture measuring stations each. Both the Mongolian and the Turkmenistan sites (See Figure 3.1 D) are characterized as semi-arid areas.

The Mongolian site is located in the southern part of the Gobi desert and the Turkmenistan site in the southern part of the Kara Kum Desert. Compared to the U.S. test sites, the satellite data is able to clearly differentiate between the dry and wet locations.

All time series of satellite-derived soil moisture illustrate discernable seasonal patterns, although correspondence with the ground observations is not always perfect (See Figure 5.5).

Not every SMMR brightness temperature measurement gave soil moisture and vegetation optical depth estimates because sometimes the non linear model did not converge. In addition, if the surface temperature algorithm generated values below the freezing point the measuring points were eliminated.

Time series of the retrieved optical depths for the same test sites were given in Figure 5.6. Fifteen day NDVI composite data are averaged for the U.S. SMMR footprints (monthly for the Eurasian), and are included for comparison.

A distinct annual course is observed in the optical depth time series, and coincides well with the NDVI at all sites.

The optical depth, however, is seen to be much more variable in time than the NDVI. This is due to the inherent characteristics of the NDVI compositing procedure, where only one value is selected during the composite window to represent the entire composite period. The inability to quantify the vegetation biomass at shorter (*i.e.* daily) time scales is often a drawback of the NDVI. This may be rather significant in arid and semi-arid regions, where greening and senescing of the vegetation canopy (especially grasses) can occur over very short time periods in response to localized and individual precipitation events. The microwave optical depth may actually be a better indicator of green biomass and vegetation dynamics at shorter time scales.

However, it is also important to understand that the NDVI and the microwave optical depth respond to entirely different vegetation properties.

The NDVI is defined as the normalized difference between the reflectance in the visible (red) that represents the absorption band of chlorophyll and the near infrared band that represents a maximum of vegetation reflectance related to the mesophyll structure. The NDVI strongly depends on optical properties of vegetation and is mainly sensitive to leaf water and chlorophyll content (P. Guillevic, Pers. Comm.). The microwave optical depth, on the other hand, responds primarily to the vegetation water content, as a function of the vegetation dielectric properties.

The day-time and night-time soil moisture and vegetation optical depth illustrate values that fall along the same trend in both the moist and dry areas, indicating that the temperature of the emitting layer is reliable and consistent in its estimation.

Even more important, the temperature algorithm can be applied to both the day-time and night-time data, resulting in a significant enhancement of the soil moisture and vegetation optical depth data set.

5.4 Summary and Conclusions

A methodology is presented, that retrieves pixel average surface soil moisture and vegetation optical depth from dual polarized microwave brightness temperature ob-

servations, and has been applied to the 6.6 GHz SMMR data.

The radiative transfer-based approach does not use ground observations of soil moisture, canopy measurement data, or other regional/geophysical data as calibration parameters, and is totally independent of frequency.

However, some assumptions regarding the different elements of the radiative transfer equation are made, in order to reduce the number of variables.

It was assumed that the soil temperature (T_s) was equal to the canopy temperature (T_c). A separate algorithm to estimate T_c would improve the model, especially for the day-time data under sparse canopies where you have the highest difference between T_c and T_s . However, such an algorithm is currently not available and remains a topic for future research.

The model assumes a constant value for the single scattering albedo, based on a series of previous studies, and derives surface temperature from high frequency (37 GHz) vertically polarized brightness temperature data.

A soil roughness parameter was not included during this analysis, however, improvements resulting from the inclusion of a roughness parameter based on land use or topographic data, especially in mountainous or other extreme terrain will also be investigated in the near future.

Days with snow cover or when surface temperatures were below zero were eliminated from the analysis.

A non-linear iterative approach is used to solve for the surface moisture and vegetation optical depth, both of which are derived from the soil dielectric constant.

The model was applied to several sites with observations of surface moisture, located in the U.S., Mongolia and Turkmenistan.

Time series of the satellite-derived surface moisture compared well with the available ground observations and precipitation data.

The vegetation optical depth showed similar seasonal patterns as the NDVI.

In addition, the day-time and night-time vegetation optical depth and soil moisture are in agreement, which is an extra indication of the reliability of the surface soil temperature model, as described in Chapter 4.

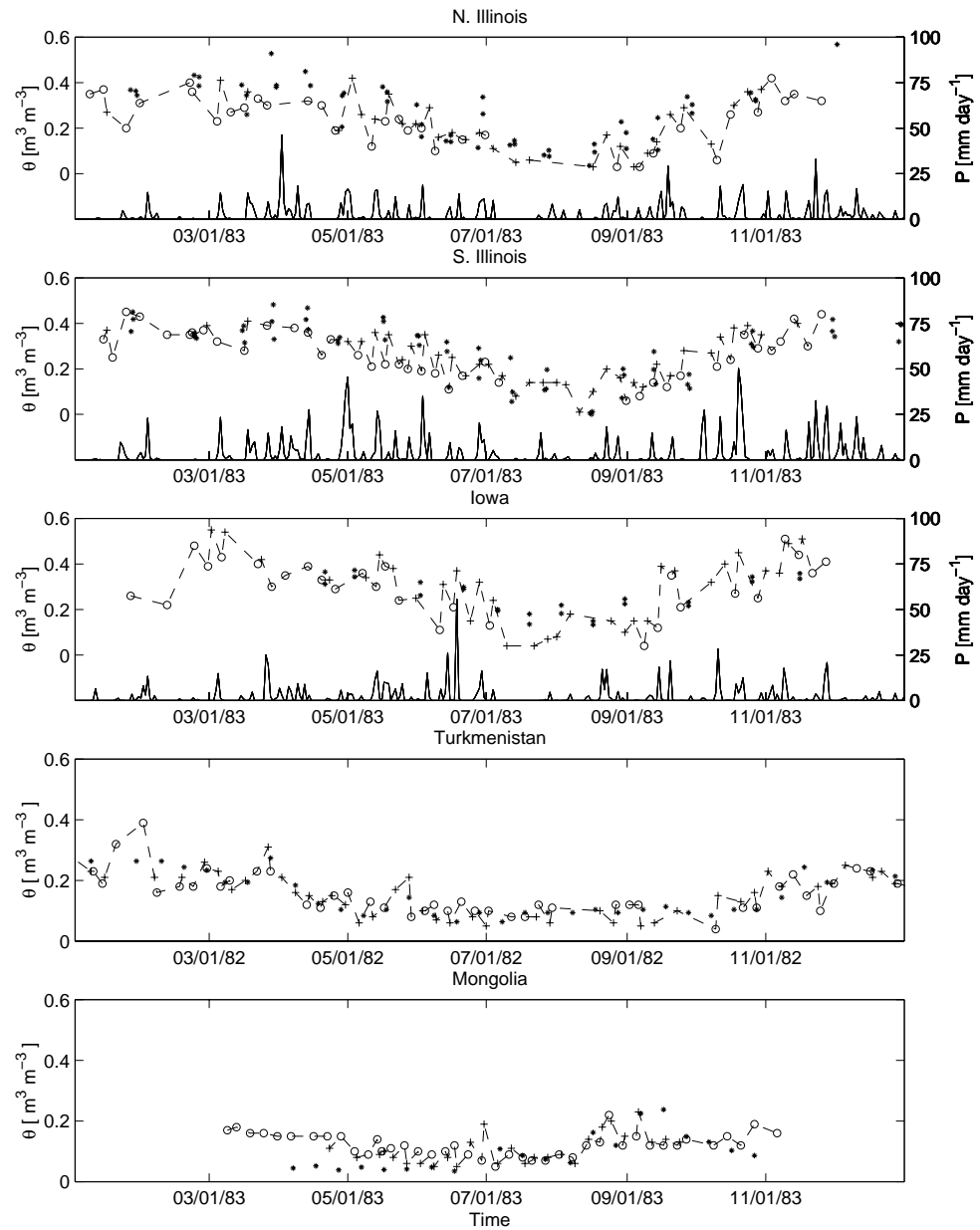


Figure 5.5: Time series of satellite derived day-time (o) and night-time (+) soil moisture and ground observations (*) for the test sites. For comparison the precipitation is included for the American sites.

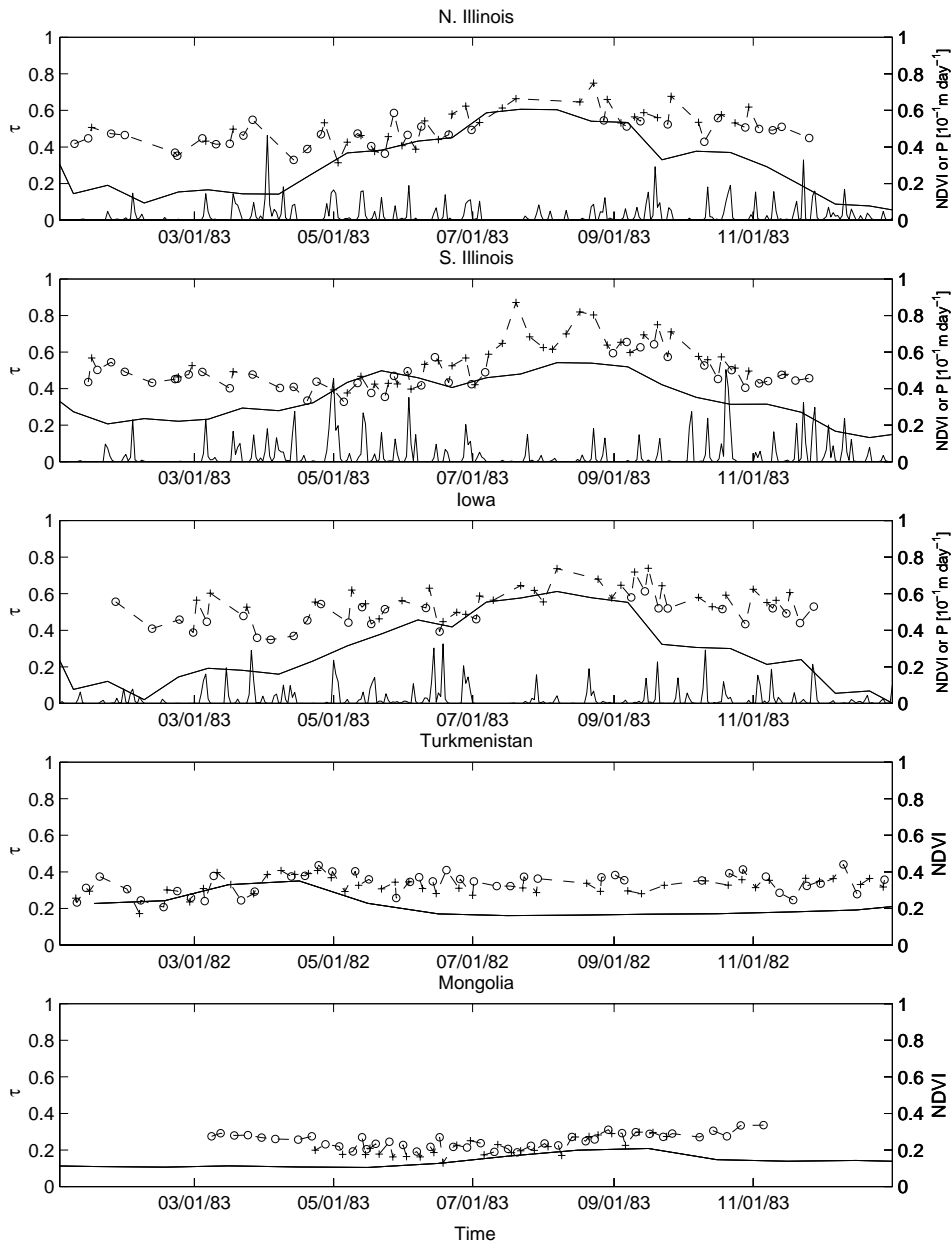


Figure 5.6: Time series of satellite derived day-time (o) and night-time (+) vegetation optical depth and NDVI (-) for the test sites. For comparison the precipitation is included for the American sites.

Chapter 6

LIMITATIONS OF THE LAND SURFACE PARAMETER RETRIEVALS

This chapter is based on:

De Jeu, R.A.M., and M. Owe (2002). Limitations of land surface parameters derived from passive microwave remote sensing. *International Journal of Remote Sensing*. Submitted.

6.1 Introduction

Ideally, results of the land surface parameter models are validated by comparison with time series of measured land surface parameters (Gouweleeuw, 2000).

In this study the passive microwave soil moisture retrieval model was validated with time series of measured soil moisture. The vegetation optical depth was verified with NDVI data (Section 5.3) and the surface soil temperature with snow cover data and validated with the soil moisture retrieval model itself (Section 4.4).

However, as already mentioned in Section 5.3, the comparison of the retrieved parameters with field data or data with a different spatial and/or temporal resolution is often difficult and may introduce wrong interpretations.

To obtain a better understanding of the potential and limitations of the land surface retrieval models, an error propagation analysis was performed. This analysis is conducted to evaluate the potential error in the retrieved land surface parameters by looking at the accuracy of the input parameters.

The accuracy of the input parameters is sometimes difficult to estimate with any degree of precision because of the limitations of available measurement techniques and the associated spatial and temporal variability. Some input parameters, like the measured brightness temperatures have a well-defined value for their accuracy, while others need a "best guess" approach.

Although it is not possible to compare the satellite derived soil moisture and vegetation optical depth with "true" values, due to the lack of existing data sets for comparison and extreme difficulty in measuring spatially averaged soil moisture and vegetation optical depth, the error propagation analysis is still an appropriate tech-

nique, because it illustrates the sensitivity of the input parameters.

This chapter begins with the theory of the error propagation analysis, followed by its application to the five test sites.

The second part of this chapter deals with the masking routine. At some points the land surface models cannot be used because the physical limitations of microwave technology are exceeded. In this chapter applications are described that can detect these miscalculations. These model limitations are discussed in detail and this chapter concludes with a general discussion about the restrictions of the models.

6.2 Error Propagation Analysis

6.2.1 Theory

The description of an error propagation analysis can be found in most general statistical textbooks and an adapted version for the retrieved land surface parameters is given below. The accuracy of the land surface parameters may be calculated by using the errors of the input parameters. This can be done with a covariance matrix:

$$\Sigma y = U \Sigma x U' \quad (6.1)$$

where

$$y = \begin{bmatrix} T_s \\ \tau \\ \theta \end{bmatrix}, \quad \Sigma y = \begin{bmatrix} \sigma_{T_s}^2 & \sigma_{T_s \tau} & \sigma_{T_s \theta} \\ \sigma_{T_s \tau} & \sigma_{\tau}^2 & \sigma_{\tau \theta} \\ \sigma_{T_s \theta} & \sigma_{\tau \theta} & \sigma_{\theta}^2 \end{bmatrix}, \quad x = \begin{bmatrix} T_{b \ 6.6 [H]} \\ T_{b \ 6.6 [V]} \\ T_{b \ 37 [V]} \\ P \\ WP \end{bmatrix},$$

$$\Sigma x = \begin{bmatrix} \sigma_{T_{b \ 6.6 [H]}}^2 & 0 & 0 & 0 & 0 \\ 0 & \sigma_{T_{b \ 6.6 [V]}}^2 & 0 & 0 & 0 \\ 0 & 0 & \sigma_{T_{b \ 37 [V]}}^2 & 0 & 0 \\ 0 & 0 & 0 & \sigma_P^2 & 0 \\ 0 & 0 & 0 & 0 & \sigma_{WP}^2 \end{bmatrix},$$

U is the partial derivative matrix and may be defined as

$$U = \begin{bmatrix} \frac{\partial T_s}{\partial T_{b \ 6.6 [H]}} & \frac{\partial T_s}{\partial T_{b \ 6.6 [V]}} & \frac{\partial T_s}{\partial T_{b \ 37 [V]}} & \frac{\partial T_s}{\partial P} & \frac{\partial T_s}{\partial WP} \\ \frac{\partial \tau}{\partial T_{b \ 6.6 [H]}} & \frac{\partial \tau}{\partial T_{b \ 6.6 [V]}} & \frac{\partial \tau}{\partial T_{b \ 37 [V]}} & \frac{\partial \tau}{\partial P} & \frac{\partial \tau}{\partial WP} \\ \frac{\partial \theta}{\partial T_{b \ 6.6 [H]}} & \frac{\partial \theta}{\partial T_{b \ 6.6 [V]}} & \frac{\partial \theta}{\partial T_{b \ 37 [V]}} & \frac{\partial \theta}{\partial P} & \frac{\partial \theta}{\partial WP} \end{bmatrix}$$

The assumption is made that there is no correlation between the input parameters. Taking into account that the temperature of the emitting layer (T_s) at 6.6 GHz is estimated with only the 37 GHz vertical polarized brightness temperature, Σy may be defined as:

$$\Sigma y = \begin{bmatrix} \left(\frac{\partial T_s}{\partial T_{b\ 37\ [V]}} \sigma_{T_{b\ 37\ [V]}}\right)^2 & \frac{\partial T_s \partial \tau}{\partial T_{b\ 37\ [V]}^2} \sigma_{T_{b\ 37\ [V]}}^2 & \frac{\partial T_s \partial \theta}{\partial T_{b\ 37\ [V]}^2} \sigma_{T_{b\ 37\ [V]}}^2 \\ \\ \frac{\partial T_s \partial \tau}{\partial T_{b\ 37\ [V]}^2} \sigma_{T_{b\ 37\ [V]}}^2 & \left(\frac{\partial \tau}{\partial T_{b\ 6.6\ [H]}} \sigma_{T_{b\ 6.6\ [H]}}\right)^2 + \left(\frac{\partial \tau}{\partial T_{b\ 6.6\ [V]}} \sigma_{T_{b\ 6.6\ [V]}}\right)^2 + \left(\frac{\partial \tau}{\partial T_{b\ 37\ [V]}} \sigma_{T_{b\ 37\ [V]}}\right)^2 + \left(\frac{\partial \tau}{\partial P} \sigma_P\right)^2 + \left(\frac{\partial \tau}{\partial WP} \sigma_{WP}\right)^2 & \frac{\partial \tau \partial \theta}{\partial T_{b\ 6.6\ [H]}^2} \sigma_{T_{b\ 6.6\ [H]}}^2 + \frac{\partial \tau \partial \theta}{\partial T_{b\ 6.6\ [V]}^2} \sigma_{T_{b\ 6.6\ [V]}}^2 + \frac{\partial \tau \partial \theta}{\partial T_{b\ 37\ [V]}^2} \sigma_{T_{b\ 37\ [V]}}^2 + \frac{\partial \tau \partial \theta}{\partial P^2} \sigma_P^2 + \frac{\partial \tau \partial \theta}{\partial WP^2} \sigma_{WP}^2 \\ \\ \frac{\partial T_s \partial \theta}{\partial T_{b\ 37\ [V]}^2} \sigma_{T_{b\ 37\ [V]}}^2 & \frac{\partial \tau \partial \theta}{\partial T_{b\ 6.6\ [H]}^2} \sigma_{T_{b\ 6.6\ [H]}}^2 + \frac{\partial \tau \partial \theta}{\partial T_{b\ 6.6\ [V]}^2} \sigma_{T_{b\ 6.6\ [V]}}^2 + \frac{\partial \tau \partial \theta}{\partial T_{b\ 37\ [V]}^2} \sigma_{T_{b\ 37\ [V]}}^2 + \frac{\partial \tau \partial \theta}{\partial P^2} \sigma_P^2 + \frac{\partial \tau \partial \theta}{\partial WP^2} \sigma_{WP}^2 & \left(\frac{\partial \theta}{\partial T_{b\ 6.6\ [H]}} \sigma_{T_{b\ 6.6\ [H]}}\right)^2 + \left(\frac{\partial \theta}{\partial T_{b\ 6.6\ [V]}} \sigma_{T_{b\ 6.6\ [V]}}\right)^2 + \left(\frac{\partial \theta}{\partial T_{b\ 37\ [V]}} \sigma_{T_{b\ 37\ [V]}}\right)^2 + \left(\frac{\partial \theta}{\partial P} \sigma_P\right)^2 + \left(\frac{\partial \theta}{\partial WP} \sigma_{WP}\right)^2 \end{bmatrix}$$

6.2.2 Application to the Test Sites

6.2.2.1 General

The accuracy of the input parameters is partly estimated with a "best guess" approach and partly taken from literature. The standard deviations of the brightness temperatures are taken from the Nimbus/SMMR manual (Gloersen and Barath, 1977) and are 0.7 K and 1.4 K for the 6.6 GHz and the 37 GHz channels, respectively. The standard error of the porosity (P) and wilting point (WP) from the LDAS and FAO data set are unknown and it is very difficult to give reliable estimates of the accuracy of these soil properties. This is due to the complex spatial distribution of the soil properties of the top soil layer. In order to get an idea of the magnitudes of the accuracy, the global range in porosity and wilting point is used to estimate the standard deviation. The accuracy of the porosity is set at $0.02\ \text{m}^3\ \text{m}^{-3}$ and the wilting point at $0.03\ \text{m}^3\ \text{m}^{-3}$.

The error propagation analysis is used to calculate the standard deviations of the land surface parameters for all five test sites for the entire period of record of the SMMR data.

Matrix U from Equation 6.1, is derived by numerical calculation at every time step. At each step there were three simulations for each individual input parameter.

The first simulation estimated the land surface parameters with the given input parameters. The second simulation estimated the land surface parameters by using a positively changed value of the input parameter by only one percent of its original value. The third simulation estimated the land surface parameters with a lower value

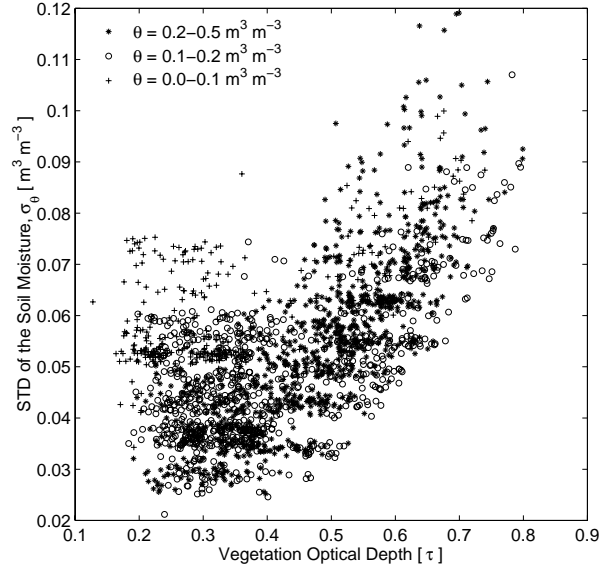


Figure 6.1: The standard deviation of the soil moisture as related the vegetation optical depth. Note the different relations for different moisture regimes

of the input parameter by subtracting one percent of the value from the original input parameter. The latter two simulations were averaged to estimate the change of the land surface parameters compared to change of the individual input parameters. Matrix U (See Equation 6.1) can be derived by doing these three simulations for every input parameter individually. The standard deviation of the land surface parameters can now be derived.

6.2.2.2 Standard deviations of the land surface parameters

The standard deviation of the temperature of the emitting layer at 6.6 GHz for the five test sites is rather constant and reaches a value of 1.2 K.

The standard deviations of the soil moisture and the vegetation optical depth are not constant and require further explanation.

For all the 5 test sites together, the standard deviations of the soil moisture varied between $0.02 \text{ m}^3 \text{ m}^{-3}$ and $0.12 \text{ m}^3 \text{ m}^{-3}$ with an average value of $0.05 \pm 0.02 \text{ m}^3 \text{ m}^{-3}$. The standard deviation of the soil moisture is related to the vegetation optical depth according to the relationship illustrated in Figure 6.1. This graph clearly shows the expected increase in uncertainty of soil moisture when the vegetation cover increases in density. As already explained in Section 2.6, the relative proportion of soil moisture information within the passive microwave signal decreases when the biomass increases, resulting in a less accurate soil moisture estimate. The same Figure also shows high standard deviation values for low soil moisture values. For example, for

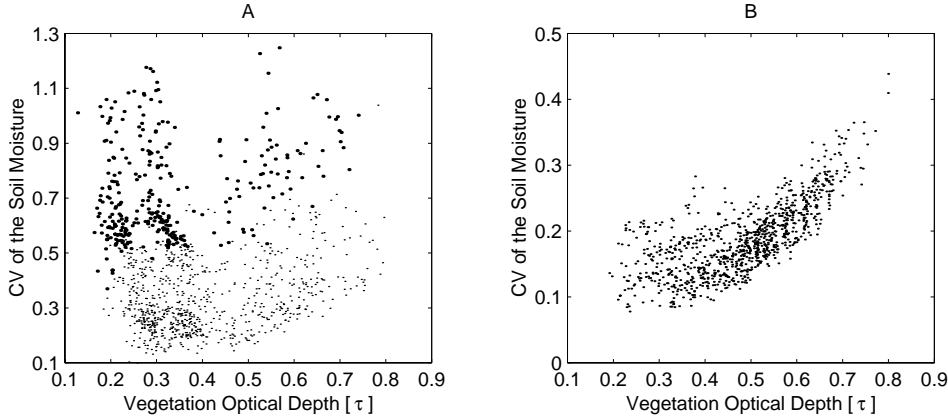


Figure 6.2: The Coefficient of Variation (CV) of the soil moisture as related to the vegetation optical depth. The relationship is separated in two different soil moisture classes, where (A) represents the dry soils with soil moisture values below $0.2 \text{ m}^3 \text{ m}^{-3}$ and (B) represents the wet soils with soil moisture values between 0.2 and $0.5 \text{ m}^3 \text{ m}^{-3}$. In Figure A the thick dots represent dry soils with soil moisture values below $0.1 \text{ m}^3 \text{ m}^{-3}$ and the thin dots soil moisture values between 0.1 and $0.2 \text{ m}^3 \text{ m}^{-3}$.

the soil moisture range between 0.0 and $0.1 \text{ m}^3 \text{ m}^{-3}$ the standard deviation values are between 0.05 and $0.07 \text{ m}^3 \text{ m}^{-3}$. These values are due to the low sensitivity of the dielectric constant of the soil in response to soil moisture in the range between 0 and $0.1 \text{ m}^3 \text{ m}^{-3}$ (See Figure 2.2). In this range a small change in the soil dielectric will give a big change in soil moisture.

The standard deviation of soil moisture as a function of the vegetation optical depth can also be interpreted in terms of mean soil moisture. Often, higher standard deviations are observed primarily when the mean is also high. In such cases, however, the relative standard deviation actually remains fairly constant. The coefficient of variation ($CV = \frac{std}{mean}$) is frequently used to investigate such relationships (Figure 6.2). The CV of soil moisture is seen to be highly variable throughout the entire range of vegetation optical depths. While this relationship appears somewhat random at first glance, a distinct pattern is observed when the data are grouped by range of mean soil moisture. For very dry soils ($\theta < 0.1 \text{ m}^3 \text{ m}^{-3}$), the variability of soil moisture is extremely high (Figure 6.2 A). At the intermediate soil moisture range ($\theta = 0.1 - 0.2 \text{ m}^3$), the variability, while still high, is significantly reduced (Figure 6.2 A). For wetter soils ($\theta > 0.2 \text{ m}^3 \text{ m}^{-3}$), a more typical pattern for the CV emerges, and the variability in soil moisture becomes even lower (Figure 6.2 B).

This phenomenon can actually be explained theoretically. The dynamic range of the observed emissivity relative to the optical depth, is very low for dry soils. This range in emissivity increases significantly as the soil moisture increases (See Figure 2.5). Soil moisture and vegetation have opposite effects on the emissivity. This paradox may be explained in more simplified terms.

The observed brightness temperature and resulting emissivity for a dry soil is high.

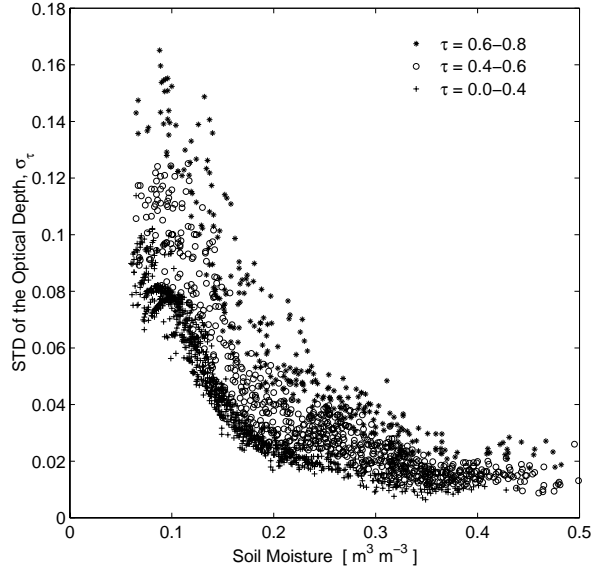


Figure 6.3: The standard deviation of the vegetation optical depth as related to the soil moisture. Note the different relations for different vegetation types.

In this situation, a vegetation canopy will actually work in tandem, and increase the brightness temperature and emissivity even more. As the soil moisture increases, it appears too cool, and the range in emissivity relative to the optical depth also increases.

The standard deviation of the optical depth, relative to soil moisture, is inversely related, but exhibits a more distinct pattern overall (Figure 6.3). When the data are grouped by levels of mean optical depth, it is clearly seen that the magnitude of the standard deviation, in an absolute sense, at a given soil moisture, is in direct proportion to the mean. However, when we look at the coefficient of variation of the optical depth, we find that the highest CVs correspond to lower mean optical CVs correspond to lower mean optical depth values, but only under relatively dry moisture conditions ($\theta \leq 0.15 \text{ m}^3 \text{ m}^{-3}$) (Figure 6.4 A). In other words, the standard deviation of the optical depth, relative to the mean, actually decreases as the optical depth increases during dry conditions (Figure 6.4 A). As the soil moisture increases, the CV of the optical depth decreases more or less uniformly, regardless of vegetation cover (Figure 6.4 A and B).

Again, this explanation has a strong theoretical basis (See Figure 2.5). At low moisture conditions, the soil emission is high and the additional contribution to the overall observed emissivity from low levels of vegetation is also low. Consequently, it is more difficult to partition the relatively small contribution from the vegetation. As soil moisture increases, the soil cools and the emission becomes lower, the relative contribution of the vegetation to the overall observed emissivity becomes more significant.

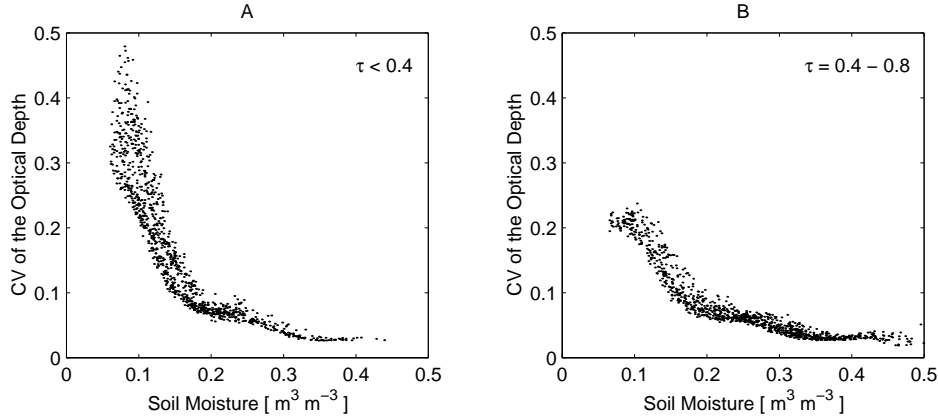


Figure 6.4: The coefficient of variation of the vegetation optical depth as related to the soil moisture. The relationship is separated in two different vegetation classes, where (A) represents sparse vegetation with optical depth values below 0.4, and (B) represents dense vegetation with optical depth values τ between 0.4 and 0.8.

6.2.2.3 Sensitivity of the individual input parameters

To understand the sensitivity of the individual input parameters on the model output, the contribution of these parameters in the total standard deviation was calculated. For every test site the standard deviation of soil moisture and vegetation optical depth was estimated using the error propagation analysis, and within this analysis, the contribution of every single input parameter was estimated. The resulting values are summarized in Table 6.1. In this Table both the night-time and day-time sets were combined, because the error propagation analysis did not show significant differences between those two sets. The current table shows that the accuracy of the soil moisture for the wet American test sites is mainly dominated by the accuracy of the horizontal polarized brightness temperature at 6.6 GHz ($T_{b6.6[H]}$). For the dry Eurasian sites the vertical polarized brightness temperature at 37 GHz ($T_{b37[V]}$) becomes more important. The standard deviation of the vegetation optical depth is mainly determined by the accuracy of both the horizontal and vertical polarized brightness temperatures at 6.6 GHz for the wet American test sites. For the dry Eurasian sites the vertical brightness temperature at 6.6 GHz becomes less important and the accuracy of both the horizontal 6.6 GHz and the vertical 37 GHz give a main contribution to the total standard deviation of the vegetation optical depth. In general, this means that if engineers can increase the accuracy of the microwave sensors, the accuracy of the soil moisture and vegetation optical depth retrievals increases significantly. Also, in the dry areas, the accuracy of both parameters is mainly related to the vertical 37 GHz signal and therefore related to the temperature of the emitting layer (T_s). This means that a better surface temperature algorithm will certainly improve the accuracy of these two land surface parameters in dry areas. The influence of soil physical properties on the retrieval of soil moisture and vege-

tation optical depth is limited. In the entire error propagation analysis the surface roughness (h) and the single scattering albedo (ω) were not used as input parameters, because for the retrieval algorithm these parameters were fixed (*i.e.* $h = 0$, and $\omega = 0.06$). In order to check the influence of these parameters on the model, both the roughness and albedo were put in the error propagation analysis and the percentages on the total standard deviations were estimated. For a single scattering albedo standard deviation of 0.003, the influence of the albedo on the total standard deviation of soil moisture was 7 % for the American sites and about 2 % for the Eurasian sites. The influence of the single scattering albedo on the total standard deviation of the vegetation optical depth was limited and approximately 1.5 % for all the test sites. With an assumed standard deviation of 0.02, the roughness influence on the total standard deviations of soil moisture and vegetation optical depth was negligible.

6.3 Masking Routine

6.3.1 General

A data mask was developed in order to provide an improved and more realistic map of reliable data points. It eliminates those data grid cells where data values are either meaningless, such as areas with frozen surfaces or snow cover, areas with excessive vegetation, or where errors were known to be so excessive, that their reliability is in serious doubt. The masking process consists of several distinct routines which are specific to the various surfaces and their respective errors. These routines are executed as part of the model either before, during, or after the retrieval algorithm.

6.3.2 Snow and Frozen Soil

The dielectric constants of water, ice and snow are so drastically different that these three materials are easy to distinguish with the passive microwave signals. Land surface retrieval models are based on the dielectric constant of water and not on snow or ice, so when the soil temperature is below freezing or when there is snow on the ground these models cease to provide useful information. However, during snow free freezing conditions it seems possible to obtain reliable surface soil temperatures from the 37 GHz vertical polarized brightness temperatures. Efforts to test this hypothesis are currently in progress. Pixels with snow were detected with the difference algorithm of Chang et al. (1987) and frozen soils were detected with the newly developed surface soil temperature algorithm, as described in Chapter 4. These pixels were excluded for further calculation.

6.3.3 Vegetation

Soil emission is attenuated by the canopy and tends to saturate the microwave signal with increasing optical depth, resulting in a decreased sensor sensitivity to soil moisture variations (See Section 2.6). Figure 6.1 shows this effect explicitly, with high soil moisture deviations for high optical depths.

Test Site	Par.	Mean	STD	CV	Contribution in % of the input parameters on the total STD				
					$T_{b\ 6.6\ [H]}$	$T_{b\ 6.6\ [V]}$	$T_{b\ 37\ [V]}$	P	WP
					$\sigma=0.7$	$\sigma=0.7$	$\sigma=1.4$	$\sigma=0.02$	$\sigma=0.03$
N. Illinois	θ	0.24	0.06	0.23	59.2	15.8	25.0	0	0
	τ	0.52	0.04	0.08	57.5	35.6	5.8	0	1.1
S. Illinois	θ	0.26	0.06	0.22	58.1	16.2	25.7	0	0
	τ	0.53	0.04	0.07	56.9	36.9	5.2	0	1.0
Iowa	θ	0.27	0.06	0.22	59.1	15.8	25.1	0	0
	τ	0.54	0.04	0.08	57.3	36.5	5.4	0	0.8
Turkmenistan	θ	0.15	0.05	0.31	31.5	7.8	60.7	0	0
	τ	0.33	0.05	0.15	39.1	15.3	41.8	0.2	3.6
Mongolia	θ	0.13	0.05	0.37	31.2	6.8	62.0	0	0
	τ	0.25	0.06	0.23	34.8	11.2	49.9	0.3	3.8

Table 6.1: Contribution of the input parameters in the total standard deviations of the soil moisture and vegetation optical depth. Note, the soil moisture values (θ) are in $\text{m}^3 \text{m}^{-3}$.

According to Njoku and Li (1999) the limit to detect soil moisture changes at 6.6 GHz, is achieved when the vegetation cover has a water content (VWC) of 1.5 kg m^{-2} , which corresponds to a vegetation optical depth of about 0.75. In the previous section we saw that in our study areas the soil moisture uncertainty is very high ($CV > 0.8$) when the vegetation optical depth reaches a values of 0.8. So one can say that for areas with a vegetation optical depth beyond 0.8 the vegetation and soil moisture retrieval model isn't reliable anymore and the soil moisture and vegetation optical depth values under these conditions are masked out.

The accuracy of the soil surface temperature retrieval algorithm under different vegetation types is still unknown and work on this part needs to be done in the near future.

6.4 Conclusions

The error propagation analysis reinforced the hypothesis that the standard deviations of retrieved soil moisture are high when the vegetation optical depth is high. The soil emission is attenuated by the vegetation and as the vegetation cover becomes denser the sensitivity of the microwave sensor to retrieve soil information will subsequently decrease.

Low soil moisture values also have high standard deviations. These high deviations were due to the low sensitivity of the dielectric constant of the soil on soil moisture when it is dry.

Optimum results in the detection of accurate soil moisture with the satellite retrieval model can be obtained with high soil moisture values under sparse vegetation.

Compared with wet conditions, the uncertainty of the vegetation optical depth is high at dry conditions. This phenomenon also has a theoretical basis. At low moisture conditions, the soil emission is high and the additional contribution to the overall observed emissivity from low levels of vegetation is also low. As soil moisture increases, the soil cools and the emission becomes lower, the relative contribution of the vegetation of the overall observed emissivity becomes more significant.

Improvement in the accuracy of the passive microwave instruments will significantly contribute to the accuracy of the satellite derived land surface parameters. In addition, a more accurate surface temperature model will enhance the accuracy of both soil moisture and vegetation optical depth, especially in dry areas.

To increase the reliability of the retrieved land surface parameters a masking routine has been applied. At first, the microwave algorithm is unable to retrieve reliable land surface parameters when the soil is frozen or when there is snow on the ground. This is due to the distinct behavior of snow and ice on the dielectric constant. Pixels containing snow and/or ice cover were subsequently excluded prior to initiation of the retrieval algorithm. Second, the microwave sensor loses sensitivity to detect soil moisture variation when the vegetation cover is dense. The retrieved soil moisture and vegetation optical depth values were excluded for further calculation when the vegetation optical depth reaches a value of 0.8, which is an average value for a vegetation cover with a vegetation water content (VWC) of approximately 1.5 kg m^{-2} .

Chapter 7

LAND SURFACE PARAMETERS DERIVED FROM 18 GHz

7.1 Introduction

Soil moisture is an important hydrologic variable in a variety of land surface atmosphere interactions (Lakshmi et al., 1997). It integrates precipitation and evaporation over periods of days to weeks and introduces a significant element of memory in the atmosphere/land system (Jackson et al., 1999).

In addition it has been shown that soil moisture is a very important factor in the study of climate using global circulation models (Walker and Rowntree, 1977; Rowntree and Bolton, 1983; Rind, 1982; Mintz, 1984). Therefore, there is a distinct need for a long term spatially averaged global soil moisture data base.

With the development of the methodology presented here, it is possible to generate such data bases for soil moisture, vegetation optical depth and surface soil temperature. This can be done with the 6.6 GHz and 37 GHz signals from the Nimbus/SMMR satellite which cover the 9 year period between October 1978 through August 1987. To extend this period until the present, other satellites observations are necessary. However, the frequency used for the soil moisture retrieval technique was 6.6 GHz, and such a satellite sensor hasn't been available since the deactivation of SMMR.

Since 1987 the only stable microwave sensor with regular global coverage was the Special Sensor Microwave Imager (SSM/I), an instrument onboard several DMSP satellite platforms. However, the limiting feature of the SSM/I instrument for soil moisture-related studies, is that the frequencies are higher and are significantly affected by vegetation (Jackson, 1997).

In the past, several attempts have been made to utilize these sensors in soil moisture studies with limited success (Choudhury and Golus, 1988; Jackson, 1997; Kerr and Njoku, 1990; Owe et al., 1992).

This chapter will investigate the possibility of using SSM/I observations to generate a long term global land surface parameter data base.

Since the lowest frequency of the SSM/I is 19.4 GHz, the ideal situation would be to generate SSM/I soil moisture retrievals and compare them to 6.6 GHz SMMR re-

trievals for the same time period. This, however, is not possible because the overlap between these two instruments was less than one month, and would not provide a reliable comparison.

Consequently, an alternative method for testing the utility of SSM/I for soil moisture retrieval was developed, whereby SMMR 18 GHz observations were used for comparison with the 6.6 GHz data. The frequency of this signal is similar to the SSM/I signal and has an optimum temporal overlap with the 6.6 GHz.

The first section of this chapter will discuss the model modification for the use of the 18 GHz, and in the following section the results are compared with the 6.6 GHz retrievals. Furthermore, an error propagation analysis is applied to the 18 GHz retrievals, and limitations and future use are also discussed.

7.2 Model Modification

The radiative transfer equation (Equation 2.5) can also be solved quite easily at 18 GHz for soil moisture and canopy optical depth if the emitting layer temperature is known.

For 6.6 GHz, T_s is estimated as the soil temperature at 1.25 cm. A procedure for deriving this parameter is given in Chapter 4. However, in order to solve the radiative transfer equation at 18 GHz, an estimate of T_s at this frequency is necessary.

The thickness of the emitting layer is typically described as approximately "several" tenths of a wavelength (Schmugge, 1983), and for a frequency of 18 GHz ($\lambda = 1.67$ cm), this depth might be estimated at about 0.5 cm. The temperature algorithm which had been developed for the 6.6 GHz data must therefore be modified.

Equation 4.5 gives the relationship between soil temperature at 1.25 cm depth and 5 cm depth, and is derived from field data as previously described (See Section 3.2.3.2 and 3.2.3.3).

Since no soil temperature data at 0.5 cm depth could be located, T_s was estimated by extrapolating measurements at known depths. The relationship between measurements at 0.5 cm and 5 cm depth may now be expressed as

$$T_{s[0.5cm]} = 1.146T_{s[5cm]} - 46.008 \quad (7.1)$$

When combining Equation 7.1 with Equation 4.2, the temperature of the 0.5 cm emitting layer can be defined as

$$T_{s[0.5cm]} = T_s = 0.864T_{b(37GHz[V])} + 48.013 \quad (7.2)$$

Both day-time and night-time soil moisture and vegetation optical depth were calculated for the 5 test sites using the entire period of the Nimbus/SMMR data set.

The same value for the single scattering albedo and surface roughness, as were used with the 6.6 GHz signal, were also used here. These values were respectively 0.06 for the single scattering albedo and 0 for the surface roughness.

For better comparison, the retrieved 18 GHz soil moisture and vegetation optical depth were averaged over the 6.6 GHz footprint, which is approximately 3 by 3 $\frac{1}{4}$ degree pixels at 18 GHz.

The soil input parameters used in the retrieval models were derived from the ISLSCP and FAO soil data set (See section 3.2.2, for detailed description of these sets).

7.3 Results

A one year time series of satellite derived surface moisture and vegetation optical depth as derived from the 18 GHz observations are compared to the 6.6 GHz retrievals and are illustrated in Figures 7.1 and 7.2 for the five test sites.

7.3.1 Vegetation

Vegetation optical depth (Figure 7.2) is shown to exhibit similar trends at both frequencies, although it is seen to be consistently higher at 18 GHz. The shorter wavelength at 18 GHz is not able to penetrate the canopy as readily as the radiation at 6.6 GHz, resulting in higher optical depth values.

This is also observed quite clearly in Figure 7.4, where the optical depth values observed at the two frequencies are plotted together in the same graph. The slope of the regression line is near unity, suggesting a more or less constant offset throughout the range of of observed values.

These results are in agreement with the findings of Kirdiashev et al. (1979) , where it was concluded that optical depth is inversely proportional to the wavelength. Similar results were also found by van de Griend and Owe (1994b), in a comparison of optical depths derived from 6.6 GHz and 37 GHz observations.

7.3.2 Soil Moisture

The retrieved soil moistures also illustrates similar patterns for the two frequencies (Figure 7.1). Additionally, the overall magnitudes are quite similar. However, certain differences are also readily observed.

When the values are plotted together in the same graph (Figure 7.3), it is seen that they are evenly distributed about the 1:1 line when the average soil moisture is above approximately 20 percent.

However, when the average soil moisture falls below 20 percent, it is noticed that the 18 GHz retrievals begin to fall below the 6.6 GHz values. This can be considered quite normal, though, since the emitting depth of the microwave radiation at 18 GHz is much closer to the surface than at 6.6 GHz. As the soil continues to dry, the thinner surface layer defined by the 18 GHz observations will consequently be drier on average.

The scatter in Figure 7.3 is caused by a variety of effects, like differences in the influence of the atmosphere on the 18 GHz and 6.6 GHz signals, differences in penetration depth, and differences in sensitivity to vegetation.

7.3.3 Interrelationships and Errors

The interrelationship between vegetation and soil moisture retrievals was investigated by an error propagation analysis. It is seen that the error in optical depth retrieval is

higher for the 18 GHz (Figure 7.5 compared to the 6.6 GHz (Figure 6.3). While this relationship between the two different sensors is very similar, the errors are somewhat greater.

Similarly, the standard deviation of the soil moisture retrievals increases as the optical depth increases (Compare Figure 7.6 with 6.1). Again, while this relationship is similar to the 6.6 GHz, the errors at 18 GHz are again found to be somewhat higher

7.4 Conclusions and Recommendations

The land surface parameter retrievals from 18 GHz SMMR observations using the newly developed methodology seem to be reliable, and illustrate that the 19.4 GHz SSM/I may be used to extend the SMMR soil moisture dataset. The soil moisture values derived from the 18 GHz signal show the same seasonal trend as the values derived from the 6.6 GHz signal.

The vegetation optical depth is inversely proportional to the wavelength and therefore significantly higher at 18 GHz than at 6.6 GHz.

However it must be remembered, that the higher frequency retrievals will represent a shallower surface layer, and will also adversely influenced by a much thinner vegetation cover.

At a vegetation optical depth of about 0.65 the sensitivity to detect soil moisture is severely reduced and observations become unreliable.

Also, for frequencies higher than 10 GHz the influence of the atmosphere starts to become significant, and an atmosphere correction component in the radiative transfer is necessary to get optimum soil moisture and vegetation optical depth retrievals. It seems that the precipitable water of the atmosphere has a relationship with the horizontal polarized emissivity and can be used to solve the atmospheric component in the radiative transfer (Choudhury et al., 1992).

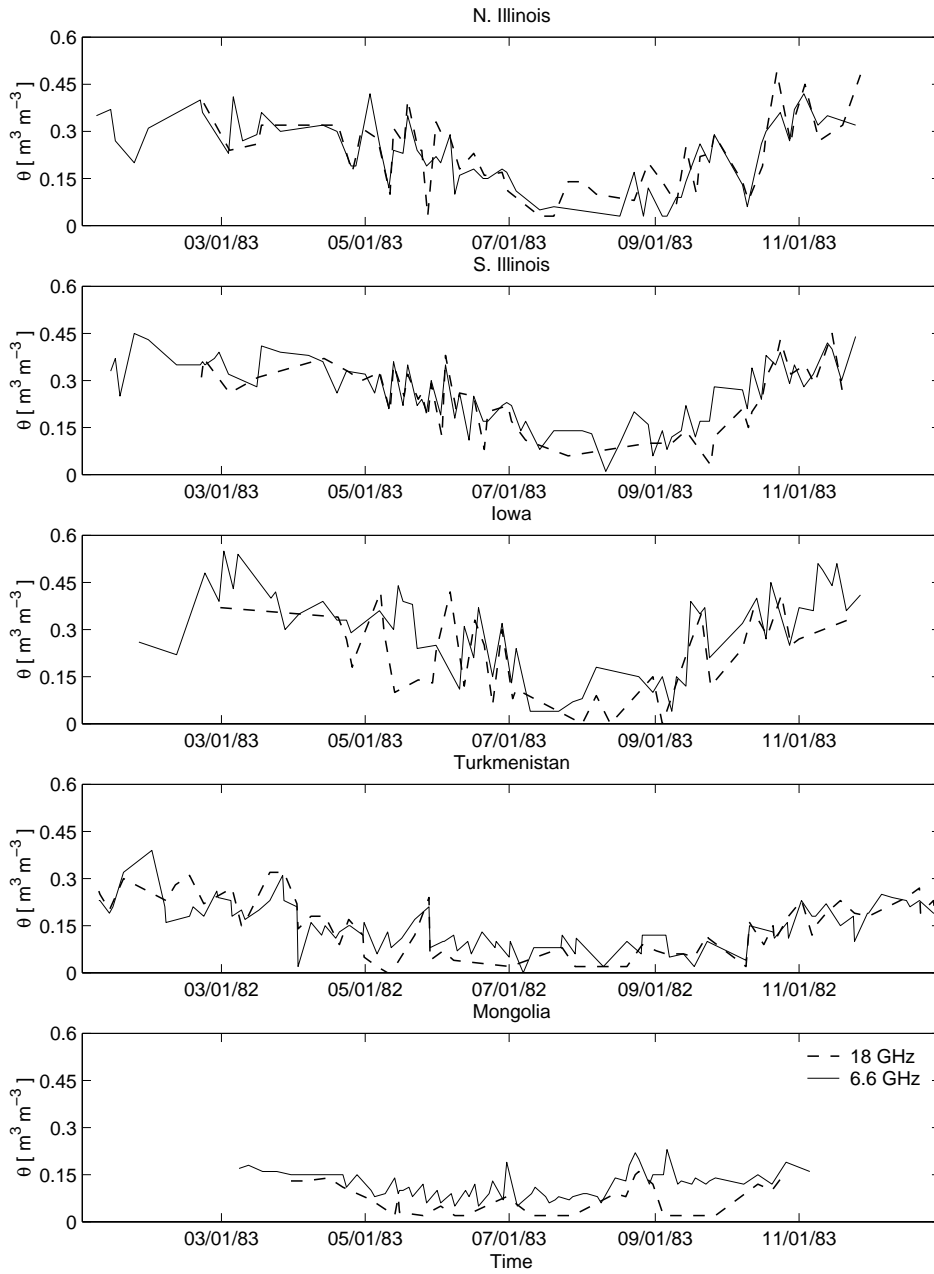


Figure 7.1: Time series of the soil moisture from 6.6 GHz and 18 GHz for the 5 test sites.

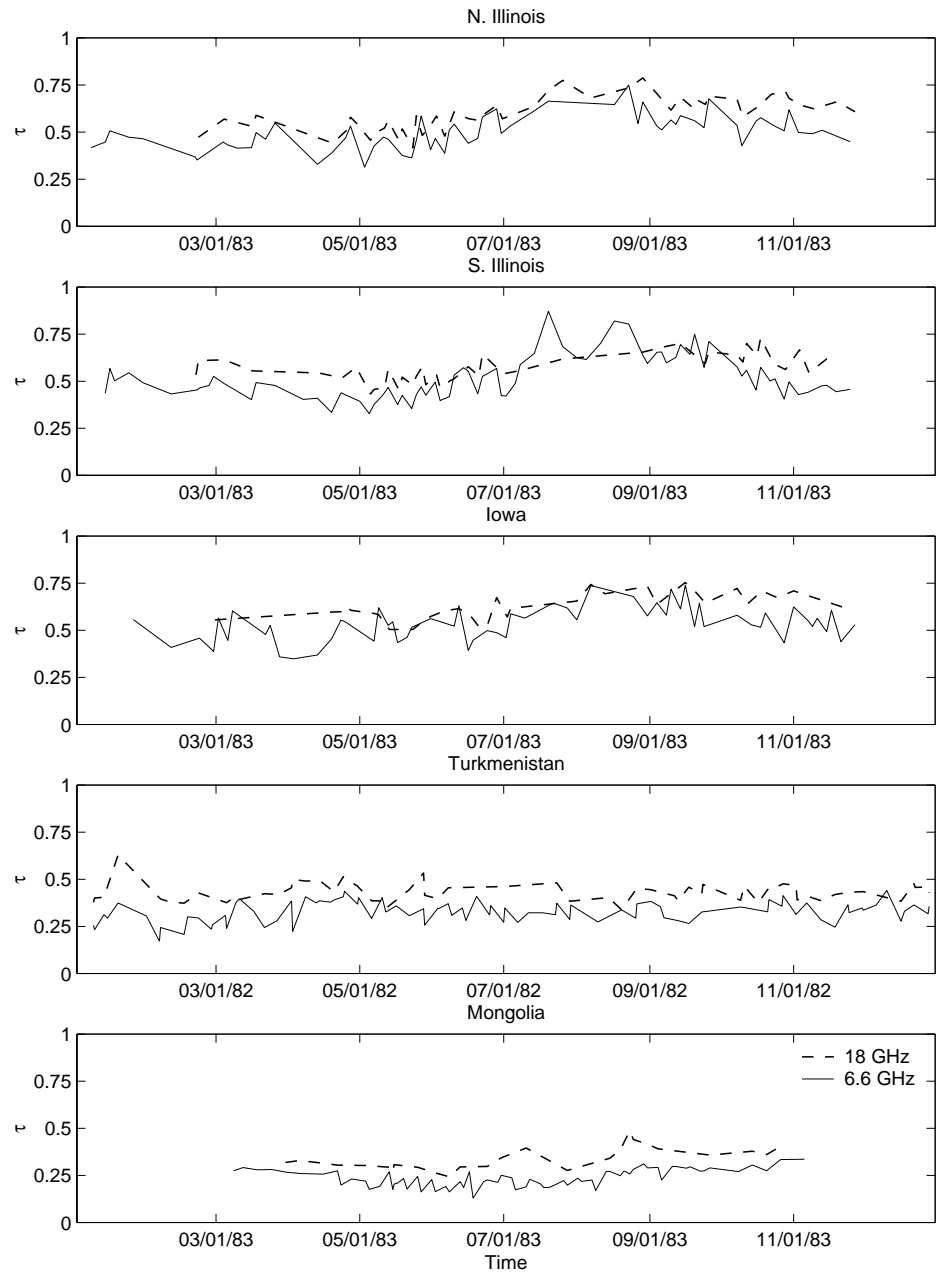


Figure 7.2: Time series of the vegetation optical depth derived from 6.6 GHz and 18 GHz for the 5 test site.

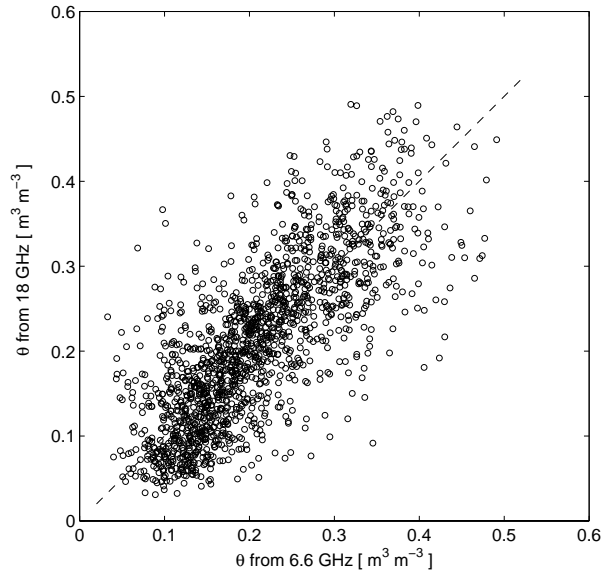


Figure 7.3: The soil moisture derived from the 6.6 GHz signals versus the soil moisture from 18 GHz. $R^2 = 0.60$, S.E.E. = $0.06 \text{ m}^3 \text{ m}^{-3}$ for 1614 (n) points.

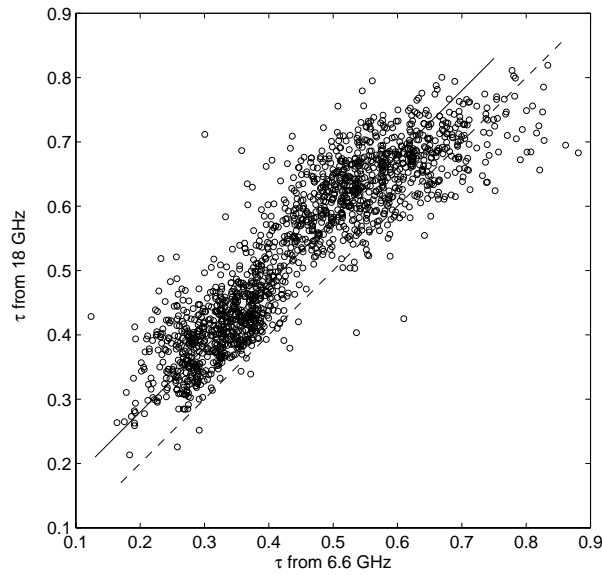


Figure 7.4: The vegetation optical depth derived from the 6.6 GHz signals versus the vegetation optical depth from 18 GHz. The dotted line indicates the 1:1 relation and the solid line the regression line. $R^2 = 0.81$, S.E.E. = 0.06 for 1614 (n) points.

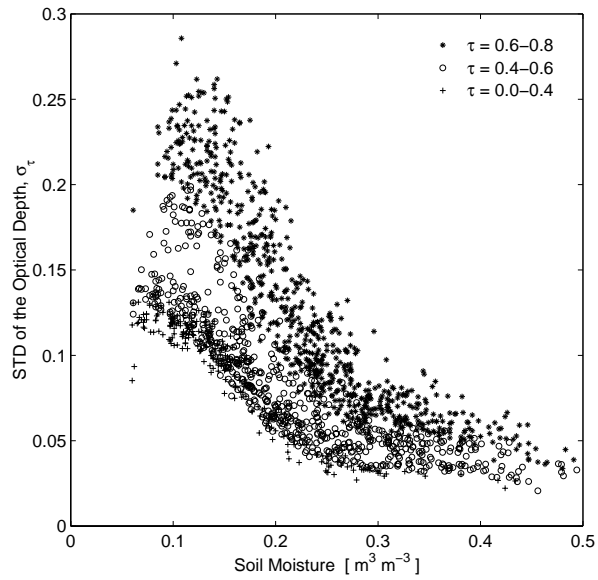


Figure 7.5: The standard deviation of the vegetation optical depth as related to the soil moisture. These values are derived from the 5 test sites with the 18 GHz brightness temperatures.

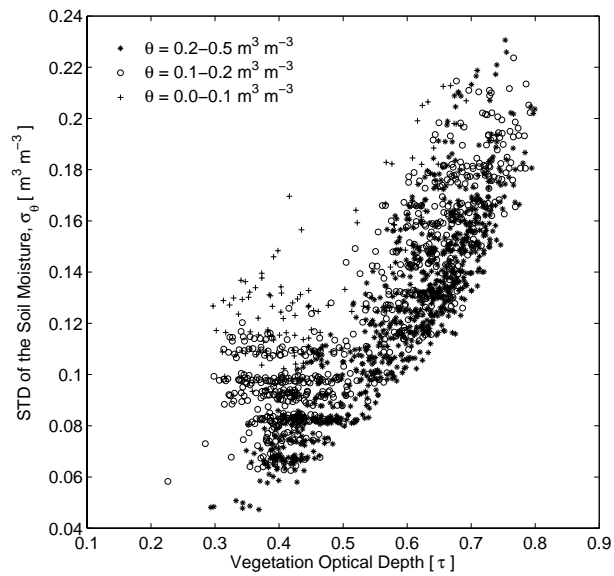


Figure 7.6: The standard deviation of the soil moisture as related to the vegetation optical depth. These values are derived from the 5 test sites with the 18 GHz brightness temperatures.

Chapter 8

APPLICATIONS

8.1 Introduction

Satellite derived land surface parameters can be used in a variety of applications. This chapter will discuss some of these and will also suggest others.

The first part will deal with the vegetation optical depth, which is somewhat less quantifiable than other parameters. Although the optical depth does not lend itself to be easily measured in the field, it has been shown to be closely related to vegetation water content, canopy structure, and biomass (Kerr and Wigneron, 1994). To demonstrate these relationships, some comparisons will be made between these parameters and the vegetation optical depth, along with their global distribution.

The second part will deal with the most appealing retrieved parameter, the soil moisture. One of the most important applications for this satellite derived parameter in current research is its use in General Circulation Models (GCMs). Numerous researchers have already indicated that accurate initialization of soil moisture in fully coupled GCMs has the potential to greatly increase the accuracy of climatological and hydrological predictions (Entekhabi et al., 1999; Walker and Houser, 2001).

This chapter however, will concentrate more on the direct monitoring capabilities of the satellite soil moisture retrievals, such as responses to precipitation.

The last part will deal with the soil temperature, and in particular the use of a time series analysis on this land surface parameter. A time series analysis can be a powerful tool to quantify the soil temperature dynamics in space and time. A simple model will be presented and some preliminary results of long-term change detection will be discussed.

8.2 Global Vegetation Monitoring

8.2.1 Introduction

Passive microwave radiometry has been used over land surfaces, primarily to assess surface soil moisture. However, vegetation canopies significantly influence the

observed signal and must be taken into account in any soil moisture retrieval algorithm (Kerr and Wigneron, 1994).

Numerous researchers (Jackson et al., 1982; Calvet et al., 1994; Kerr and Wigneron, 1994; Wegmüller et al., 1994; Njoku and Li, 1999) have already demonstrated the potential of the use of microwave signals for retrieving biophysical parameters such as vegetation water content, biomass, or leaf area index. Many of these parameters are not obtainable with visible, near infrared or thermal remote sensing techniques. However, techniques for using passive microwave radiometry for retrieving vegetation properties are not fully mature either.

One of the first successful attempts to retrieve vegetation parameters by passive microwave remote sensing was reported by Jackson and O'Neill (1990) and Jackson and Schmugge (1991). It was suggested that the vegetation optical depth (τ) could be written as:

$$\tau = bVWC \quad (8.1)$$

where b is a constant that depends on the vegetation structure and frequency, and VWC is the vegetation water content in kg m^{-2} .

Later, Le Vine and Karam (1996) tested this hypothesis with a discrete scatter model for vegetation, as developed by several authors (Karam and Fung, 1988; Karam et al., 1992; Lang, 1981; Lang et al., 1986). They concluded that for real canopies, b is also a function of the vegetation water content.

With the current methodology, it is possible to retrieve vegetation optical depth with different microwave frequencies (*e.g.* 18 and 6.6 GHz). However, the most important advantage of this new approach is that it is physically-based and does not require any ground data or other supporting measurements for calibration purposes.

8.2.2 Global Vegetation Mapping

Global vegetation optical depth maps at $\frac{1}{4}$ degree resolution were derived by applying the model to 6.6 GHz Nimbus/SMMR microwave observations for 1983 (See Section 5.2). Surface soil temperature was calculated as described previously in Chapter 4. Soil properties, like wilting point and porosity, were obtained from the LDAS (Houser et al., 2000; Mitchell et al., 2000) for the United States and from the ISLSCP (Meeson et al., 1995; Sellers et al., 1995; Zobler, 1986) for the remainder of the world (See Section 3.2.2).

Data retrieval is not possible under certain conditions, and data cells will typically be masked out in these situations. Cells falling along coastlines and extending inland approximately 100 km are not processed because of the influence of water surfaces on the observed microwave signal (boundary effect; See Section 3.1.1). This phenomenon is illustrated quite clearly in Figure 8.1. Other conditions resulting in no data retrieval are pixels with snow cover, frozen surfaces, and when vegetation cover is sufficiently great so as to saturate the signal. In addition, Central Europe has no reliable data, because the 6.6 GHz microwave retrievals are disturbed by radio signals. A masking routine (Section 6.3) is applied to the global maps so that all non processed land data cells are treated uniformly.

Both day-time and night-time optical depth maps are typically produced, with a

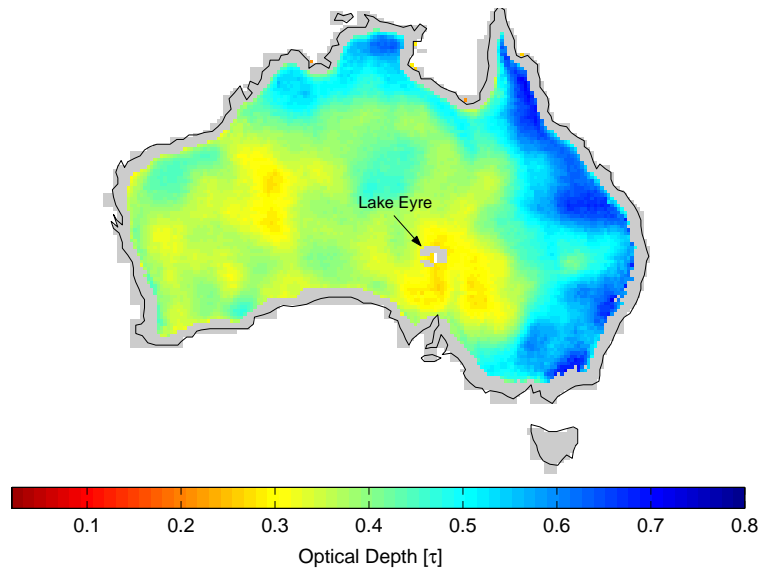


Figure 8.1: A monthly composite of the vegetation optical depth for Australia during July 1983. This image clearly illustrates the boundary effect with the masked pixels (gray) along the coastlines and surrounding Lake Eyre in the south central site of Australia.

temporal coverage of approximately 5 to 8 day-time and 5 to 8 night-time maps per month.

Since the optical depth is a function of VWC (Jackson and O'Neill, 1990), it is also related to vegetation biomass. Monthly composites of global optical depth were subsequently developed for comparison to other indicators of biomass. NDVI and LAI were selected, since the NDVI is a good indicator of biomass and the LAI is a physical parameter that represents vegetation density in m^2 leaves per m^2 soil. And both are available as a historical global data product (Los et al., 2000) (See Section 3.1.3 and 3.2.1.1).

Average monthly global images of optical depth are compared to monthly composite images of both NDVI and LAI for selected months during 1983 (See Figure 8.2 and 8.3). Comparisons are made in the context of a land classification map developed by Defries and Townsend (1994). This classification map (Figure 8.4) is described in Section 3.2.1.2. Cover types are defined in Table 8.1.

While all data sets are presented as monthly composites, it is important not to forget key differences in the manner in which the data sets are derived and processed. The optical depth data are true mean pixel values for all available data retrievals in a given month. The LAI values, on the other hand, are derived from NDVI data, where the composite image is presented by single values for each pixel (usually the greatest value) for the given time period. The major drawback of this process, is the inability to provide temporal resolution within the composite period. Consequently, values are often overestimated.

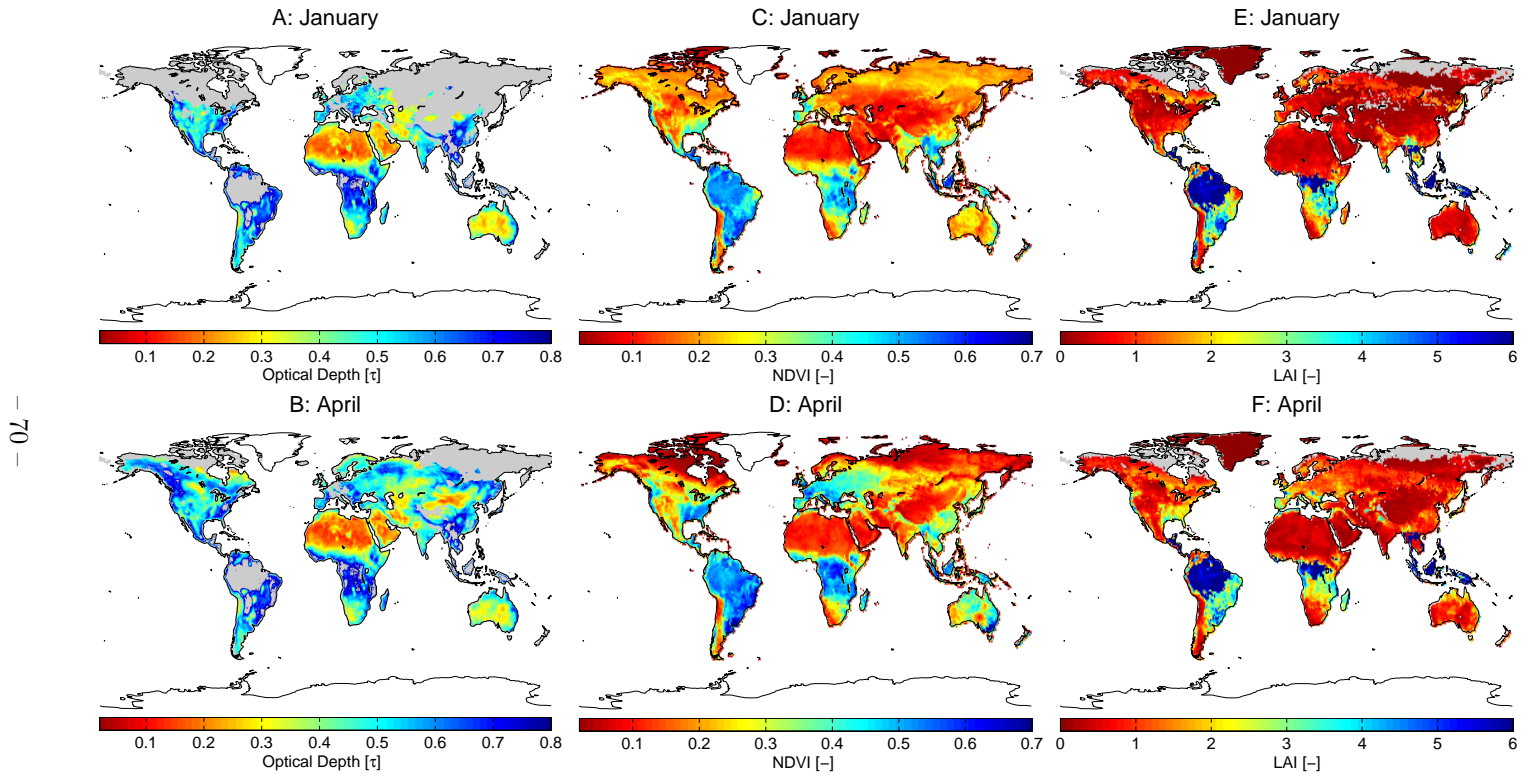


Figure 8.2: Global monthly composites of vegetation optical depth (A and B), NDVI (C and D), and LAI (E and F) representing January, and April respectively for 1983. Missing data are represented by the color gray .

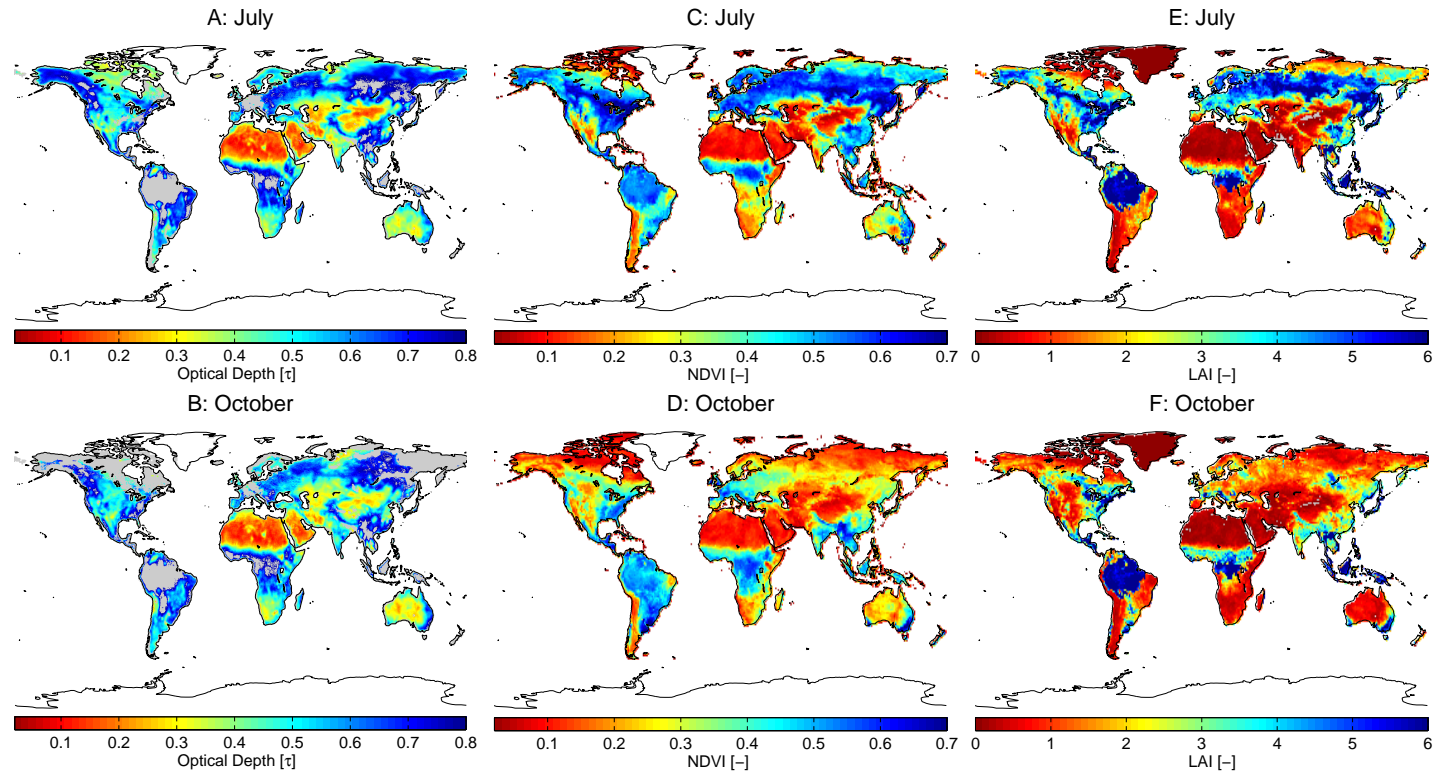


Figure 8.3: Global monthly composites of vegetation optical depth (A and B), NDVI (C and D), and LAI (E and F) representing July, and October respectively for 1983. Missing data are represented by the color gray .

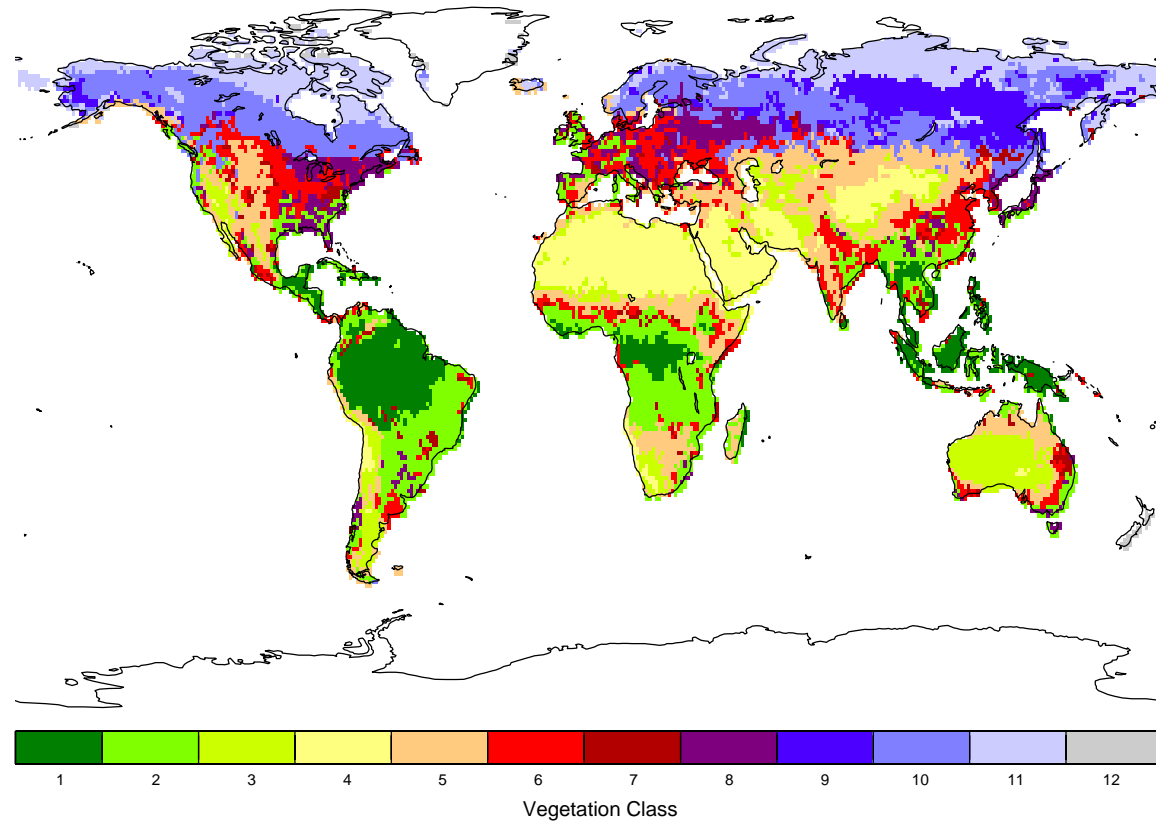


Figure 8.4: The land cover classification map developed by Defries and Townshend (1994)

Class	Description	Mean τ	Min τ	Max τ	Mean NDVI	Min NDVI	Max NDVI	Mean LAI	Min LAI	Max LAI	% of total Land Cover
1	broadleaf evergreen forest	0.80	0.80	0.80	0.51	0.44	0.55	5.97	5.97	5.97	8
2	wooded grassland	0.59	0.51	0.67	0.43	0.29	0.54	2.04	0.70	3.91	13
3	shrubs and bare ground	0.34	0.29	0.39	0.18	0.14	0.22	0.56	0.28	1.04	7
4	desert, bare ground	0.21	0.17	0.25	0.10	0.09	0.12	0.28	0.15	0.47	10
5	grassland	0.43	0.36	0.49	0.24	0.14	0.35	0.98	0.25	2.27	14
6	cultivation	0.49	0.39	0.58	0.34	0.18	0.52	1.77	0.37	4.30	9
7	broadleaf deciduous forest and woodland	0.55	0.47	0.64	0.37	0.22	0.54	2.11	0.60	4.68	2
8	mixed coniferous and broadleaf deciduous forest and woodland	0.54	0.41	0.64	0.40	0.18	0.59	2.64	0.29	5.38	5
9	high latitude deciduous forest and woodland	0.68	0.57	0.75	0.32	0.14	0.59	1.66	0.09	5.24	6
10	coniferous forest and woodland	0.54	0.46	0.61	0.31	0.14	0.54	2.00	0.94	4.67	13
11	tundra	0.37	0.33	0.40	0.17	0.04	0.33	0.81	0.11	1.79	12
12	Missing Data										1

Table 8.1: Median vegetation optical depth (τ), NDVI, and LAI values for different land covers derived from the Mean, Maximum and Minimum monthly images of 1983

The other key difference between the optical depth and NDVI-based data sets is in the physical nature of the actual radiation signals and how the parameters are derived.

The maps of global optical depth are generally in agreement with the global images of both NDVI and LAI.

High NDVI and LAI values can be found in the broadleaf evergreen forests (tropical rain forests) with NDVI values of about 0.5 and LAI values of approximately 6. This vegetation type is most of the time too dense to retrieve reliable vegetation optical depth values and are therefore often masked out. However, the remaining pixels of this vegetation type have τ values close to 0.8.

Low values can be found in the deserts with an average τ of 0.2, NDVI of 0.1 and a LAI of 0.3.

Major differences between the three global vegetation images can be found on the African continent. On this continent one can see that the vegetation optical depth is much less dynamic during a year than the NDVI and LAI. The vegetation optical depth is largely a function of the VWC and total biomass, and the seasonal variation of these biophysical properties does not vary as much as the NDVI and LAI.

Another striking example is the eastern area of the U.S. in the Appalachian mountains. The vegetation optical depth stays high the entire year with an average value of 0.75, while the NDVI and the LAI changes from 0.3 and 0.5 in January to 0.7 and 6 in July. This area is densely forested with mainly hemlock, hickory and oak. These trees are leafless in winter, resulting in low NDVI and LAI values. However, the vegetation optical depth stays high, because in winter there is still water left in the stems and branches of the trees.

8.2.3 Conclusions

Monthly composite images of vegetation optical depth showed good similarity with the monthly NDVI and LAI composites and also the vegetation classification map of Defries and Townsend (1994).

Differences between the τ maps and the conventional NDVI and LAI maps were detected mainly in vegetation class 2 and 8 (*i.e.* wooded grassland and mixed coniferous forest and woodland). In these areas the trees are leafless in winter, resulting in a distinct seasonal NDVI and LAI patterns. The vegetation optical depth is largely a function of the VWC and total biomass, and the seasonal variation of these biophysical properties does not vary as much as the NDVI and LAI.

Until now, most of the biophysical data (*e.g.* LAI or greenness fraction) used in land surface models, are derived from NDVI data. However, the vegetation index also has some negative aspects, because it can not retrieve reliable NDVI and LAI data under cloudy conditions. Another drawback is the compositing process itself, which is discussed earlier (Section 8.2.2).

The vegetation optical depth can be an important contribution to the derivation of biophysical properties like VWC and biomass. It can also increase the reliability of the NDVI derived biophysical data, because the microwave signals penetrate clouds and the optical depth data product could improve the temporal resolution of bio-

physical data products.

In combination with the SSM/I data it is also possible to obtain more than 20 years of global τ data, which can give a significant contribution in climate research.

8.3 Soil Moisture Dynamics

8.3.1 Introduction

Desertification and flooding are complex land degradation processes, which involve man, the environment and most certainly climate. Additional research is needed to quantify, assess, and further monitor these processes and other related environmental changes, such as changes in vegetation type (species composition), fractional ground cover, surface soil properties, and land use (Choudhury, 1993). The methodologies described in this research, may provide a quantitative and systematic manner in which to monitor these changes.

This Section describes an example of environmental change monitoring by applying the methodologies developed during this research by observing the Indian Monsoon. This region experiences seasonal precipitation extremes throughout the year, which subsequently are reflected in the surface soil moisture. Specific characteristics of the Indian Monsoon are discussed and followed by monthly averaged maps of satellite-retrieved surface soil moisture. The maps are compared to typical Monsoon circulation patterns and monthly precipitation totals for the region.

8.3.2 The Indian Monsoon

The monsoon circulation in the tropics is caused by the annual cycle of land-ocean surface temperature difference along with the seasonal reversal in the sea surface temperature difference between the hemispheres (Rasmusson et al., 1992). The Asian-Australian monsoon system is the dominant monsoon circulation on the earth. During the winter phase of the monsoon, there is a low-level flow of dry, cool air from the cold continent to the warmer ocean, and precipitation over land is generally light. During summer, there is a strong flow of atmospheric moisture from the tropical ocean to the warmer land, where the upward motion of the heated air produces the heavy rains of the monsoon season (Hastenrath, 1985).

For the Indian peninsula this results in a climate with a distinct seasonal precipitation pattern. The precipitation maps in Figure 8.5 and 8.6 give a graphical presentation of the seasonal climate of this subcontinent. The maps were developed by the Climate Research Unit and represent a mean monthly 0.5 degree precipitation grid of 1983. A description of this set can be found in Section 3.3.1.

From January till March, during the cool season, the winter monsoon prevails with air temperatures between 293 K and 298 K, and low precipitation rates ($< 25 \text{ mm month}^{-1}$). For the hot and dry season (March till May) the temperature rises quickly above 300 K but the precipitation rate stays below $100 \text{ mm month}^{-1}$. During the wet season (June-September) the summer monsoon prevails, giving more than 80 % of the annual precipitation, which is approximately $2000 \text{ mm year}^{-1}$. The rain

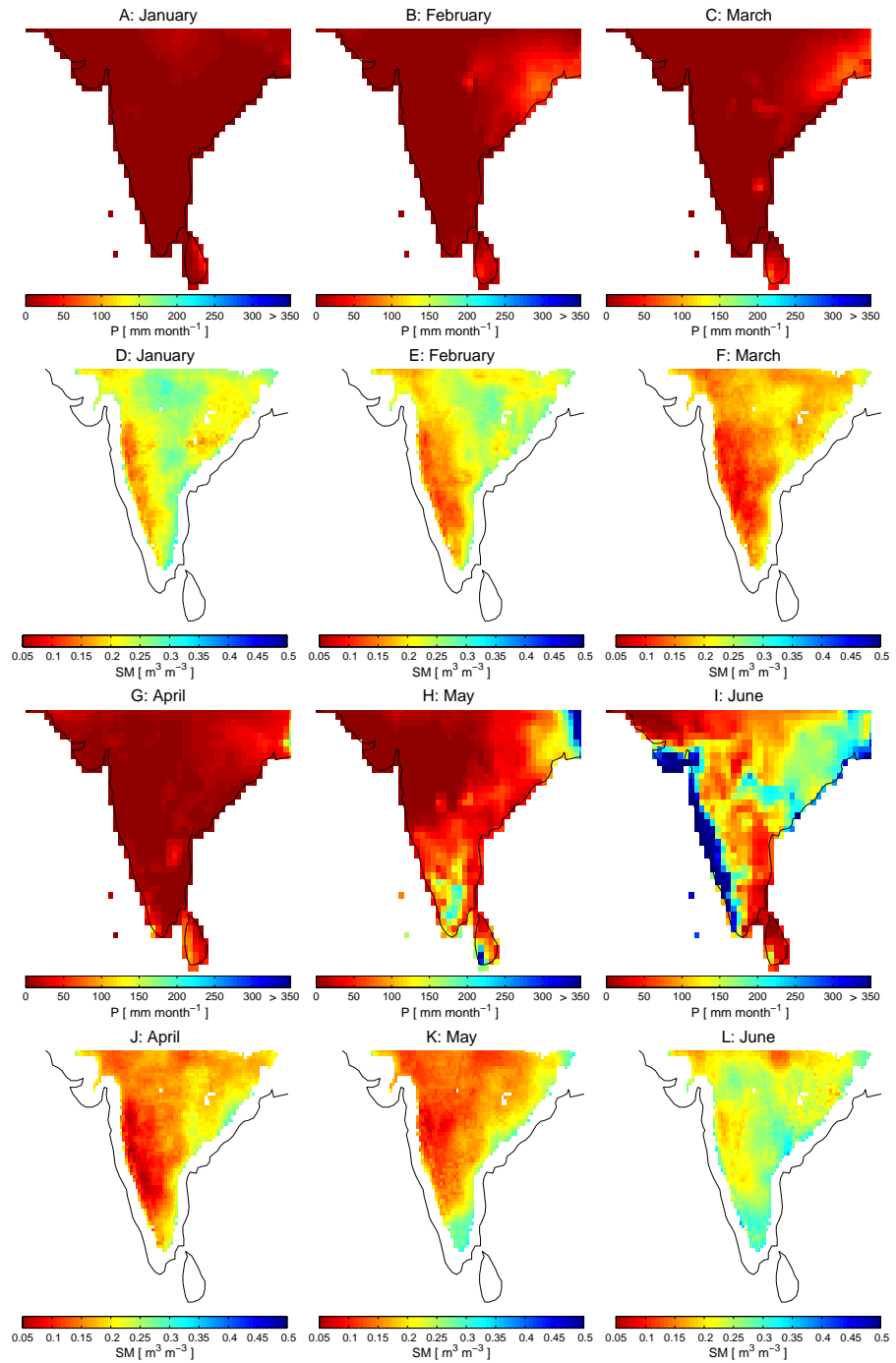


Figure 8.5: Mean monthly precipitation (A, B, C, G, H and I) and soil moisture (D, E, F, J, K and L) composites from the Indian peninsula of 1983. This Figure represents the first six months.

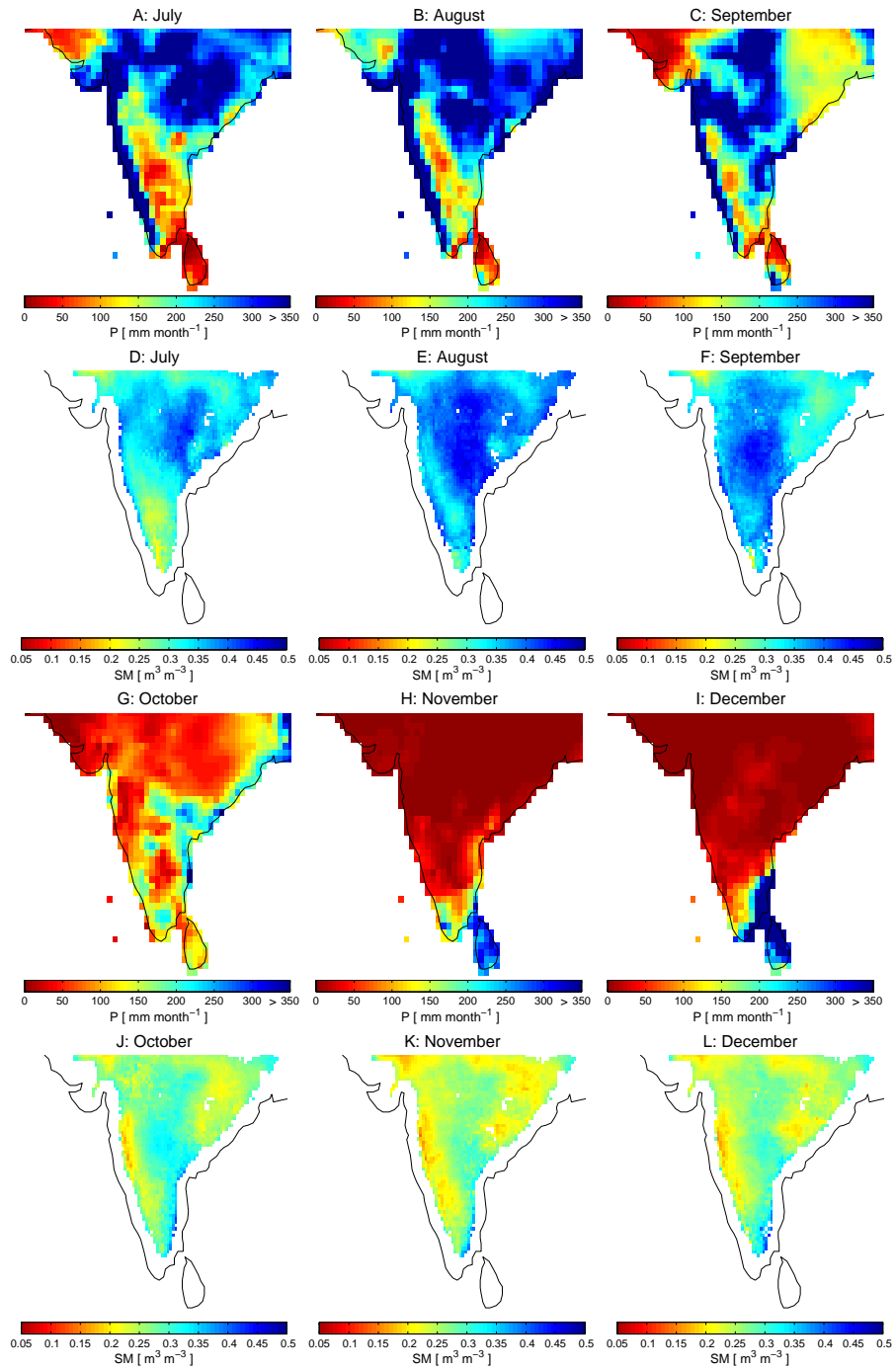


Figure 8.6: Mean monthly precipitation (A, B, C, G, H and I) and soil moisture (D, E, F, J, K and L) composites from the Indian peninsula of 1983. This Figure represents the last six months.

migrates from east to west, with the highest precipitation rates along the west coast as a result of orographic lifting. During this period the temperature drops about 5 K. From October till December the monsoon retreats in a southeasterly direction, resulting in higher temperatures of about 300 K. However, these values are not as high as the values during the March-May period (Rao, 1981).

8.3.3 Annual Soil Moisture Changes versus Monsoon Circulation

Soil moisture retrievals were used to compile monthly average soil moisture maps of the Indian peninsula for 1983 (Figure 8.5 and 8.6). These images give a remarkable spatial imprint of the Indian monsoon circulation, showing dry values below $0.15 \text{ m}^3 \text{ m}^{-3}$ in April-May and wet values above $0.35 \text{ m}^3 \text{ m}^{-3}$ during the summer monsoon in August-September. During the first 5 months (January-May) there is almost no precipitation on the Indian peninsula. In January, the western part of India starts to dry up, and this drying pattern is moving northeast ward, resulting in an almost complete dry country in May. Except the south and east coast, still values above $0.15 \text{ m}^3 \text{ m}^{-3}$ are found. After May the summer monsoon arrives from the northeast, moving slowly to the southwest with monthly precipitation values beyond 250 mm. Highest soil moisture values can be found in August in central India where the values are close to saturation ($\approx 0.5 \text{ m}^3 \text{ m}^{-3}$). During this wet period the spatial distribution of the soil moisture of the months July, August and September coincide very well with the precipitation maps (See Figure 8.6). This, again shows the strong capacity of the satellite based soil moisture retrieval model to detect wet areas in a semi arid region.

After September the abundance of precipitation stops and the soil dries quickly, and in the following three months there are only limited changes in the soil moisture fields.

8.3.4 Conclusions

The satellite derived soil moisture fields appear to be quite useful for monitoring the seasonal dynamics of soil moisture at the regional, continental, and even global scale. The monthly soil moisture maps of the Indian peninsula are seen to illustrate the typical monsoonal characteristics of the region and exhibit a good correspondence with monthly rainfall. The satellite based retrieval model seems to be a powerful tool in the detection of wet areas in semi arid regions.

8.4 Time Series Analysis on the Surface Soil Temperatures

8.4.1 Introduction

The model-estimated surface soil temperatures for the 5 cm profile correspond well with field observations from the various measurement sites. Field measurements are typically quite accurate, but because they are point measurements, they are valid only for the specific sampling location. Attempts to use sparse field measurements to calculate large area spatial means, can often result in significant errors. The field observations used to derive the algorithms in Chapter 4 are from sufficiently dense sampling networks relative to the microwave footprint size, so as to result in a reliable methodology for temperature retrieval.

Spatial means of soil temperatures are not only necessary for reliable soil moisture and optical depth retrievals, they are also more conducive to independent temperature analysis. Surface soil temperature at a $\frac{1}{4}$ degree grid scale were calculated for the continental United States during the entire SMMR period (1978-1987) for a subsequent time series analysis.

8.4.2 Time Series Analysis

Decomposition of complex cell based time series in simpler periodic components is a powerful tool to analyze the seasonal behavior of the satellite derived land surface parameters. Grid cell based time series of the parameters can be defined as $I(x, y, t)$, where c is the column number or longitude, r is the row number or latitude and t is the time. $I(c, r, t)$ can be expressed as a linear combination of elementary cosine and sine functions:

$$I(c, r, t) = a(c, r)t + d_1(c, r) \cos(w_n t) + d_2(c, r) \sin(w_n t) + d_{mean}(c, r) \quad (8.2)$$

where a is the slope or long term trend, d_1 to d_2 are unknown fitting parameters, d_{mean} is the 9-year mean value and w_n is the frequency which is related to the periodicity as $w_n = \frac{2\pi}{P_n}$. When the periodicity is known (*e.g.* a year) the function can be used to fit the measured data resulting in values for a , d_1 , d_2 and d_{mean} . The phase-shift (g) or time of peak in the periodicity can be calculated by:

$$g(c, r) = \frac{\arctan\left(\frac{d_2(c, r)}{d_1(c, r)}\right)}{w_n} \quad (8.3)$$

If $I(c, r, g) < I(c, r, g + 0.5P_n)$ half a period must be added to Equation 8.3. Now the seasonal amplitude (A) can be defined as:

$$A(c, r) = |(d_1(c, r) \cos(g(c, r)w_n) + d_2(c, r) \sin(g(c, r)w_n)) - (d_1(c, r) \cos((g(c, r) + 0.5P_n)w_n) + d_2(c, r) \sin((g(c, r) + 0.5P_n)w_n))| \quad (8.4)$$

The value of the seasonal amplitude is twice the value of the amplitude as defined in wave mechanics, where the amplitude is defined as the distance from the mean position to the extreme.

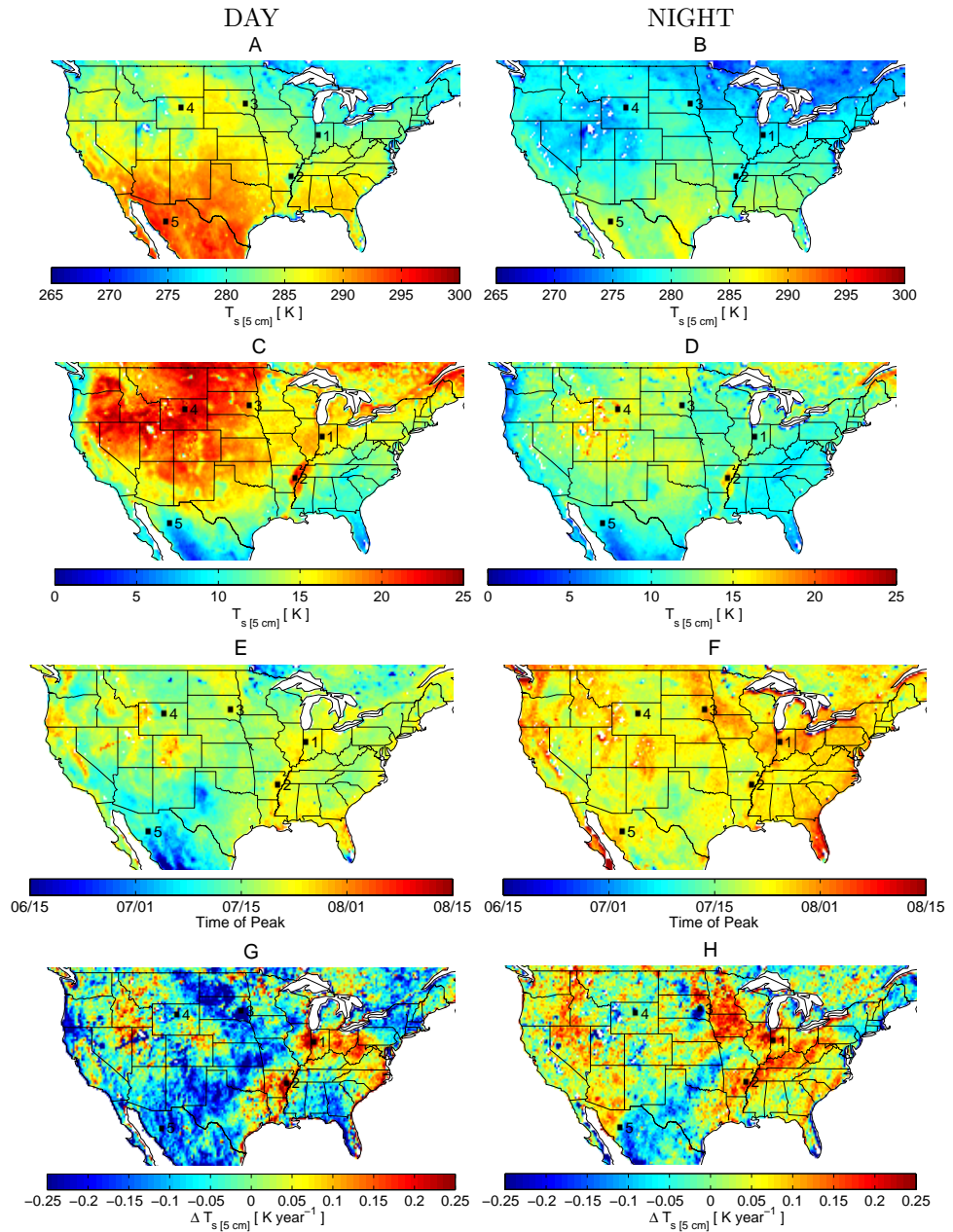


Figure 8.7: Results of a statistical time series analysis of surface soil temperature (5 cm) retrievals from satellite microwave observations for the continental U.S. during the period 1978 to 1987. The left and right panels correspond with day-time and night-time observations respectively. Maps A and B illustrate the 9-year average temperature in Kelvin; C and D the seasonal amplitude of the mean monthly annual course in Kelvin; E and F the phase-shift (time of peak) with the unit being the date; G and H the long term trend (slope) in Kelvin per year. Five pixels (numbered) were selected for more detailed analysis.

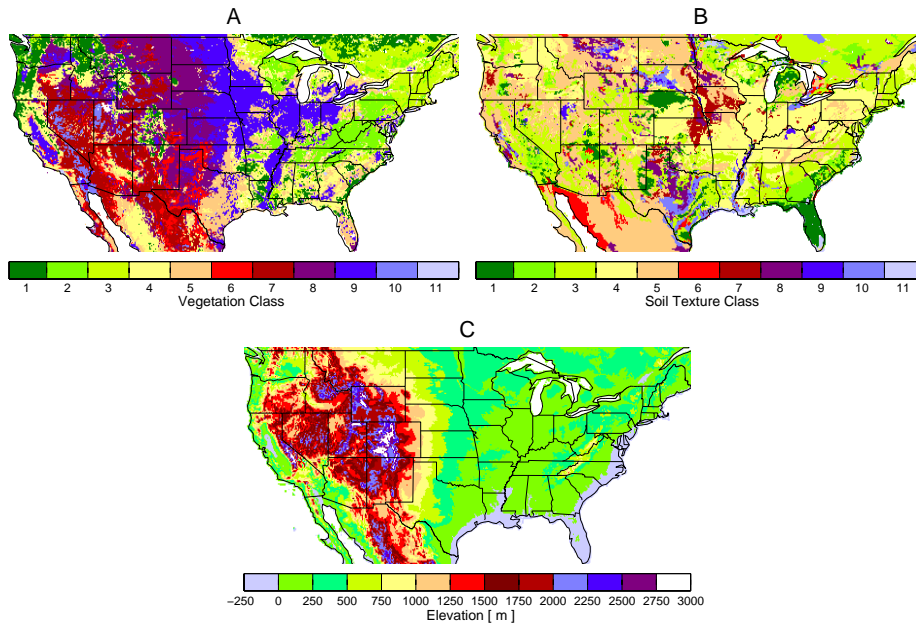


Figure 8.8: Three thematic maps of the U.S. obtained from the LDAS web site (<http://ldas.gsfc.nasa.gov/>). These maps are a (A) vegetation classification map, (B) classification map of the soil texture type, and (C) elevation map. The description of the soil and vegetation classes can be found in Table 8.2.

Class	Vegetation description	Soil description
1	Evergreen Needleleaf Forest	Sand
2	Deciduous Broadleaf Forest	Loamy Sand
3	Mixed Cover	Sandy Loam
4	Woodland	Silt Loam
5	Wooded Grassland	Loam
6	Closed Shrubland	Sandy Clay Loam
7	Open Shrubland	Silty Clay Loam
8	Grassland	Clay Loam
9	Cropland	Silty Clay
10	Bare land	Clay
11	Urban and Built up	Organic Materials

Table 8.2: Description of the soil and vegetation classes, as given in Figure 8.8.

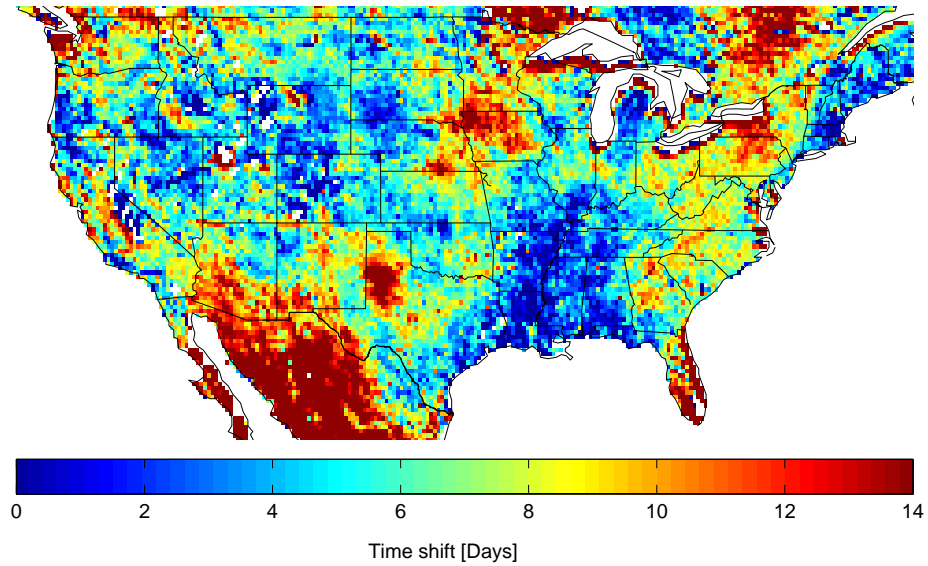


Figure 8.9: Difference (in days) between the night-time (Figure 8.7 F) and day-time (Figure 8.7 E) phase-shift of the soil temperature at 5 cm depth.

8.4.3 Application to the Continental United States

A time series analysis, as previously described, was conducted with the 5 cm soil temperature for the entire SMMR period of record. Soil temperatures were derived from 37 GHz vertical polarization data according to the procedure described in Chapter 4.

To reduce the computing time, monthly averages were calculated. The periodicity (P_n) is set to 12 months and the time series analysis is applied to 106 months of $T_{s[5cm]}$ (*i.e.* from November 1978 to August 1987). The unknown parameters a , d_1 , d_2 and d_{mean} are solved by multiple linear regression analysis, resulting in a 9-year mean (d_{mean}), a seasonal amplitude (A), a phase-shift (g), and a long term trend (a) of the day-time and night-time $T_{s[5cm]}$. Figure 8.7 shows the resulting maps. Topographical, vegetation, and soil maps are provided (Figure 8.8) to assist in the interpretation of the time series analysis.

From the time series analysis maps (Figure 8.7), five pixels were selected based on differences in the time series analysis components. To illustrate the performance of the time series model and to compare the differences between the pixels they were plotted in time in Figure 8.10.

The 9-year mean soil temperatures (5 cm) for the continental United States illustrate typical spatial distributions as expected (Figure 8.7 A and B). The highest day-time temperatures were found in the Southwest extending into Mexico, while the lowest average day-time temperatures were found in the Northeast (and southeastern Canada), northern midwest and the higher elevations of the Rocky Mountains.

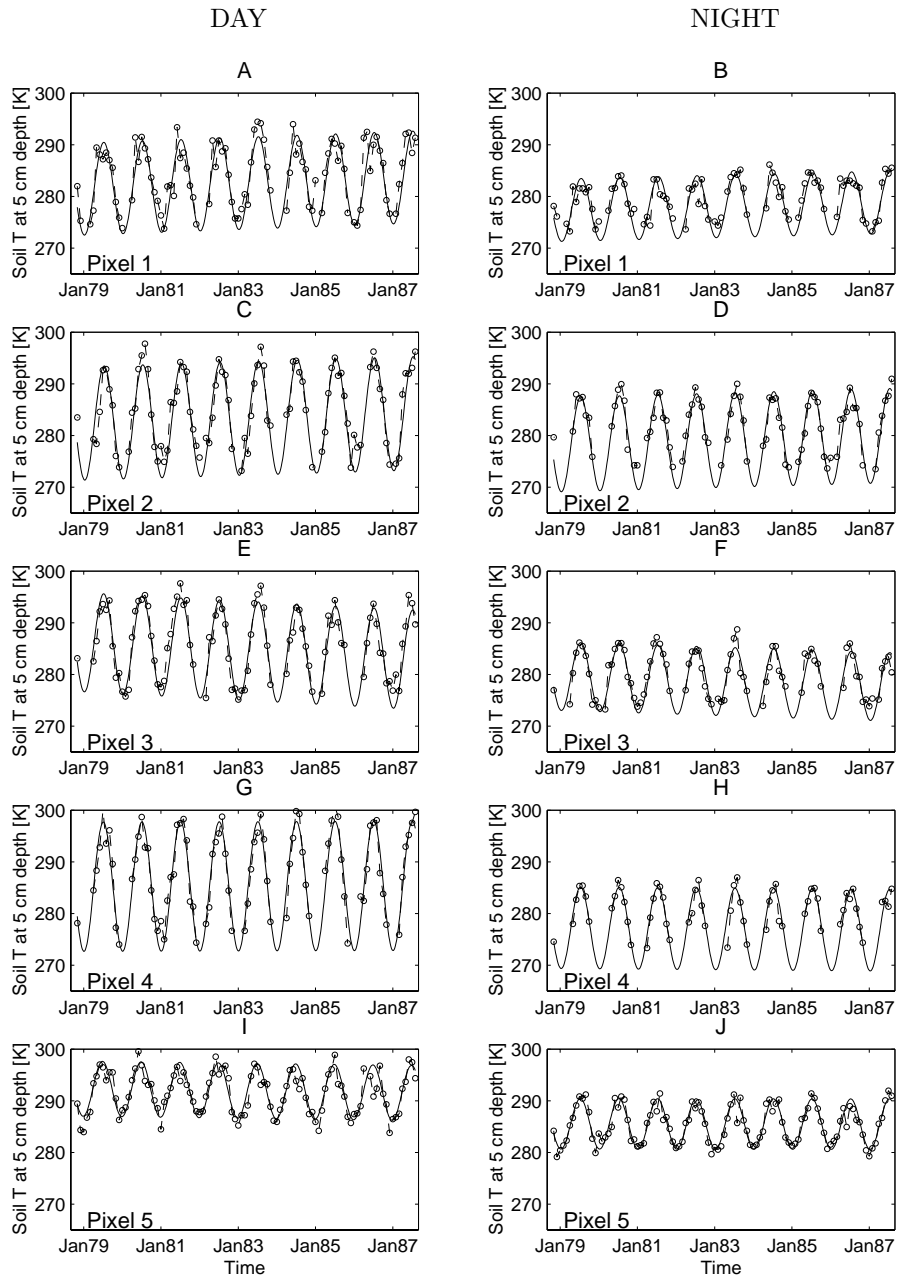


Figure 8.10: The time series of the soil surface temperature for the 5 selected pixels (as marked in Figure 8.7). The circles in combination with the dashed line represent the satellite derived monthly average T_s values at 5 cm depth, and the solid line is the time series analysis model.

Mid-range temperatures are found in the northern Great Plains region mostly with cropland vegetation and the Southeast. The Florida peninsula remains somewhat cooler as a result of the maritime influence, as does the Mississippi valley.

9-year average night-time temperatures display similar patterns, with the lowest temperatures in the Northeast and in the mountains. The Northeast region in Canada is often covered with evergreen needleleaf forest and the predominate soil type is sandy loam. The average nighttime high temperatures, however, are more widely distributed throughout the Southwest, Southeast, western coastal region, and the southern, central and northern Great Plains.

The seasonal amplitude corresponds to the annual range in mean monthly temperature and are presented in Figure 8.7 C and D. The highest day-time values are seen to occur in the central to northern plains and mountain ranges, the Northeast, and lower Mississippi Valley. The Mississippi Valley is mostly covered with cropland and along the river the main soil type is clay. The lowest day-time values occur in the southeast and coastal areas of western Mexico, where the area is covered with woodland on a loam/sandy clay loam soil. An other area with low values is the Northwest of the U.S. where the vegetation is dominated with evergreen needleleaf forest on a sandy loam soil. The range of night-time temperatures demonstrates similar spatial patterns, although the dynamic range is significantly lower.

The phase-shift or time of peak (Figure 8.7 E and F) illustrates the spatial and temporal distribution of when the annual temperature cycle reaches its maximum. This period covers about 45 days (15 June to 1 August) throughout the region for the day-time peak and about 30 days (15 July to 15 August) for the night-time peak.

The earliest day-time peak temperatures are seen to occur in the southern-most regions west of Mississippi. The time of peak occurs progressively later with an increase in latitude, as one would expect. This trend is influenced slightly by elevation, as is observed in the Rocky Mountain regions and along the Sierra Nevada and Cascade ranges on the West Coast. In the east, including coastal waters, the Mississippi Valley and the Allegheny Ridge.

The night-time time of peak also occurs later as latitude increases, for the most part, but also appears to be influenced significantly by coastal waters and elevation.

The night-time peak temperature typically occurs sometime after the day-time peak (Figure 8.9). This lag time may be due to the heat capacity of the soil. Some of the heat that is absorbed by the soil during the day from incoming solar radiation is directed downward into the soil profile. As the lower soil profile heats up, the magnitude of the downward soil heat flux steadily decreases, and the night-time surface temperature will eventually attain a maximum.

The lag time will be affected by a number of geo- and biophysical and geographic influences, such as soil moisture, vegetation, elevation, and climatology. This difference is observed to be anywhere from 0 to about 9 days for most of the continental U.S. and surrounding region. However, the difference may be as much as 14 days in some locations. While these greater differences are seen to be almost randomly located in small patches throughout much of the region, several extended uniform areas are also observed. These areas include almost all of Mexico and extending into southern Arizona and New Mexico; the northern Texas Panhandle; almost the entire Florida peninsula; the upper Midwest region of Iowa, Minnesota and extending into

Canada; and the entire Allegheny ridge, extending through central Pennsylvania, the southern Tier of New York, and north into Canada. Equally noticeable, are extended areas with little or no difference in the time of occurrence of day-time and night-time peaks. These include the northern High Plains, the extended Mississippi Valley and virtually all of New England.

Decreases in the monthly day-time means were observed throughout the Southwest, southern, middle and northern Great Plains, and some areas in the Northeast and Southeast. Increases in monthly day-time means were noticed in the Midwest, southeastern Great Plains, and regions in the northern Rocky Mountains. Increases in the night-time monthly means was noticed in the northern Midwest, along the Appalachian Mountains, and in patchy locations along a line extending from northwestern Mexico northeastern Oklahoma (See Figure 8.7 G and H). The driving force behind the long term cooling and warming of the U.S. is unknown and remains a topic for future research.

Chapter 9

SUMMARY AND CONCLUSIONS

This chapter is a summary of:

Retrieval of Land Surface Parameters using Passive Microwave Remote Sensing.

9.1 General

The primary objective of this study was to develop a methodology to retrieve global soil moisture from satellite microwave observations. The approach was to retain a strong physical basis by using a radiative transfer equation, applicable at any wavelength, and not require any form of calibration based on other ground measurements of soil moisture. Reliance on any prior calibration procedures would introduce a regional dependency to this methodology and consequently limit its global applicability.

Three key unknowns remained in the radiative transfer equation; surface soil temperature, surface soil moisture, and vegetation optical depth. A non-linear iterative procedure, in a forward approach, was used to solve the radiative transfer equation. However, solving for all three variables simultaneously presented a mathematical challenge, resulting in frequent convergence problems.

It was decided to solve for surface soil temperature off-line, and use the above-described procedure with the remaining two variables. This approach proved to be highly successful.

There are many applications that can utilize the land surface parameters that are derived from this retrieval model. Several common examples have been provided. The retrieved parameters may be used to study soil moisture, surface soil temperature, and vegetation optical depth at a variety of spatial scales, including regional, continental, and global, and temporally, at both inter- and intra annual time scales.

9.2 Soil Temperature

Surface soil temperature is an extremely important variable in solving the radiative transfer equation for soil moisture. While the surface temperature model is inherently sound, it is regression-based, and its accuracy is limited by the availability of ground observations used for calibration.

Soil temperature retrieval within North America can probably be considered the most accurate, because most of the ground data used for calibration/validation are from this region. Consequently, overall model performance and the retrieval of the remaining parameters will probably also reflect this fact. Validation with additional surface soil temperature data sets in different environments, should lead to improvements in model performance.

The surface soil temperature is derived from vertical polarized 37 GHz brightness temperature. It has been shown that the brightness temperature at this frequency and polarization is predominantly a function of soil temperature and is not markedly influenced by the atmosphere or soil moisture.

The brightness temperatures were compared with field soil temperatures at 5 cm depth from Oklahoma, and a linear relation between those two parameters was developed. Temperatures of the emitting layer were retrieved by using the satellite derived soil temperature at 5 cm depth in combination with an interpolation technique. The interpolation technique was based on soil temperature observations at both 1.25 cm and 5 cm from Maryland (BARC) and Botswana.

9.3 Soil Moisture and Vegetation Optical Depth

Microwave vegetation optical depth may be a highly useful tool for monitoring various biophysical aspects of vegetation. While this parameter has some distinct advantages over visible/near infrared instruments, such as all-weather capability, it is not meant to replace these. Because these various parameters are derived from different sensors, and hence, are a response to totally different biophysical properties, they should complement each other. When taken together, their interpretation should yield a more accurate picture of vegetation biophysical characteristics.

Soil moisture retrieval by microwave has been shown to be the most reliable remote sensing technique, since the up-welling microwave energy is a direct response to the absolute water content in the soil. The retrieval method presented here, is a direct radiative transfer approach, and requires no calibration based on geographic location, vegetation biophysical properties, or other ground-based data sets of soil moisture. It appears to be the first technique of its kind to successfully retrieve space-based estimates of absolute soil moisture at the global scale.

While the approach has definite limitations, these are the result of the inherent limitations which define microwave physics, and are not a function of the model. Optimum model performance can be expected to coincide with the use of optimum microwave sensor data, which is known to be at the L-band wavelength. The model may be directly applied to the new AMSR observations, which are expected to be highly similar to the SMMR data utilized for this study. Some improvement may be realized,

however, as a result of the improved spatial resolution of the new radiometer. Soil moisture and vegetation optical depth are retrieved from dual polarized microwave brightness temperature observations, and were applied to 6.6 GHz SMMR data.

Some assumptions regarding the different elements of the radiative transfer equation are made in order to reduce the number of variables. The model assumes a constant value for the scattering albedo, based on a series of previous studies. A soil roughness parameter is also not included because it has been hypothesized that roughness has a minimal effect at satellite scale. Days with snow cover or when surface temperatures were below zero were eliminated from the analysis.

A non-linear iterative approach is used to solve for the surface moisture and vegetation optical depth, both of which are derived from the soil dielectric constant.

The model was applied to several sites with observations of surface moisture, located in the U.S., Mongolia and Turkmenistan. Time series of the satellite-derived surface moisture compared well with the available ground observations and precipitation data. The vegetation optical depth showed similar seasonal patterns as the NDVI.

9.4 Model Sensitivity

An error propagation analysis was applied to the satellite derived land surface parameters from the U.S. and Eurasian study sites. The standard deviation of the retrieved surface soil temperature was small and on average 1.2 degrees Kelvin for all test sites. The standard deviations of the retrieved soil moisture were high when the vegetation optical depth is high. The soil emission is attenuated by vegetation, and when the vegetation density increases, the sensitivity of the microwave sensor to retrieve soil moisture information will decrease.

Low soil moisture values also have high standard deviations. These high deviations were due to the low sensitivity of the dielectric of the soil on soil moisture when it is dry

Optimum results in the detection of accurate soil moisture with the satellite retrieval model can be obtained with high soil moisture values under sparse vegetation.

Compared with wet conditions, the uncertainty of the vegetation optical depth is high at dry conditions. This phenomenon also has a theoretical basis. At low moisture conditions, the soil emission is high and the additional contribution to the overall observed emissivity from low levels of vegetation is also low. As soil moisture increases, the soil cools and the emission becomes lower, the relative contribution of the vegetation of the overall observed emissivity becomes more significant.

To increase the reliability of the retrieved land surface parameters, a masking routine has been applied. This consists of a pixel masking for pixels with snow cover, frozen soil and excessive dense vegetation cover. Pixels with snow were detected with a difference algorithm and frozen soils with the newly developed surface soil temperature algorithm. Beyond a vegetation optical depth of 0.8 the satellite retrieval model doesn't generate reliable soil moisture and vegetation optical depth information anymore and under these circumstances both the vegetation optical depth and soil moisture were masked out.

9.5 Wavelength Effects

The land surface parameter retrievals from 18 GHz observations appear to be consistent with the 6.6 GHz results in most instances, therefore supporting the use of the 19.4 GHz observations from SSM/I to extend the soil moisture and optical depth data base. However, the limitations of the higher frequency observations are significantly greater.

First, the penetration depth of 18/19.4 GHz observations is probably less than 0.5 cm. Also, since the ability to detect changes in soil moisture is severely reduced at an optical depth above 0.65 and since vegetation optical depth is inversely proportional to the wavelength, an optical depth of 0.65 corresponds to a much thinner canopy layer at 18 GHz than at 6.6 GHz.

Additionally, atmospheric influences, primarily precipitable water, becomes more significant at frequencies above 10 GHz. In order to optimize surface soil moisture retrievals, it is strongly recommended that an atmospheric correction component be added when using higher frequency observations.

9.6 Applications

While the primary objective of this study was the development of the land surface parameter retrieval algorithm, examples of potential applications for these parameters were also demonstrated and discussed.

Time series of vegetation optical depth were compared to both NDVI and LAI. While the long term trend between optical depth and the other two parameters compared well, some differences were also observed. These differences are expected, however, because microwave and visible/near infrared respond to different biophysical characteristics and energy sources. Additionally, visible/near infrared measurements are typically reported as a composite over time (usually 15 days or monthly) because of frequent adverse atmospheric effects. Optical depth measurements, on the other hand, are less affected by the atmosphere and therefore may provide information on vegetation characteristics at improved temporal resolution. Both microwave and visible/near infrared data products provide information on various aspects of vegetation growth characteristics, and information retrieval may be maximized when they are taken together.

While spatially averaged surface temperature is extremely important for solving the radiative transfer equation, it is also a valuable tool by itself. Surface temperature can be especially useful for global studies of land surface cover characteristics and other long term environmental changes.

Regular observations of spatially representative surface soil moisture may be extremely useful for studies of meteorological phenomena and long term environmental changes such as global climate change, studying the effects of land use change, and in the validation of general circulation models. It has also been determined that accurate initialization of land surface moisture is critical for seasonal-to-interannual climatological and hydrologic prediction.

9.7 Follow-up Studies

A number of logical follow-up studies have been identified during this investigation, and are described briefly below.

Additional soil temperature-brightness temperature studies

Improvements to the surface temperature algorithm should significantly improve the accuracy of the soil moisture and optical depth retrievals. The temperature model is currently based only on measurements from Oklahoma, Maryland, and Botswana. Efforts to identify additional data sets of near-surface temperature observations made under a variety of different surface cover conditions will be made, while recommendations to modify on-going and planned field experiments to include such measurements will also be made. Application of the retrieval model to new sensor platforms such as AMSR and SMOS will be significantly enhanced by improvement in surface temperature estimation.

Global studies of surface temperature

The surface soil temperature data set will be extended with retrievals from vertical polarization 37 GHz observations from SSM/I to yield a 25 year record. Long term studies of global surface temperature could be useful in studies of global warming, by identifying temperature changes in environmentally sensitive locations.

Atmospheric correction for higher frequency brightness temperature above 10 GHz

Horizontal polarization brightness temperature at frequencies above 10 GHz are subject to atmospheric influences, especially from precipitable water in the atmosphere. The effect on the horizontal brightness temperature can be as large as 10 Kelvin in extreme cases, indicating a strong need to apply an atmospheric correction. Microwave data from both TRMM and SSM/I will be corrected for atmospheric precipitable water before use in the retrieval model.

Application of the land surface data retrieval model to SSM/I and TRMM observations

The global surface soil moisture and optical depth data sets will be extended until the present term with SSM/I and TRMM observations.

Retrieval model application to AMSR

The retrieval model will be applied to observations from the Advanced Microwave Scanning Radiometer (AMSR) on board both the Advanced Earth Observing Satellite II (ADEOS-II) and AQUA, when these data become available. These sensor missions are supported by elaborate field campaigns, which should provide excellent ground data observations for improved model validation.

Analysis of global surface soil moisture

The 25+ year history of global surface soil moisture will be analyzed for existing spatial and temporal trends by a variety analysis techniques such as fourier analysis

and other trend analysis techniques. Such studies may provide information about climate change and climate anomalies such as El Niño-Southern Oscillation, especially in combination with the derived vegetation and soil temperature information.

Analysis of global vegetation optical depth

The microwave vegetation optical depth has a strong physical relationship with vegetation water content and possibly plant geometry and biomass of the overlying canopy. Attempts to derive biophysical properties from vegetation optical depth have been limited and largely empirical, for the most part. An effort will be made to derive a more physically based interpretation for the vegetation optical depth and also develop more physically based retrieval techniques for related vegetation biophysical parameters.

Chapter 10

SAMENVATTING EN CONCLUSIES

Dit hoofdstuk is een samenvatting van:

Bepaling van Landoppervlakteparameters uit Teledetectie van Passieve Microgolven.

10.1 Algemeen

De hier gepresenteerde studie onderzoekt de vraag of het mogelijk is om een techniek te ontwikkelen om op regionale, continentale of op globale schaal bodemvocht te bepalen met behulp van satellietwaarnemingen in het microgolvenbereik. Deze techniek moet fysisch onderbouwd zijn door middel van de theorie van stralingstransport en toepasbaar zijn bij verschillende golflengten, zodat de techniek bruikbaar is bij verschillende microgolfinstrumenten. Verder moet de techniek onafhankelijk zijn van veldwaarnemingen van bodemvocht. Want wanneer de techniek met veldwaarnemingen aan calibratie technieken gekoppeld zou zijn, dan wordt er een regionale afhankelijkheid gecreëerd en verliest de techniek zijn globale toepasbaarheid.

De stralingstransportvergelijking in het microgolvenbereik heeft drie belangrijke onbekenden; de bodemtemperatuur, het bodemvocht en de optische diepte van de vegetatie.

Een niet lineaire iteratieve procedure werd opgezet om de stralingstransportvergelijking op te lossen. Dit is niet eenvoudig, want het tegelijkertijd oplossen van de drie onbekenden resulteert vaak in convergentieproblemen. Daarom werd er besloten om de bodemtemperatuur apart te bepalen en de andere twee variabelen met de hier bovenstaande procedure op te lossen. Deze benadering bleek uiterst succesvol te zijn. Er zijn verschillende toepassingen te bedenken voor de verkregen landoppervlakteparameters (dit is een verzamelnaam voor de bodemtemperatuur, bodemvocht en de optische diepte van de vegetatie). In dit proefschrift worden een aantal toepassingen voor de drie parameters aangeleverd en anderen worden besproken. De verkregen resultaten kunnen worden gebruikt om de drie parameters te bestuderen op verschil-

lend spatieel (bijvoorbeeld regionaal, continentaal of globaal) maar ook op verschillend temporeel (bijvoorbeeld seizoenaal of interjaarlijks) niveau.

10.2 Bodemtemperatuur

De bodemtemperatuur is een belangrijke parameter in het oplossen van de stralings-transportvergelijking voor bodemvocht. In deze studie is er een op zichzelf staand bodemtemperatuurmodel ontwikkeld. Alhoewel het bodemtemperatuurmodel stabiel is, is het gebaseerd op regressie en is zijn nauwkeurigheid gelimiteerd aan de beschikbaarheid van grondobservaties die nodig zijn om het model te calibreren.

De uit het model verkregen bodemtemperatuur in Noord Amerika is waarschijnlijk het meest betrouwbaar omdat de meeste grondobservaties die gebruikt zijn voor calibratie en validatie van het model daar vandaan komen. Dit heeft in alle waarschijnlijkheid ook effect op de prestatie van het bodemvochtmodel en de daarbij verkregen parameters. De prestatie van zowel het bodemtemperatuurmodel en het bodemvochtmodel zal verbeterd worden bij het gebruik van aanvullende bodemtemperatuur datasets uit verschillende gebieden.

De bodemtemperatuur is verkregen uit vertikaal gepolariseerde 37 GHz helderheidstemperaturen. Het is aangetoond dat helderheidstemperaturen van deze frequentie en polarisatie sterk gerelateerd zijn aan de bodemtemperatuur. Deze relatie wordt niet zichtbaar verstoord door veranderingen in de atmosfeer of bodemvocht.

De helderheidstemperaturen werden vergeleken met veldwaarnemingen uit Oklahoma van bodemtemperaturen op 5 cm diepte. Er werd een lineaire relatie tussen deze 2 parameters waargenomen. De temperatuur van de uitstralende laag bij 6.6 GHz (dit is de parameter die nodig is als invoer voor het bodemvochtmodel) werd gemodeleerd met behulp van de satelliet gerelateerde bodemtemperaturen op 5 cm in combinatie met een interpolatietechniek. De interpolatietechniek was gebaseerd op bodemtemperatuur observaties in Maryland (afkomstig van het Beltsville Agricultural Research Center, BARC) en Botswana op 1.25 cm en 5 cm diepte.

10.3 Bodemvocht en Vegetatie

Om verschillende biofysische aspecten van de vegetatie te monitoren kan heel goed gebruik gemaakt worden van de optische diepte van de vegetatie in het microgolvenbereik. Deze parameter heeft een aantal voordelen ten opzichte van vegetatie parameters die verkregen zijn uit zichtbare/nabij infrarode instrumenten. Zo kan de optische diepte van de vegetatie onder alle weersomstandigheden bepaald worden. Het gebruik van alleen de optische diepte van de vegetatie voor het monitoren van de vegetatie geeft echter niet het optimale resultaat. Dit heeft te maken met het feit dat de optische diepte van de vegetatie op andere biofysische eigenschappen reageert dan vegetatie parameters verkregen uit zichtbare/nabij infrarode instrumenten. Gecombineerd zullen deze parameters een breder en beter beeld geven van de biofysische karakteristieken van de vegetatie.

Bewezen is dat het verkrijgen van bodemvocht uit microgolven de meest betrouwbare techniek in de teledetectie is. Dit komt omdat de omhooggaande energie in het microgolvenbereik direct gerelateerd is aan het absolute watergehalte van de bodem. De getoonde techniek is gebaseerd op de theorie van de stralingstransport, en calibratie van het model in welke vorm dan ook (bijvoorbeeld met veldwaarnemingen van bodemvocht of vegetatie) is niet nodig. Het blijkt de eerste techniek te zijn in zijn soort die succesvol ruimtelijk bodemvocht schat op een globale schaal.

Alhoewel het model zijn beperkingen heeft in het oplossen van de landoppervlakteparameters, zijn deze beperkingen inherent gekoppeld aan microgolvenfysica, en zijn geen functie van het model zelf. Optimale uitvoering van het model kan verwacht worden met L-band microgolven data. Het model kan direct worden gebruikt op de nieuwe Advanced Microwave Scanning Radiometer (AMSR) observaties. De verwachting is dat deze observaties overeenkomstig zijn met de in deze studie gebruikte Scanning Multichannel Microwave Radiometer (SMMR) observaties. Door het toedoen van een hogere spatiale resolutie van deze nieuwe sensor zullen er wel wat kleine model aanpassingen moeten plaatsvinden.

Bodemvocht en de optische diepte van de vegetatie zijn verkregen uit tweevoudig gepolariseerde helderheidstemperatuur observaties in het microgolven bereik. Voor deze studie werd het model toegepast op 6.6 GHz SMMR helderheidstemperaturen. Om de hoeveelheid variabelen te reduceren, zijn er verschillende aannames gemaakt bij de stralingstransportvergelijking. Het model neemt aan dat de single scattering albedo gelijk blijft. De waarde van deze parameter is verkregen uit de literatuur. De invloed van de ruwheid van de bodem op het microgolvensignaal is verwaarloosd omdat er wordt aangenomen dat de ruwheid een minimaal effect heeft wanneer er op satelliet-schaal gekeken wordt. Dagen met sneeuw of vorst zijn ook uit de analyse verwijderd.

Er werd een niet lineaire iteratieve techniek toegepast om voor de bodemvocht en optische diepte van de vegetatie op te lossen. Beiden werden bepaald aan de hand van de diëlectrische constante van de bodem.

Het model werd toegepast op verschillende gebieden met veldobservaties van bodemvocht. Deze gebieden konden gevonden worden in de Verenigde Staten, Mongolië en Turkmenistan. De tijdseries van de met behulp van de satelliet verkregen bodemvocht kwam goed overeen met de veldobservaties van bodemvocht en neerslag. De optische diepte van de vegetatie had vergelijkbare seizoenale patronen als de Normalized Difference Vegetation Index (NDVI).

10.4 Gevoeligheid van het Model

Een fouten analyse werd toegepast op de uit satellietwaarnemingen verkregen landoppervlakteparameters van testlocaties uit de Verenigde Staten en Eurazië. De standaard deviatie van de bodemtemperatuur was klein en gemiddeld 1.2 graden Celcius voor alle testlocaties. De standaarddeviatie van het verkregen bodemvocht was hoog bij een hoge optische diepte van de vegetatie. De uitstralende energie van de bodem wordt verzwakt door de vegetatie en bij een groeiende vegetatie dichtheid wordt de gevoeligheid van de microgolvensensor om bodemvocht te meten verkleind.

Lage bodemvocht waarden hebben ook hoge standaarddeviaties. Deze hoge deviaties werden vooral veroorzaakt door de lage gevoeligheid van de diëlectrische constante van de bodem ten opzichte van bodemvocht tijdens droge condities.

Optimale detectie van bodemvocht met het satelliet model kan verkregen worden met hoge bodemvocht waarden onder een schaarse begroeiing.

In vergelijking met natte condities is het model om de optische diepte van de vegetatie te bepalen minder nauwkeurig in droge situaties. Dit fenomeen heeft ook een theoretische grondslag. Bij droge condities is de bodem emissiviteit hoog en de contributie van vegetatie op de bodememissiviteit is dan laag. Als het bodemvocht toeneemt dan zal de bodememissiviteit afnemen en de contributie van de vegetatie op de emissiviteit weer toenemen.

Een maskeer routine is toegepast om de betrouwbaarheid van de verkregen landoppervlakteparameters te vergroten. Deze routine bestaat uit een techniek om pixels met sneeuwbedekking, pixels met vorst, en pixels met een te dikke vegetatiebedekking te elimineren. Pixels met sneeuw werden gedetecteerd met een verschilalgorithme en pixels met bevroren bodems werden gevonden met het nieuw ontwikkelde bodemtemperatuurmodel.

Bij een optische diepte van de vegetatie tot 0.8 geeft het op satellietwaarnemingen gebaseerde model nog betrouwbare bodemvocht en vegetatie informatie. Pixels die in eerste instantie een optische diepte van 0.8 of meer genereerden werden uit de procedure gehaald.

10.5 Golflengte Effecten

De verkregen landoppervlakteparameters uit 18 GHz data bleken overeen te komen met de resultaten uit de 6.6 GHz data. Dit resultaat ondersteunt het idee om de 19.4 GHz observaties van de Special Sensor Microwave Imager (SSM/I) sensor te gebruiken om de bodemvocht en vegetatie database uit te breiden. Echter, bij deze hoge frequentie observaties zijn er meer beperkingen.

Ten eerste is de penetratiediepte van de 18/19.4 GHz observaties ongeveer 0.5 cm. Verder kunnen er slechts betrouwbare veranderingen in bodemvocht geregistreerd worden bij een waarde van de optische diepte van de vegetatie van onder de 0.65. Deze waarde representeert bij 18 GHz een dunner vegetatiedek dan bij 6.6 GHz, want de optische diepte van de vegetatie is omgekeerd evenredig met de golflengte.

Daarbij komt ook dat de invloed van de atmosfeer, waarbij met name de hoeveelheid waterdamp een rol van betekenis speelt, significant gaat worden bij frequenties boven de 10 GHz. Bij deze hogere frequentie observaties wordt daarom ook ten zeerste aangeraden om een atmosferische correctiecomponent in het model in te voeren om zo optimaal bodemvocht uit de microgolven data te halen.

10.6 Toepassingen

Naast het primaire doel van dit onderzoek, wat de ontwikkeling van een landoppervlakteparameter model was, zal dit proefschrift ook een aantal potentiële toepassin-

gen demonstreren en bespreken.

Tijdseries van de optische diepte van de vegetatie werden vergeleken met NDVI en Leaf Area Index (LAI) data. Naast de vele overeenkomsten werden er ook een aantal verschillen geconstateerd. Deze verschillen waren voorspeld omdat microgolven anders reageren op biofysische karakteristieken dan zichtbaar/nabij infrarood metingen. Verder worden de zichtbaar/nabij infrarood waarnemingen vaak als een compositie in tijd gepresenteerd (bijvoorbeeld als een 15 dagen of maandelijks gemiddelde). De data wordt zo gepresenteerd om de ongunstige atmosferische effecten te minimaliseren. De metingen van de optische diepte van de vegetatie in het microgolvenbereik hebben veel minder last van atmosferische effecten en kunnen daardoor vegetatie informatie verschaffen over een veel betere temporele resolutie.

Naast het feit dat de bodemtemperatuur een hele belangrijke parameter is in het oplossen van de stralingstransportvergelijking, biedt het ook andere interessante toepassingen. Zo kan de bodemtemperatuur een belangrijke bijdrage leveren in globale studies die zich bezig houden met de detectie van temperatuurveranderingen in combinatie met het broeikas effect.

Regelmatige observaties van ruimtelijk representatief bodemvocht is erg nuttig voor studies die zich bezig houden met micrometeorologische fenomenen zoals klimaatverandering maar ook landoppervlakveranderingen, en studies die zich bezig houden met de validatie van Globale Circulatie Modellen (GCMs). Zo is bijvoorbeeld al vastgesteld dat om betrouwbare klimatologisch en hydrologische voorspellingen te maken, nauwkeurige initialisatie van bodemvocht noodzakelijk is.

10.7 Vervolgstudies

Tijdens dit onderzoek zijn er een aantal vervolgstudies geïdentificeerd en een aantal worden hieronder kort besproken.

Uitgebreide bodemtemperatuur helderheidstemperatuur studies

Verbeteringen in het bodemtemperatuurmodel zal de nauwkeurigheid in het verkrijgen van bodemvocht en optische diepte significant verbeteren. Het bodemtemperatuurmodel is momenteel alleen gebaseerd op waarnemingen uit Oklahoma, Maryland, en Botswana. Pogingen om nieuwe datasets van bodemtemperatuur waarnemingen van de top laag onder verschillende ecologische condities te bemachtigen zullen gemaakt gaan worden. Ook zal er worden aanbevolen om bij huidige en toekomstige veldexperimenten deze parameter te gaan meten. Het toepassen van het bodemtemperatuur model in nieuwe sensor platformen zoals de Soil Moisture and Ocean Salinity Mission (SMOS) en AMSR zal de bepaling van bodemtemperatuur aanzienlijk verbeteren.

Globale bodemtemperatuur studies

De dataset van bodemtemperatuur zal vergroot worden met verkregen data afkomstig van de vertikaal gepolariseerde 37 GHz observaties van SSM/I wat zal resulteren in een database van ongeveer 25 jaar. Deze lange tijdreeks kan dan gebruikt worden om bijvoorbeeld temperatuur veranderingen te detecteren in ecologisch gevoelige ge-

bieden.

Atmosferische correctie voor helderheidstemperaturen boven de 10 GHz frequentie

Horizontaal gepolariseerde helderheidstemperaturen bij een frequentie boven de 10 GHz zijn gevoelig voor atmosferische invloeden, met name waterdamp. In extreme gevallen kan waterdamp in de atmosfeer voor een verandering van 10 graden Celcius zorgen, wat aangeeft dat een atmosferische correctie noodzakelijk is. Microgolvendata van de Tropical Rainfall Measuring Mission (TRMM) en SSM/I zullen gecorrigeerd moeten worden voor waterdamp voordat ze in het bodemvocht- en vegetatiemodel gebruikt kunnen worden.

Toepassing van het landoppervlaktemodel op SSM/I en TRMM observaties

De datasets van globale bodemvocht en optische diepte van de vegetatie zullen worden uitgebreid met recente data met behulp van de SSM/I en TRMM observaties.

Toepassing van het landoppervlaktemodel op AMSR

Wanneer de data beschikbaar komt, zal het landoppervlaktemodel worden toegepast op observaties van AMSR. Dit instrument is te vinden op de Advanced Earth Observing Satellite II (ADEOS II) en AQUA satelliet. Deze sensor missies worden gecombineerd met uitgebreide veldcampagnes. De veldwaarnemingen tijdens deze campagnes kunnen leiden tot verbeterde model validaties.

Analyse van globale bodemvocht

De meer dan 25 jaar geregistreerde geschiedenis van globale bodemvocht zal geanalyseerd worden op spatiele en temporele trends met behulp van verscheidene technieken waaronder Fourier analyse en andere trend detectietechnieken. Dit soort studies kunnen informatie verschaffen over globale veranderingen en klimaat-anomalien zoals El Niño-Zuidelijke Oscillatie.

Analyse van globale optische diepte van de vegetatie

De optische diepte van de vegetatie in het microgolven bereik heeft een sterke fysische relatie met het watergehalte van de vegetatie, geometrie van de plant, en biomassa. Tot nu toe zijn er nog weinig pogingen gedaan om biofysische eigenschappen uit de optische diepte te halen en de pogingen die er gedaan zijn, zijn hoofdzakelijk empirisch van aard. Er zal geprobeerd worden om met behulp van de microgolven fysica biofysische parameters uit de optische diepte van de vegetatie te halen.

Bibliography

Becker, F. and Choudhury, B. J. (1988). Relative sensitivity of normalized difference vegetation index (NDVI) and microwave polarization difference index (MPDI) for vegetation and desertification monitoring. *Remote Sensing of Environment*, 24:297–311.

Brunfeldt, D. R. and Ulaby, F. T. (1984). Measured microwave emission and scattering in vegetation canopies. *IEEE Transactions on Geoscience and Remote Sensing*, 22:520–124.

Calvet, J. C., Chanzy, A., and Wigneron, J. P. (1996). Retrieval in the Sahel from Airborne Multifrequency Microwave Radiometry. *IEEE Transactions on Geoscience and Remote Sensing*, 34:588–600.

Calvet, J. C., Wigneron, J. P., Mougin, E., Kerr, Y., and Brito, J. (1994). Plant water content and temperature of the Amazon forest from satellite microwave radiometry. *IEEE Transactions on Geoscience and Remote Sensing*, 32:397–408.

Chahine, M. T. (1983). Interaction mechanisms within the atmosphere. In Colwell, R. N., editor, *Manual of Remote Sensing*. John Wiley, New York.

Chang, A. T. C., Foster, J. L., and Hall, D. K. (1987). Nimbus-7 SMMR derived global snow cover parameters. *Annals of Glaciology*, 9:39–44.

Chen, J. M. and Black, T. M. (1992). Foliage area and architecture of plant canopies from sunfleck size distributions. *Agricultural and Forest Meteorology*, 60:249–266.

Choudhury, B. J. (1993). Desertification. In Gurney, R. J., Foster, J. L., and Parkinson, C., editors, *Atlas of satellite observations related to global change*. Cambridge University Press.

Choudhury, B. J. and Golus, R. E. (1988). Estimating soil wetness using satellite data. *International Journal of Remote Sensing*, 9:1251–1257.

Choudhury, B. J., Major, E. R., Smith, E. A., and Becker, F. (1992). Atmospheric effects on SMMR and SSM/I 37 GHz polarization differences over the Sahel. *International Journal of Remote Sensing*, 13:3443–3463.

- Choudhury, B. J., Schmugge, T. J., Chang, A. T., and Newton, R. W. (1979). Effect of surface roughness on the microwave emission from soils. *Journal of Geophysical Research*, 84:5699–5706.
- De Jeu, R. A. M. and Owe, M. (2002a). Further validation of a new methodology for surface moisture and vegetation optical depth retrieval. *International Journal of Remote Sensing*. In Press.
- De Jeu, R. A. M. and Owe, M. (2002b). Estimating spatially averaged surface soil temperature for microwave surface moisture derivation. *Remote Sensing of Environment*. Submitted.
- De Jeu, R. A. M. and Owe, M. (2002c). Limitations of land surface parameters derived from passive microwave remote sensing. *International Journal of Remote Sensing*. Submitted.
- Defries, R. S. and Townshend, J. R. G. (1994). NDVI-derived land cover classifications at a global scale. *International Journal of Remote Sensing*, 15:3567–3586.
- Dirmeyer, P. A., Zeng, F. J., Ducharne, A., Morill, J. C., and Koster, R. D. (2000). The sensitivity of surface fluxes to soil water content in three land surface schemes. *Journal of Hydrometeorology*, 1:121–134.
- Dobson, M. C., Ulaby, F. T., Hallikainen, M. T., and El-Rayes, M. A. (1985). Microwave dielectric behavior on wet soils, II, Dielectric mixing models. *IEEE Transactions on Geoscience and Remote Sensing*, 23:35–46.
- DryLand-Farming-Research-Scheme-Botswana (1984). *A summary of Meteorological Data Recorded at Sebele, Botswana, 1975-1983*. Ministry of Agriculture, Gaborone, Botswana.
- EarthInfo (1993). *EarthInfo CD² NCDC Hourly and Fifteen Minute Precipitation*. EarthInfo Inc., Boulder (CO), USA.
- EarthInfo (1994). *EarthInfo CD² NCDC Summary of the Day*. EarthInfo Inc., Boulder (CO), USA.
- Eidenshink, J. C. and Faundeen, J. L. (1994). The 1 km AVHRR Global Land Data Set: First Stages in Implementation. *International Journal of Remote Sensing*, 15:3443–3462.
- Entekhabi, D., Asrar, G. R., Betts, A. K., Beven, K. J., Bras, R. L., Duffy, C. J., Dunne, T., Koster, R. D., Lettenmaier, D. P., Mclaughlin, D. B., Shuttleworth, W. J., Van Genuchten, M. T., Wei, M. Y., and Wood, E. F. (1999). An agenda for land surface hydrology research and a call for the second international hydrological decade. *Bulletin of the American Meteorological Society*, 80:2043–2058.
- Fung, A. K. and Eom, H. J. (1981). Emission from a rayleigh layer with irregular boundaries. *J. Quant. Spectr. Radiat. Transfer*, 26:397–409.

- Gloersen, P. and Barath, F. T. (1977). The Scanning Multichannel Radiometer (SMR) Experiment. In Madrid, C. R., editor, *Nimbus-7 Users Guide*, pages 213–245. NASA/GSFC, Beltsville, MD, USA, Beltsville, MD, USA.
- Gouweleeuw, B. T. (2000). *Satellite passive surface moisture monitoring. A case-study on the impact of climatic variability and land use change on the regional hydrogeology of the West La Mancha area in semi-arid central Spain*. PhD thesis, Faculty of Earth Sciences, Vrije Universiteit Amsterdam, the Netherlands.
- Hansen, M. C., DeFries, R. S., and Townshend, J. R. G. (2000). Global land cover classification at 1 km spatial resolution using a classification tree approach. *International Journal of Remote Sensing*, 21:1331–1364.
- Hastenrath, S. (1985). *Climate and Circulation of the Tropics*. D. Reidel, Dordrecht, the Netherlands.
- Holben, B. N., Tucker, C. J., and Fan, C. J. (1980). Spectral assessment of soybean leaf area and leaf biomass. *Photogrammetric Engineering and Remote Sensing*, 46:651–656.
- Hollinger, S. E. and Isard, S. A. (1994). A Soil Moisture Climatology of Illinois. *Journal of Climate*, 7:822–833.
- Houser, P. R., Cosgrove, B. A., Entin, J. K., and Desetty, M. (2000). Land data assimilation system. NASA/GSFC. <http://ldas.gsfc.nasa.gov/index.shtml>.
- Jackson, T. J. (1997). Soil moisture estimation using special satellite microwave/imager satellite data over a grassland region. *Water Resources Research*, 33:1475–1484.
- Jackson, T. J., Bras, R., England, A., Engman, E. T., Entekhabi, D., Famiglietti, J., Kerr, Y., Lakshmi, V., Le Vine, D. M., Liu, T., Martin-Neira, M., Njoku, E. G., O’Neill, P. E., Swift, C., Van Zyl, J., and Wilson, W. J. (1999). Soil Moisture Mission(EX-4). Technical report, NASA Post-2002 Land Surface Hydrology Mission.
- Jackson, T. J. and O’Neill, P. E. (1990a). Laboratory evaluations of a field-portable dielectric soil-moisture probe. *IEEE Transactions on Geoscience and Remote Sensing*, 28:241–245.
- Jackson, T. J. and O’Neill, P. E. (1990b). Attenuation of soil microwave emission by corn and soybeans at 1.4 and 5 GHz. *IEEE Transactions on Geoscience and Remote Sensing*, 28:978–980.
- Jackson, T. J. and Schmugge, T. J. (1991). Vegetation effects on the microwave emission of soils. *Remote Sensing of Environment*, 36:203–212.
- Jackson, T. J., Schmugge, T. J., and Wang, J. R. (1982). Passive microwave sensing of soil moisture under vegetation canopies. *Water Resources Research*, 18:1137–1142.

- Karam, M. A. and Fung, A. K. (1988). Electromagnetic scattering from a layer of finite randomly oriented, dielectric circular cylinder over a rough interface with application to vegetation. *International Journal of Remote Sensing*, 9:1109–1134.
- Karam, M. A., Fung, A. K., Lang, H. R., and Chauhan, N. S. (1992). Microwave scattering model for layered vegetation. *IEEE Transactions on Geoscience and Remote Sensing*, 30:767–784.
- Kerr, Y. H. and Njoku, E. G. (1990). A semi-empirical model for interpreting microwave emission from semi arid land surfaces as seen from space. *IEEE Transactions on Geoscience and Remote Sensing*, 28:384–393.
- Kerr, Y. H. and Wigneron, J. P. (1994). Vegetation models and observations, A review. In Choudhury, B. J., Kerr, Y. H., Njoku, E. G., and Pampaloni, P., editors, *Passive Microwave Remote Sensing of Land-Atmosphere Interactions*, pages 317–344. VSP, Utrecht, the Netherlands.
- Kirdiashev, K. P., Chikhantsev, A. A., and Shutko, A. M. (1979). Microwave radiation of the earth’s surface in the presence of vegetation cover. *Radio Engineering and Electronic Physics*, 24:37–44.
- Lakshmi, V., Wood, E. F., and Choudhury, B. J. (1997). Evaluation of Special Sensor Microwave/Imager Satellite Data for Regional Soil Moisture Estimation over the Red River Basin. *Journal of Applied Meteorology*, 36:1309–1328.
- Lang, R. H. (1981). Electromagnetic backscattering from sparse distribution of lossy dielectric scatterers. *Radio Science*, 16:15–30.
- Lang, R. H., Seker, S., and Le Vine, D. M. (1986). Vector solution for the mean electromagnetic fields in a layer of random particles. *Radio Science*, 21:771–786.
- Le Vine, D. M. and Karam, M. A. (1996). Dependence of attenuation in a vegetation canopy on frequency and plant water content. *IEEE Transactions on Geoscience and Remote Sensing*, 34:1090–1096.
- Los, S. O., Collatz, G. J., Sellers, P. J., Malmström, C. M., Pollack, N. H., DeFries, R. S., Bounoua, L., Parris, M. T., Tucker, C. J., and Dazlich, D. A. (2000). A Global 9-yr Biophysical Land Surface Dataset from NOAA AVHRR Data. *Journal of Hydrometeorology*, 1:183–199.
- Marsh, G. P. (1874). *the Earth as Modified by Human Action*. Scriber and Armstrong Publishers, NY.
- Mätzler, C. and Standley, A. (2000). Relief effects for passive microwave remote sensing. In Mätzler, C., editor, *Radiative transfer models for microwave radiometry. COST Action 712: Application of Microwave Radiometry to Atmospheric Research and Monitoring. Project 1: Development of Radiative Transfer Models.*, pages 81–88. European Communities, Brussels, Belgium.

- McCulloch, J. S. G. and Penman, H. L. (1956). Heat flow in the soil. *Report of the 6th International Soil Science Congress*, B:275–280.
- Meeson, B. W., Corprew, F. E., McManus, J. M. P., Myers, D. M., Closs, J. W., Sun, K. J., Sunday, D. J., and Sellers, P. J. (1995). ISLSCP Initiative I. Global Data Sets for Land-Atmosphere Models, 1987-1988. Volumes 1-5, published on CD-ROM. *NASA Goddard DAAC Science Data Series*.
- Mintz, Y. (1984). The sensitivity of numerically simulated climates to land surface conditions. In Houghton, J., editor, *The Global Climate*, pages 79–105. Cambridge University Press.
- Mitchell, K., Marshall, C., Lohmann, D., Ek, M., Lin, Y., Grunmann, P., Houser, P., Wood, E., Schaake, J., Lettenmaier, D., Tarpley, D., Higgins, W., Pinker, R., Robock, A., Cosgrove, B., Entin, J., and Duan, Q. (2000). The collaborative GCIP land data assimilation (LDAS) project and supportive NCEP uncoupled land-surface modeling initiatives. *15th Conference on Hydrology by the American Meteorological Society*, 15:1–4.
- Mo, T., Choudhury, B. J., Schmugge, T. J., and Jackson, T. J. (1982). A model for microwave emission from vegetation-covered fields. *Journal of Hydrology*, 184:101–129.
- Myneni, R. B., Los, S. O., and Asrar, G. (1995). Potential gross primary productivity of terrestrial vegetation from 1982-1990. *Geophysical Research Letters*, 22:2617–2620.
- New, M., Hulme, M., and Jones, P. D. (1999). Representing twentieth century space-time climate variability. part 1: development of a 1961-90 mean monthly terrestrial climatology. *Journal of Climate*, 12:829–856.
- Njoku, E. G. and Entekhabi, D. (1996). Passive microwave remote sensing of soil moisture. *Journal of Hydrology*, 184:101–129.
- Njoku, E. G. and Kong, J. (1977). Theory of passive microwave remote sensing of near-surface soil moisture. *Journal of Geophysical Research*, 82:3108–3118.
- Njoku, E. G. and Li, L. (1999). Retrieval of land surface parameters using passive microwave measurements at 6-18 GHz. *IEEE Transactions on Geoscience and Remote Sensing*, 37:79–93.
- O’Neill, P., Jackson, T., Blanchard, B., Van den Hoek, R., W., G., Wang, J., Glazar, W., and McMurtrey-III, J. (1983). The Effects of Vegetation and Soil Hydraulic Properties on Passive Microwave Sensing of Soil Moisture: Data Report for the 1982 Field Experiments. Technical Report TM-85106, NASA/GSFC.
- Owe, M., De Jeu, R. A. M., and Walker, J. P. (2001). A methodology for surface soil moisture and vegetation optical depth retrieval using the microwave polarization difference index. *IEEE Transactions on Geoscience and Remote Sensing*, 39:1643–1654.

- Owe, M. and Van de Griend, A. A. (1998). Comparison of soil moisture penetration depths for several bare soils at two microwave frequencies and implications for remote sensing. *Water Resources Research*, 34:2319–2327.
- Owe, M. and Van de Griend, A. A. (2001). On the relationship between thermodynamic surface temperature and high frequency (37 GHz) vertically polarized brightness temperature under semi-arid conditions. *International Journal of Remote Sensing*, 22:3521–3532.
- Owe, M., Van de Griend, A. A., and Chang, A. T. C. (1992). Surface Soil Moisture and Satellite Passive Microwave Observations in Semi-Arid Southern Africa. *Water Resources Research*, 28:829–839.
- Owe, M., Van de Griend, A. A., De Jeu, R. A. M., De Vries, J. J., Seyhan, E., and Engman, E. T. (1999). Estimating soil moisture from satellite microwave observations: Past and ongoing projects, and relevance to GCIP. *Journal of Geophysical Research*, 104:19735–19742.
- Peake, W. (1959). Interaction of electromagnetic waves with some natural surfaces. *IRE Trans.*, AP-7:5342.
- Peplenski, N., Ulaby, F., and Dobson, M. (1995). Dielectric properties of soils in the 0.3-1.3 GHz range. *IEEE Transactions on Geoscience and Remote Sensing*, 33:803–807.
- Rao, Y. P. (1981). Chapter 2, The climate of the Indian sub continent. In Takahashi, K., Arakawa, H., and Landsberg, H., editors, *World Survey of Climatology, Volume 9: Climates of southern and western Asia*. Elsevier Scientific Publishing, New York.
- Rasmusson, E., Dickinson, R., Kutzbach, J., and Cleaveland, M. (1992). Chapter 2, Climatology. In Maidment, D., editor, *Handbook of Hydrology*. McGraw-Hill, Inc., New York.
- Rawls, W. J., Gimenez, D., and Grossman, R. (1998). Use of soil texture, bulk density, and the slope of the water retention curve to predict saturated hydraulic conductivity. *Transactions American Society of Agricultural Engineers*, 41:983–988.
- Rind, D. (1982). The influence of ground moisture conditions in North America on summer climate as modeled in the GISS GCM. *Monthly Weather Review*, 110:1487–1494.
- Robock, A., Vinnikov, K. Y., Srinivasan, G., Entin, J. K., Hollinger, S. E., Speranskaya, N. A., Liu, S., and Namkhai, A. (2000). The Global Soil Moisture Data Bank. *Bulletin of the American Meteorological Society*, 81:1281–1299.
- Rossow, W. B. and Schiffer, R. A. (1991). ISCCP cloud data products. *Bulletin of the American Meteorological Society*, 72:2–20.
- Rowntree, P. R. and Bolton, J. R. (1983). Simulation of atmospheric response to soil moisture anomalies over Europe. *Quarterly Journal of the Royal Meteorological Society*, 109:501–526.

- Schmugge, T. J. (1985). Remote sensing of soil moisture. In Anderson, M. and Burt, T., editors, *Hydrological Forecasting*. John Wiley, New York.
- Schmugge, T. J. (1983). Remote sensing of soil moisture: Recent advances. *IEEE Transactions on Geoscience and Remote Sensing*, 21:336–344.
- Schmugge, T. J. and Choudhury, B. J. (1981). A comparison of radiative transfer models for predicting the microwave emission from soils. *Radio Science*, 16:927–938.
- Schmugge, T. J., O’Neill, P. E., and Wang, J. R. (1986). Passive microwave soil moisture research. *IEEE Transactions on Geoscience and Remote Sensing*, 24:12–22.
- Sellers, P. J., Meeson, B. W., Closs, J., Collatz, J., Corprew, F., Dazlich, D., Hall, F. G., Kerr, Y., Koster, R., Los, S., Mitchell, K., McManus, J., Myers, D., Sun, K. J., and Try, P. (1995). *An overview of the ISLSCP Initiative I Global Data Sets. On: ISLSCP Initiative I. Global Data Sets for Land-Atmosphere Models, 1987-1988. Volumes 1-5. Volume 1*. NASA/GSFC, Greenbelt (MD), USA.
- Shukla, J. and Mintz, Y. (1982). Influence of Land Surface Evapotranspiration on the Earth’s Climate. *Science*, 215:1498–1501.
- Theis, S. W. and Blanchard, B. J. (1988). The effect of measurement error and confusion from vegetation on passive microwave estimates of soil moisture. *International Journal of Remote Sensing*, 9:333–340.
- Thornthwaite, C. W. (1956). Man’s Role in Changing the Face of the Earth. In Thomas, W. L. J., editor, *Modification of Rural Microclimates*. University of Chicago Press, Chicago, IL.
- Townshend, J. R. G., Tucker, C. J., and Goward, S. N. (1993). Global vegetation mapping. In Gurney, R. J., Foster, J. L., and Parkinson, C. L., editors, *Atlas of Satellite Observations related to Global Change*. Cambridge University Press, New York.
- Tsang, L., Kong, J. A., and Shin, R. T. (1985). *Theory of Microwave Remote Sensing*. John Wiley, New York.
- Tsang, L. and Newton, R. (1982). Microwave emission from soils with rough surfaces. *Journal of Geophysical Research*, 87:9017–9024.
- Tucker, C. J., Elgin, J. H., and McMurtrey, J. E. (1980). Relationship of crop radiance to alfalfa agronomic values. *International Journal of Remote Sensing*, 1:69–75.
- Ulaby, F. T., Moore, R. K., and Fung, A. K. (1982). *Microwave Remote Sensing - Active and Passive. Vol. I: Microwave Remote Sensing Fundamentals and Radiometry*. Artech House, Boston (MA),USA.

- Ulaby, F. T., Moore, R. K., and Fung, A. K. (1986). *Microwave Remote Sensing - Active and Passive. Vol. III: From Theory to Applications*. Adisson-Wesley Readings, Dedham (MA),USA.
- USDA (1994). *State soil geographic (STATSGO) data base-data use information, miscellaneous publication number 1492 (rev. ed.)*. Forth Worth, Texas, Natural Conservation Service, USA.
- Van de Griend, A. A. (2001). The Effective Thermodynamic Temperature of the Emitting Surface at 6.6 GHz and Consequences for Soil Moisture Monitoring from Space. *IEEE Transactions on Geoscience and Remote Sensing*, 39:1673–1679.
- Van de Griend, A. A., De Jeu, R. A. M., Seyhan, E., De Vries, J. J., and Owe, M. (1998). *Desertification of the Iberian Peninsula. Contribution to RESMEDES-Final Report, EU-contract ENV4-CT95-0094*. Faculty of Earth Sciences, Vrije Universiteit, Amsterdam, the Netherlands.
- Van de Griend, A. A. and Owe, M. (1994a). The Influence of Polarization on Canopy Transmission Properties at 6.6 GHz and Implications for Large Scale Soil Moisture Monitoring in Semi-Arid Environments. *IEEE Transactions on Geoscience and Remote Sensing*, 32:409–415.
- Van de Griend, A. A. and Owe, M. (1994b). Microwave vegetation optical depth and inverse modelling of soil emissivity using Nimbus/SMMR satellite observations. *Meteorology and Atmospheric Physics*, 54:225–239.
- Van de Griend, A. A., Owe, M., De Ruiter, J., and Gouweleeuw, B. T. (1996). Measurement and Behavior of Dual-Polarization vegetation Optical Depth and Single Scattering Albedo at 1.4- and 5-GHz Microwave Frequencies. *IEEE Transactions on Geoscience and Remote Sensing*, 34:957–965.
- Van Oevelen, P. J. (2000). *Estimation of Areal Soil Water Content through Microwave Remote Sensing*. PhD thesis, Wageningen University, the Netherlands.
- Van Wijk, W. R. (1963). *Physics of plant environment*. North Holland Publishers, Amsterdam, the Netherlands.
- Walker, J. M. and Rowntree, P. R. (1977). The effect of soil moisture on circulation and rainfall in a tropical model. *Quarterly Journal of the Royal Meteorological Society*, 103:29–46.
- Walker, J. P. and Houser, P. R. (2001). A methodology for initializing soil moisture in a global climate model: Assimilation of near surface soil moisture observations. *Journal of Geophysical Research*, 106:11761–11774.
- Walker, J. P., Kurer, D. F., and Houser, P. R. (2000). A field evaluation of ERS-2 synthetic aperture radar data for soil moisture measurement. *EOS, Transactions American Geophysical Union*, 81:S207.

- Wang, J., O'Neill, P., Engman, E., McMurtrey-III, J., Lawless, P., Schmugge, T., Jackson, T., Gould, W., Fuchs, J., and Glazar, W. (1982). Remote measurements of soil moisture by microwave radiometers at BARC test site, II. Technical Report TM-83954, NASA/GSFC.
- Wang, J., Shiue, J., Engman, E., McMurtrey-III, J., Lawless, P., Schmugge, T., Jackson, T., Gould, W., Fuchs, J., Calhoun, C., T., C., Hirschmann, E., and Glazar, W. (1980). Remote measurements of soil moisture by microwave radiometers at BARC test site. Technical Report TM-80720, NASA/GSFC.
- Wang, J. R. (1983). Passive microwave sensing of soil moisture content: The effects of soil bulk density and surface roughness. *Remote Sensing of Environment*, 13:329–344.
- Wang, J. R. and Choudhury, B. J. (1981). Remote sensing of soil moisture content over bare field at 1.4 GHz frequency. *Journal of Geophysical Research*, 86:5277–5282.
- Wang, J. R. and Schmugge, T. J. (1980). An empirical model for the complex dielectric permittivity of soils as a function of water content. *IEEE Transactions on Geoscience and Remote Sensing*, 18:288–295.
- Wegmüller, U., C., M., and Njoku, E. G. (1994). Canopy opacity models. In Choudhury, B. J., Kerr, Y. H., Njoku, E. G., and Pampaloni, P., editors, *Passive Microwave Remote Sensing of Land-Atmosphere Interactions*, pages 375–387. VSP, Utrecht, the Netherlands.
- Wilheit, T. T. J. (1975). Radiative transfer in a plane stratified dielectric. Technical Report X-911-75-66, NASA/GSFC.
- Zobler, L. (1986). A world soil file for global climate modeling. Technical Report TM-87802, NASA/GSFC.

Appendix A

WANG-SCHMUGGE MODEL

In the Wang-Schmugge model (1980) the dielectric constant ε of a soil-water mixture is described as

$$\varepsilon = \theta \cdot \varepsilon_x + (P - \theta) \cdot \varepsilon_a + (1 - P) \cdot \varepsilon_r, \quad \theta \leq \theta_t \quad (\text{A.1})$$

with

$$\varepsilon_x = \varepsilon_i + (\varepsilon_w - \varepsilon_i) \cdot \frac{\theta}{\theta_t} \cdot \gamma \quad (\text{A.2})$$

and

$$\varepsilon = \theta_t \cdot \varepsilon_x + (\theta - \theta_t) \cdot \varepsilon_w + (P - \theta) \cdot \varepsilon_a + (1 - P) \cdot \varepsilon_r, \quad \theta > \theta_t \quad (\text{A.3})$$

with

$$\varepsilon_x = \varepsilon_i + (\varepsilon_w - \varepsilon_i) \cdot \gamma \quad (\text{A.4})$$

Where θ is the volumetric water content [$\text{m}^3 \text{m}^{-3}$] of the soil, P the porosity of the dry soil (total volume occupied by pores per unit volume of soil), γ is an empirical parameter, and θ_t is the transition moisture [$\text{m}^3 \text{m}^{-3}$]. ε_a , ε_w , ε_r and ε_i , in sequential order, are the dielectric constants of air, water, rock and ice. ε_x stands for the dielectric constant of the initially absorbed water.

The transition moisture is defined as the moisture content at which the free water phase begins to dominate the soil system and can be described as

$$\theta_t = 0.49 \cdot WP + 0.165 \quad (\text{A.5})$$

Where WP is the wilting point of the soil in [$\text{m}^3 \text{m}^{-3}$]. When WP is unknown but there is information about the particle size distribution of the soil, WP can be redetermined as

$$WP = 0.06774 - 0.00064 \cdot SAND + 0.00478 \cdot CLAY \quad (\text{A.6})$$

where $SAND$ and $CLAY$ are the sand and clay contents in percent of dry weight of a soil.

γ can be estimated by

$$\gamma = 0.57 \cdot WP + 0.481 \quad (\text{A.7})$$

The complex dielectric constants for ice (ε_i), solid rock (ε_r) and air (ε_a) are $3.2+0.1i$, $5.5+0.2i$ and $1+0i$, respectively. The dielectric constant for water (ε_w) is given by the Debye Equation

$$\varepsilon_w = \varepsilon_{w\infty} + \frac{\varepsilon_{w0} - \varepsilon_{w\infty}}{1 + (2 \cdot \pi \cdot t_w \cdot f)^2} \quad (\text{A.8})$$

Where $\varepsilon_{w\infty}$ is the high frequency limit of the dielectric constant of pure water (≈ 4.9), ε_{w0} is the static dielectric constant of pure water, t_w the relaxation time of pure water in seconds, and f is the electro magnetic frequency in Hz. Equation A.8 can be divided in a real and an imaginary part. The real part is defined by Ulaby et al. (1986), as

$$\varepsilon'_w = \varepsilon_{w\infty} + \frac{\varepsilon_{w0} - \varepsilon_{w\infty}}{1 + (2 \cdot \pi \cdot t_w \cdot f)^2} \quad (\text{A.9})$$

and the imaginary part (ε''_w) as

$$\varepsilon''_w = \frac{2 \cdot \pi \cdot t_w \cdot f \cdot (\varepsilon_{w0} - \varepsilon_{w\infty})}{1 + (2 \cdot \pi \cdot t_w \cdot f)^2} \quad (\text{A.10})$$

The static dielectric constant of pure water is given as

$$\varepsilon_{w0} = 88.045 - 0.4147 \cdot (T - 273.15) + 6.295 \cdot 10^{-4} \cdot (T - 273.15)^2 + 1.075 \cdot 10^{-5} \cdot (T - 273.15)^3 \quad (\text{A.11})$$

where T is the effective temperature of the emitting layer in Kelvin. The relaxation time of pure water is

$$2\pi t_w = 1.1109 \cdot 10^{-10} - 3.824 \cdot 10^{-12} \cdot (T - 273.15) + 6.938 \cdot 10^{-14} \cdot (T - 273.15)^2 - 5.096 \cdot 10^{-16} \cdot (T - 273.15)^3 \quad (\text{A.12})$$

Appendix B

ACRONYMS AND SYMBOLS

Acronyms

ADEOS-II	Advanced Earth Observing Satellite II
AMSR	Advanced Microwave Scanning Radiometer
ARS	Agriculture Research Service
AVHRR	Advanced Very High Resolution Radiometer
BARC	Beltsville Agricultural Research Center
CRU	Climate Research Unit
DAAC	Distributed Active Archive Center
DDC	Data Distribution Centre
DMSF	Defense Meteorological Satellite Program
EDC	EROS Data Center
ENSO	El Niño-Southern Oscillation
EROS	Earth Resources Observation System
GCM	Global Circulation Model
GCIP	GEWEX Continental-Scale International Project
GTOPO30	Global 30 Arc Second Elevation Data Set
fPAR	fraction of Photosynthetically Active Radiation
FAO	Food and Agriculture Organization
GEWEX	Global Energy and Water Cycle Experiment
GSFC	Goddard Space Flight Center
IPCC	Intergovernmental Panel on Climate Change
ISCCP	International Satellite Cloud Climatology Project
ISLSCP	International Satellite Land Surface Climatology Project
LAI	Leaf Area Index
LDAS	Land Data Assimilation System
MPDI	Microwave Polarization Difference Index
NASDA	National Space Development Agency of Japan
NASA	National Aeronautics and Space Administration
NCDC	National Climate Data Center
NDVI	Normalized Difference Vegetation Index

NOAA	National Oceanic and Atmospheric Administration
NSIPP	NASA Seasonal-to-Interannual Prediction Project
SEE	Standard Error of Y Estimated
R-J	Rayleigh-Jeans Approximation
SMMR	Scanning Multichannel Microwave Radiometer
SMOS	Soil Moisture and Ocean Salinity Mission
SSM/I	Special Sensor Microwave Imager
STATGO	State Soil Geographic data base
TMI	TRMM Microwave Instrument
TRMM	Tropical Rainfall Measuring Mission
USDA	United States Department of Agriculture
USGS	United States Geological Survey
VWC	Vegetation Water Content
WCRP	World Climate Research Program
W-S	Wang-Schmugge Dielectric Mixing Model

Symbols

Γ	Microwave vegetation transmissivity	[-]
γ	Empirical parameter in Wang-Schmugge Model	[-]
ε	Dielectric constant of a soil-water mixture	[-]
ε'	Real part of the dielectric constant of a soil-water mixture	[-]
ε''	Imaginary part of the dielectric const. of a soil-water mixture	[-]
ε_a	Dielectric constant of air	[-]
ε_i	Dielectric constant of ice	[-]
ε_r	Dielectric constant of rock	[-]
ε_w	Dielectric constant of water	[-]
ε'_w	Real part of the dielectric constant of water	[-]
ε''_w	Imaginary part of the dielectric constant of water	[-]
$\varepsilon_{w\infty}$	high frequency limit of the dielectric constant of water	[-]
ε_{w0}	Static dielectric constant of water	[-]
ε_x	Dielectric constant of initially absorbed water	[-]
θ	Volumetric water content of the soil	[m ³ m ⁻³]
θ_t	Transition moisture	[m ³ m ⁻³]
λ	Wavelength	[m]
τ	Vegetation optical depth	[-]
ω	Single scattering albedo	[-]
a	Long term trend	[value month ⁻¹]
A	Seasonal amplitude	[value year ⁻¹]
A_0	Amplitude of the surface temperature	[K year ⁻¹]
b	Constant that depends on vegetation type and frequency	[-]
c	Column number or longitude	[-]
C_j	Fitting parameter for the optical depth model	[-]

<i>CLAY</i>	Clay content in percent of dry weight	[%]
d_{1-3}	Fitting parameters for the time series analysis	[-]
d_{mean}	9-year mean value	[value]
D	Damping depth	[cm]
e_c	Above canopy emissivity	[-]
e_r	Rough surface emissivity	[-]
e_s	Smooth surface emissivity	[-]
f	Electro magnetic frequency	[Hz]
g	phase-shift or time to peak	[date]
H	Horizontal polarization angle	[-]
h	Soil surface roughness	[-]
j	Polynomial parameter for the optical depth model	[-]
k	Absolute value of the dielectric constant of the soil	[-]
l	polarization angle, H or V	[-]
M	Polynomial parameter for the optical depth model	[-]
N	Polynomial parameter for the optical depth model	[-]
n	number of observations	[-]
P	Porosity of the soil	[$m^3 m^{-3}$]
p	Precipitation	[$mm day^{-1}$]
P_n	Periodicity	[months]
r	Row number or latitude	[-]
R	Surface reflectivity	[-]
<i>SAND</i>	Sand content in percent of dry weight	[%]
T	Effective temperature of the emitting layer	[K]
T_{ave}	Average temperature of the surface	[K]
T_b	Brightness temperature	[K]
T_c	Canopy temperature	[K]
T_s	Surface temperature	[K]
$T_{s[zcm]}$	Soil temperature at z cm depth	[K]
t	time	[months]
t_d	time	[days]
t_w	Relaxation time of pure water	[s]
u	Incidence angle	[° from nadir]
V	Vertical polarization angle	[-]
w_d	Frequency	[$days^{-1}$]
w_n	Frequency	[$months^{-1}$]
<i>WP</i>	Wilting point of the soil	[$m^3 m^{-3}$]
z	Soil depth	[cm]

Acknowledgements

Well, where did it all start.

In February 1999 Manfred Owe asked me if I could come to the U.S. for a 3 months research visit to work on soil moisture retrievals from passive microwave remote sensing. At that time I already worked at the Vrije Universiteit Amsterdam as a research assistant at various projects and I was planning to quit science and to become a high school teacher. However, a final research job at NASA was quite irresistible for me. So a few months later I arrived in the U.S. and Manfred had arranged everything for me to live the *All American Dream* with a big old white Cadillac, a nice apartment, and immediately my first pay-check. I was really surprised and had a very good time these three months.

In August I came back and in September 1999 I started as a high school teacher. After 2 weeks of teaching geography to some malicious 15 year old kids from the Hague I realized that this was not the way for me, and started to dream about the good summer I had in the U.S. So I called Manfred if he had a research position for me and he told me he had something for a year. The research job he told me about was funded by the NSIPP program and I could work on the development of a global soil moisture database.

So in December 1999 I was back at NASA. The forthcoming research year went very well and halfway through Manfred convinced me to get a Ph.D. out of it. So I started to search for a Dutch promotor and fortunately I found Prof.dr Hans Vugts, who was willing to do the job. After a year I came back to the Netherlands and with an additional 2 month visit at NASA and a research position at the Vrije Universiteit Amsterdam I was able to finish this thesis.

However, without the help and support of a lot of people this thesis would not be completed. And I would like to thank a number of people in particular:

Manfred Owe, many, many thanks for all your unconditional support and getting me back into science. It has been a great pleasure to work with you and you always helped my out when I was struggling with practical or scientific problems. Your guidance during the data processing phase, as well as your critical remarks on the draft version of this dissertation greatly improved the final result. I hope we can continue to work and fish together in the near future.

Hans Vugts for solving all the practical problems concerning a Ph.D including the opportunity you gave me to finish the thesis at the Vrije Universiteit. Your open

Acknowledgements

mind, sense of humor, and support were a great value for me.

The members of the reading committee Prof.dr. Han Dolman, VU Amsterdam, Prof.dr. Allard Meijerink, ITC Enschede, Prof.dr.ir. Peter Troch, WAU Wageningen, dr.ir. Bart van den Hurk, KNMI De Bilt, dr. Eni Njoku JPL Pasadena (CA), USA, and dr. Pierre Guillevic, LCPC Bouguenais Cedex, France for reviewing the draft text.

All the NASA people who helped my out during my visits at Goddard: Paul Houser, Jared Entin, Brian Cosgrove, Jeffrey Walker, Michele Rienecker, Randy Koster, Max Suarez, Rolf Reichle, Janet Chien, David Adamec, Peggy O'Neill, Jim Foster, Dave Toll, Nick Digirolamo, Hao Jin, Meg Larko, and Thorsten Markus.

Sietse Los, for giving me the privilege to use the latest NOAA/AVHRR NDVI data but also to taste his delicious erwtensoep.

All the people I met at NASA who joined the heavy lunches at the cafeteria, diners, drinks, and exclusive parties with me: Agnes Ducharne, Sarith Mahanama, Augustin "*Mr BBQ*" Vintzileos, Jean-Pierre "*Date Man*" Alfano, Sébasti en Li enard, Fred, Boris, Alex, Aaron Berg, and Linda Pacini.

Of course my good French friends, "*the good guys*" Pierre Guillevic and Paul Poli. Beside the work, you thought me how to live the good life. Many, many thanks !!

The two Dutch students who joined me at NASA, Guido v/d Werf en Rogier van Opstal. Thanks, for all the fun and good time we had together.

Many thanks to the friends and (ex) colleagues of the VU: Friso Holwerda, Corry N, Albert "*met je geitengezicht*" Van Dijk, Michiel "*Q*" van der Molen, Reinder Ronda, Christiaan van der Tol, Jaap Schellekens, Ray Hafkenscheid, Ben "*Don Bingo*" Gouweleeuw, Arnoud Frumau, Paul Smeets, Joost Vermeulen, Elmer v/d Berg, Maarten Waterloo, Sampurno Bruijnzeel, Antoon Meesters, and Michel Groen.

Marcel and Chretienne for reading and correcting the draft version of the Dutch summary.

My two notorious "*Paranimfen*" Marcel de Jeu en Robert "*Krent*" Hoogenboom.

Verder wil ik uiteraard al mijn vrienden en familie, Greet en Leo in het bijzonder, bedanken voor al hun steun. Ook zij hebben continu dat geteut van me moeten aanhoren. Ik denk niet dat het teuten minder zal worden maar het zal in ieder geval niet meer zo vaak gaan over dit boekje dat meer dan een jaar *bijna af* was.

And last but not least, Anne. Tjonge, jonge.... ik weet niet zo goed waar ik moet beginnen, maar door jouw steun, vertrouwen, en liefde kon ik dit allemaal doen. Mijn dank is groot, een hele dikke knuffel !!

Publications and Reports

De Jeu, R.A.M. (1996). *Hydrology of two montane forests of contrasting stature in the Blue Mountains of Jamaica*, Master's Thesis, Faculty of Earth Sciences, Vrije Universiteit, Amsterdam.

De Jeu, R.A.M., R. Hoogeveen, and J. Peeters (1995). Estimation of natural groundwater recharge through the unsaturated zone at the Veluwe with chemical and physical methods. A water balance study by means of micrometeorology, tracer techniques and soil water content simulation. *Veluwe Time series*, Vol. 4, Faculty of Earth Sciences, Vrije Universiteit Amsterdam.

De Jeu, R.A.M., and M. Owe (2002). Further Validation of a new Methodology for Surface Moisture and Vegetation Optical Depth Retrieval. *International Journal of Remote Sensing*. In Press.

De Jeu, R.A.M., and M. Owe (2002). Derivation of a global soil moisture and vegetation database from passive microwave signals. In *Proceedings of SPIE series, Remote Sensing for Agriculture, Ecosystems and Hydrology IV*, Vol. 4879, Crete, Greece.

De Jeu, R.A.M., and M. Owe (2002). Estimating Spatially Averaged Surface Soil Temperature for Microwave Surface Moisture Derivation. *Remote Sensing of Environment*. Submitted.

De Jeu, R.A.M., and M. Owe (2002). Limitations of Land Surface Parameters derived from Passive Microwave Remote Sensing. *International Journal of Remote Sensing*. Submitted.

Hafkenscheid, R.L.L.J., L.A. Bruinzeel, and R.A.M. De Jeu (1998). Estimates of fog interception by montane rain forest in the Blue Mountains of Jamaica. In R.S. Schemenhauer and H. Bridgman, editors, *First International Conference on Fog and Fog Collection*, pp. 33-36, Vancouver.

Hafkenscheid, R.L.L.J., L.A. Bruijnzeel, R.A.M. De Jeu, and N.J. Bink (1999). Water budgets of two upper montane rain forests of contrasting stature in the Blue Mountains, Jamaica. In *Proceedings of the Second International Colloquium on Hydrology and Water Managements in Humid Tropics*, Cathalac.

Hafkenscheid, R.L.L.J., F. Holwerda, L.A. Bruijnzeel, R.A.M. De Jeu, J. Schellekens, and F.N. Scatena (1999). Transpiration from tropical montane cloud forests in the Blue Mountains, Jamaica and the Luquillo Mountains, Puerto Rico. In *Second International Colloquium on Hydrology and Water Management in the Humid Tropics*, Panama City, Panama.

Owe, M., and R.A.M. De Jeu (2002). Combining Day- and Nighttime Satellite Microwave Observations for Improved Temporal Resolution of Satellite Surface Moisture Retrievals *Water Resources Research*. In prep.

Owe, M., and R.A.M. De Jeu (2002). Large Area Spatial and Temporal Trends in Surface Soil Moisture as Derived from Satellite Microwave Observations. *Journal of Geophysical Research*. In prep.

Owe, M., and R.A.M. De Jeu (2002). Surface parameter retrieval at global scales by microwave remote sensing. In *Proceedings of SPIE series, Remote Sensing for Agriculture, Ecosystems and Hydrology IV*, Vol. 4879, Crete, Greece.

Owe, M., and R.A.M. De Jeu (2002). Recent Advances in Microwave Sensing of Soil Moisture. In *Proceedings Europto series, Remote Sensing for Agriculture, Ecosystems, and Hydrology III*, Vol. 4542, Toulouse, France.

Owe, M., and R.A.M. De Jeu (2002). The Need for Regular Remote Sensing Observations of Global Soil Moisture. In D.T. Hansen, V.R. Singhroy, R.R. Pierce, and A.I. Johnson, editors, *Spatial Methods for Solution of Environmental and Hydrologic Problems: Science, Policy, and Standardizations - Implications for Environmental Decisions ASTM STP 1420*, American Society for Testing and Materials, West Conshohocken, Pennsylvania.

Owe, M., and R.A.M. De Jeu (2001). Retrieving Surface Soil Moisture and Vegetation Optical Depth from Satellite Microwave Observations. In *Proceedings International Geoscience and Remote Sensing Symposium (IGARSS)* [CD Rom], 9-13 July, Sydney, Australia.

Owe, M., R.A.M. De Jeu and J.P. Walker (2001). A Methodology for Surface Soil Moisture and Vegetation Optical Depth Retrieval Using the Microwave Polarization Difference Index. *IEEE Transactions on Geoscience and Remote Sensing*, 39:1643-1654.

Owe, M., A.A. Van de Griend, and R.A.M. De Jeu (2000). Estimating long term surface soil moisture in the GCIP area from satellite microwave observations. In *Proceedings Remote Sensing and Hydrology Symposium 2000*, Publ. No. 267, Santa Fe, New Mexico.

Owe, M., A.A. Van de Griend, and R.A.M. De Jeu (2000). A methodology for estimating surface soil temperature from high frequency microwave observations. In *Proceedings Europto series, Remote Sensing for Agriculture, Ecosystems, and Hydrology II*, Vol. 4171, Barcelona, Spain.

Owe, M., A.A. Van de Griend, and R.A.M. De Jeu (1999). Estimates of long term surface soil moisture in the midwestern U.S. derived from satellite microwave observations. In *Proceedings Europto series, Remote Sensing for Earth Science, Ocean, and Sea Ice Applications*, Vol. 3868, Florence, Italy.

Owe, M., A.A. Van de Griend, R.A.M. De Jeu, J.J. De Vries, E. Seyhan, and E.T. Engman (1999). Estimating Soil Moisture from Satellite Microwave Observations: Past and ongoing projects, and relevance tot GCIP. *Journal of Geophysical Research*, 24:19735-19742.

Van de Griend, A.A., R.A.M. De Jeu, E. Seyhan, J.J. De Vries and M. Owe (1999). *Physically Based Monitoring of Soil Moisture Fields and Change Detection in Mediterranean Regions by Passive Microwave Remote Sensing*, Contribution to RESYSMED-Final Report. Faculty of Earth Sciences, Vrije Universiteit, Amsterdam.

Van de Griend, A.A., R.A.M. De Jeu, E. Seyhan, J.J. De Vries and M. Owe (1998). *Desertification of the Iberian Peninsula*, Contribution to RESMEDES-Final Report. Faculty of Earth Sciences, Vrije Universiteit, Amsterdam.

